Check for updates

Recent advances in multi-metallic organic frameworks and their derivatives for catalysis, electro-/photocatalysis and sensing applications

Mohammad Mazraeh, [a] Zeynab Hedayati, [a] Ana Primo,[b]
Amarajothi Dhakshinamoorthy, *[cd] Ali Morsali*[a] and Hermenegildo Garcia [*b]

The growing global demand for advanced porous materials for a wide range of applications has spurred significant interest in metal–organic frameworks (MOFs). These structures are highly valued for their engineering versatility, combined with multifunctionality, vast chemical space, and structural diversity. Various strategies have been developed to enhance the performance of MOFs in different applications, with one of the most promising approaches being the incorporation of multiple metals into their structure to form multi-metallic organic frameworks (MMOFs). MMOFs exhibit outstanding performance compared to MOFs due to the tunable synergistic effect among diverse metals, enabled by precise structural engineering. The simultaneous presence of several metals imparts exceptionally enhanced properties to MMOFs, including active site tunability, which optimizes their catalytic, photocatalytic, and electrocatalytic performance. Additionally, MMOFs exhibit superior sensing capabilities, characterized by higher sensitivity and precision, and demonstrate improved medicinal properties. This review provides a comprehensive, critical view of MMOFs, focusing on their synthesis strategies, challenges, and the specific or preferential role of each metal when they are present in MMOFs. Further, this review also covers their applications in various fields, such as catalysis, photocatalysis, electrocatalysis, electrical energy storage, gas separation, adsorption, sensing, and medicine. Furthermore, the review offers guidelines in the selection of metals for tailoring MMOFs to specific applications. Numerous existing examples show the superior performance of MMOFs compared to single-metal MOFs (SMOFs), underscoring the synergistic effects arising from the combination of multiple metals present in the structure. This favorable synergy makes MMOFs the most efficient material in a wide range of technological and industrial applications.

1. Introduction

Approximately 25 years ago, porous metal–organic frameworks (MOFs) were reported by Kitagawa,[1] Yaghi,[2] and Férey,[3] and they quickly captured the attention of the scientific community. MOFs are composed of organic linkers and metal nodes, featuring unique characteristics such as high surface area, significant porosity, and tunable design with predictable structures based on the consideration of the linker structure and the directionality of the metal–ligand coordinative bond.[2,4] These properties can be customized by selecting specific metal

ions, organic linkers, and secondary building units (SBUs) with various compositions and directionality of the coordination bonds.[4] MOFs have found applications across numerous fields, including medicine,[5] sensing,[6] catalysis,[7] renewable energy sector,[8] and gas adsorption and separation.[9]

The porous structures of MOFs have attracted considerable attention due to their customizable pore design, adjustable chemical properties, and high surface area,[10,11] providing a toolbox to adapt the materials for their practical applications. Despite their widespread use, there is always continued interest in further improving MOF performance, the discovery of new variants, and advances in their industrial scalability, promising a transformative impact on science and technology.[12]

A subclass of MOFs, known as multi-metallic organic frameworks (MMOFs), incorporates more than one metal ion in their structure.[13] These metals may be integrated into the MOF structure as metal–organic compounds, metal complexes within cavities, or as part of the MOF nodes. Bimetallic or heterometallic MOFs are included in this category.[14] The incorporation of multiple metals can frequently create

[a]Department of Chemistry, Faculty of Sciences, Tarbiat Modares University, P. O. Box 14115-175, Tehran, Iran. E-mail: morsali_a@yahoo.com

[b]Instituto Universitario de Tecnología Química, Consejo Superior de Investigaciones Científicas, Universitat Politecnica de Valencia, Av. De los Naranjos s/n, 46022, Valencia, Spain. E-mail: hgarcia@qim.upv.es

[c]Departamento de Química, Universitat Politècnica de València, C/Camino de Vera, s/n, 46022, Valencia, Spain. E-mail: admguru@gmail.com

[d]School of Chemistry, Madurai Kamaraj University, Madurai 625021, Tamil Nadu, India

synergistic interactions among them, enhancing the performance of MMOFs compared to single-metal MOFs (SMOFs) in applications such as electrocatalysis,[15] photocatalysis,[16,17] gas separation,[18] energy storage,[19,20] and sensing.[21]

In 2019, our group published the well-received paper "Mixed-Metal MOFs: Unique Opportunities in Functionalization and Design of Metal–Organic Frameworks",[13] which highlighted the growing significance of MMOFs and their applications. Since then, the field has seen rapid development, as evidenced by the exponential increase in the number of publications on MMOFs, particularly notable since 2016 (Fig. 1a). This growing interest underscores the need for an updated review of recent advances in MMOFs to show the current state of the art, the present bottlenecks, and the challenges ahead.

Numerous reviews and perspectives have emphasized the critical role of the preparation of MMOFs and their derivatives, focusing on their use in specific applications. For example,

some perspectives have focused on the challenges and opportunities associated with metal node engineering in electrical energy storage systems.[22] Gallis and coworkers have provided a detailed description of the topological properties of MMOFs, synthetic methodologies, metal distributions within MMOFs, their characterization and applications including catalysis.[23] Reviews covering synthesis routes, characterization techniques, and computational studies of MMOFs and their derivatives provide a conceptual framework to understand the reasons for the improved performance of MMOFs in applications such as catalysis, photocatalysis, and electrocatalysis.[13,24–26] Additionally, some reviews compare the development and performance of bimetallic MOFs and trimetallic MOFs and their derivatives with their SMOF counterparts.[27,28] Some reviews have focused on the specific applications of MMOFs and their derivatives, such as energy storage (*e.g.*, supercapacitors and batteries),[29–31] water splitting (including oxygen evolution reaction (OER) and

Mohammad Mazraeh obtained his BSc degree in Applied Chemistry from Shahid Chamran University in Ahwaz in 2019. Subsequently, he earned his MSc degree in Inorganic Chemistry from K. N. Toosi University of Technology, Tehran, in 2023, under the supervision of Professor Saeed Rayati. Currently, he is pursuing a PhD in Inorganic Chemistry under the supervision of Professor Ali Morsali at Tarbiat Modares

Mohammad Mazraeh

University in Tehran. His research primarily concentrates on the design and engineering of Metal–Organic Frameworks (MOFs) in electrocatalysis and photocatalysis.

Zeynab Hedayati received her BSc and MSc degrees from Shahid Beheshti University and the University of Tehran, respectively. In 2023, she joined the research group of Professor Ali Morsali at Tarbiat Modares University, where she works under the supervision of the professor. Her research expertise is in the design, synthesis, and application of metal–organic frameworks (MOFs) focused on pharmaceuticals, sensing technologies, catalysis, and photocatalysis.

Zeynab Hedayati

Dr Ana Primo received her PhD in chemistry from the Universidad Politécnica de Valencia (Spain) in 2006. From 2007 to 2009, she conducted postdoctoral research at the Institute Charles Gerhardt of Montpellier, France. Currently, she is a tenured scientist at the "Instituto de Tecnología Química" (UPV–CSIC). Her research interests include the synthesis of 2D materials (graphene, boron nitride, and MXenes) and their

Ana Primo

application in catalytic and photocatalytic processes such as CO_2 reduction for obtaining methanol or water splitting for H_2 production. She has published more than 100 papers, received more than 7000 citations, and has an h-index of 44.

Amarajothi Dhakshinamoorthy received his PhD degree in 2009 from Madurai Kamaraj University, Madurai-21, India. Later, he worked as a postdoctoral researcher with Prof. Hermenegildo Garcia at the Technical University of Valencia for four years. Currently, he is serving as a UGC-Assistant Professor at the School of Chemistry, Madurai Kamaraj University. His research interests include catalytic/photocatalytic applica-

Amarajothi Dhakshinamoorthy

tions of metal–organic frameworks, covalent organic frameworks and graphene-related materials. He has co-authored over 185 publications, five book chapters and one patent. He is also serving as an Early Career Advisory Board member in Molecular Catalysis, Elsevier.
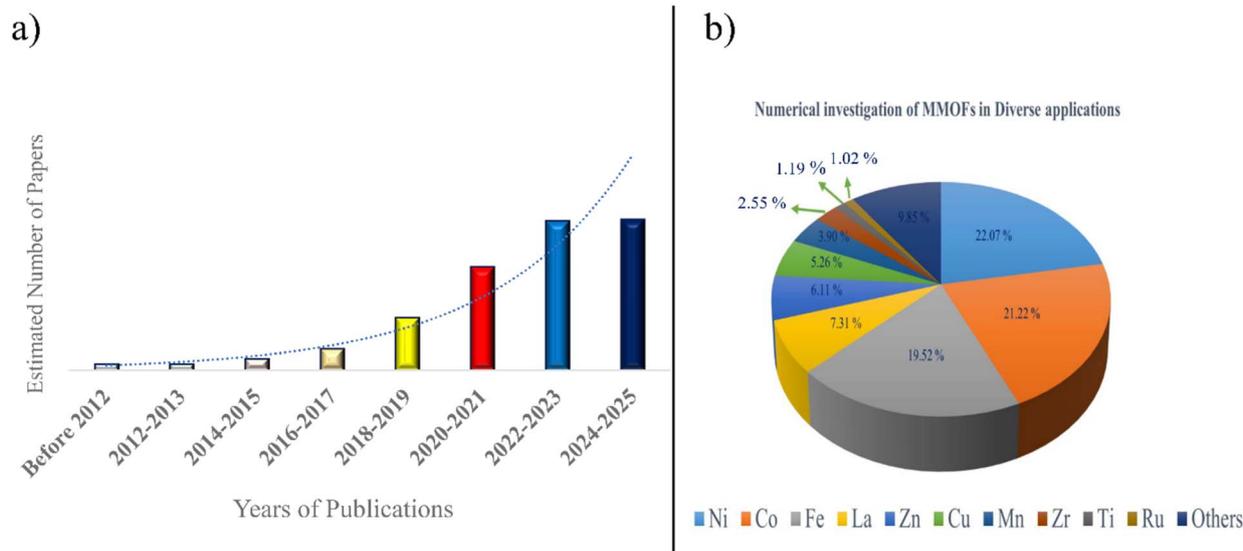
Fig. 1 (a) Plot showing the gradual increase of reports on MMOFs since 2004 based on the *Web of Science* Database (accessed in Nov. 2025); (b) percentage contribution of each metal in the composition of MMOFs during the period 2019–2025.

hydrogen evolution reaction (HER)),[32–37] and photocatalysis.[38,39] Compared to other multi-metal compounds, MMOFs offer advantages, particularly the possibility of designing the structure and versatile synthetic methods, thus justifying their vast usage for diverse applications. Other important features of MMOFs are porosity and vast chemical space in ligands and metals, while metal oxides or alloys can lack this intrinsic chemical diversity. Also, the stability of MMOFs can differ in various applications compared to other multi-metal compounds. Furthermore, MMOFs can be the precursors of a wide range of multi-metal oxides/alloys/carbides and other variants.[40–42] By pyrolysis, MMOFs can be converted into MMOF-derived materials, preserving some advantages of the pristine MMOFs, such as hierarchical porosity, uniform distribution of metals, and tunable electronic structures, rendering highly active electrocatalysts and single-atom sites, which cannot be easily obtained from direct oxide synthesis.[43–45] These accounts comprehensively address synthesis strategies, characterization methods, and applications, underscoring the potential offered by MMOFs in fundamental and technological advancements that focus on the role of metals and their synergistic effect in diverse applications, which is not comprehensively stated in any other reviews. Besides, our review also compares the activity of MMOFs with that of SMOFs in different catalytic applications to

Ali Morsali

Ali Morsali earned his BSc degree in Chemistry from Tarbiat Moallem University, Tehran (Iran), and his M Sc. degree in Inorganic Chemistry at Zanjan University (Iran). He obtained his PhD (2003) and started his independent career at Tarbiat Modares University, where he has been a Professor in the Department of Chemistry since 2012. In recent years, he has spent sabbaticals at Northwestern University (with J. Hupp and O. Farha), UC-Berkeley (with Omar M. Yaghi), and Düsseldorf University (with C. Janiak). His research interests focus on coordination polymers and metal–organic frameworks (MOFs).

Hermenegildo Garcia

Hermenegildo García is a full Professor at the Instituto de Tecnología Química of the Technical University of Valencia and an Honorary Adjunct Professor at the Center of Excellence in Advanced Materials Research of King Abdullaziz University. He works in the field of heterogeneous catalysis with porous solids as well as in the photocatalytic production of solar fuels having published over 900 articles. Prof. Garcia is a Doctor Honoris Causa of the University of Bucharest and received the Spanish National Research Award (2021), the Janssen-Cilag Award of the Spanish Royal Society of Chemistry (2011), the Jaume I Prize for Novel Technologies (2016) and the Medal Lecturer Award from the International Association for Advanced Materials (2021).

precisely illustrate the importance of MMOFs. Eventually, some advantages can be achieved by MMOFs, which are different compared to other multi-metal compounds and justify their vast usage for diverse applications. One of these features can be attributed to the porosity and vast engineering of ligands and metals, while other metal oxides or alloys can lack this intrinsic molecular engineering. Also, the stability of MMOFs can vary depending on engineering assignments compared to other multi-metal compounds. Furthermore, achieving multi-metal oxides/alloys/carbides and other variants by pyrolyzing MMOFs to obtain MMOF-derived materials can not only preserve some advantages of the MMOFs, such as hierarchical porosity, uniform metal dispersion, stability, and tunable electronic structures, but also yield highly active electrocatalysts and single-atom sites, which cannot easily be obtained from direct oxide synthesis.

In this review, we focus on recent progress in MMOFs and their derivatives, which have garnered significant interest in recent years. The review is divided into two sections, with the first part dealing with the synthesis of MMOFs and the second part summarizing their applications. The synthesis methods discussed here include diverse approaches to MMOF formation, either *de novo* or post-synthetic modification, analyzing their specific advantages and disadvantages, and how they impact the structural and functional performance of MMOFs. In the applications section, we emphasize the critical role of incorporating multiple metals, as the introduction of a second, third, or additional metal into the material can significantly enhance some properties of the resulting MMOF with an impact on its performance. This review covers applications in adsorption, catalysis, electrocatalysis, energy storage, photocatalysis, sensing by electrochemical or fluorescence techniques, and related areas reported from 2019 to 2024, providing insights into the influence of multi-metal incorporation on MMOFs in these fields. It also analyzes the interactions among metals, the unique properties present in MMOFs, the structural modifications induced by the incorporation of additional metals in the composition, and the formation of MMOFs.

Fig. 1b illustrates the proportion of the various metallic elements that have been reported in the composition of MMOFs and their derivatives. The applications are categorized into seven primary sections, highlighting each metal role and its interaction with neighboring metals. The intrinsic electroactive properties of Ni make it highly active in electrical energy applications, particularly in electrocatalysis and energy storage, where it significantly enhances specific capacity. Further, Ni-MMOFs are also the most widely used materials in photocatalysis due to their ability to regulate band gaps, thereby improving the photocatalytic activity.[46]

After Ni, the other most frequently reported metals in MMOFs are Co, and Fe. Their electroactive properties make them highly effective in energy-related applications. Fe-MMOFs, in addition to energy applications, are employed in the adsorption and removal of pollutants since the corresponding Fe-MMOFs have abundant active sites. Co-MMOFs, besides their role in energy applications, excel in catalysis, where these MMOFs exhibit high porosity, and their crystalline structure

enhances catalytic efficiency. Lanthanide-based MMOFs demonstrate great potential, particularly in sensing applications, due to the sensitivity of atomic emissions in rare earth ions. The incorporation of additional lanthanide metals further enhances their efficiency through the appearance of synergistic effects. Zn-based MMOFs are also promising for diverse applications. In this case, Zn combined with Co is the most common pairing, as Co enhances crystallinity, while Fe, when paired with Zn, may reduce structural stability. Cu is another widely used metal in MMOFs, contributing to various applications. For the sake of organization, this review classifies MMOFs based on the metal present in the highest proportion in the material. For some metals, like Cu, that have not yet been reported to be in the highest proportion, their examples of MMOFs are scattered in sections corresponding to the most abundant metal.

This review focuses exclusively on MMOFs reported in recent years, offering a comprehensive analysis of the challenges in their synthesis, the impact of various metals on MMOF structures, their unique properties, and the metal–metal interactions. Besides their synthesis, the present review provides a detailed exploration of the diverse applications of MMOFs, categorized by metal composition, and examines the contribution of each of these metals to the structure and functionality of the resulting MMOFs. Considering the vast chemical space, this area of MMOFs remains relatively underexplored, making this review valuable for understanding the remarkable MMOF properties and how metal characteristics determine their applications. Moreover, it presents a fresh perspective on MOF engineering for targeted applications, indicating the rules for the selection and integration of specific metals in MMOFs. Finally, this work highlights the huge potential of MMOFs and opens new avenues for research, offering significant opportunities for future growth and innovation in this rapidly evolving field. Also, application sections with M-based MOFs (M: Fe, Ni, Co, Zn, La, Zr) can give us clear insights into the role of each metal ion in diverse MMOF applications along with their efficiency.

2. Synthetic routes for MMOFs

The synthetic route of a given MMOF is a critical factor influencing their performance in diverse applications, since, depending on the preparation procedure, MMOFs with even the same chemical composition can exhibit contrasting efficiency. Recent research has employed various methods to enhance durability, stability, and activity by forming robust structures. Several reviews have specifically addressed these synthetic procedures, highlighting the importance of the synthesis on the properties.[24,25] In this review, we will discuss some of the most widely used, reliable synthetic routes to provide a clearer understanding of MMOF structures.

Before exploring the applications of MMOFs, we will discuss how the synthesis method can influence the properties of these materials and, consequently, their performance. Direct synthesis methods, such as *in situ*, cluster, and nickel foam strategies, are among the most widely used synthetic procedures, and they will be described earlier in this review. Post-

modification routes, including core–shell, insertion, and exchange strategies, are less general synthetic approaches and more specifically tailored towards a particular application, providing further versatility in MMOF research.

Besides being at the metal nodes, the metallo-ligand approach, where metals are integrated into the linker, also provides an effective strategy for synthesizing MMOFs. This method is particularly advantageous for energy conversion systems, where enhanced porosity, robustness, and functional properties are required. Additionally, the review also covers procedures to obtain MMOF derivatives, particularly employed for energy applications. Transformation of MMOFs into derivatives will also be succinctly covered, as they offer materials with larger surface areas and increased active site accessibility compared to alternative synthetic routes of these derived materials. Fig. 2 illustrates the synthesis routes covered in the present review, emphasizing their impact on MMOF performance and expanding their applicability across various fields. Structural changes in MMOFs occur before synthesis (pre-modification) or after (post-modification). Derived routes can also relate to various modifications that take place in high temperatures to form MMOF derivatives. Metallo-ligand approaches form part of a unique MMOF synthesis pathway; the section explains how linkers containing metals within their structure can be used in the synthesis of MMOFs.

2.1. Synthesis from special precursors

The synthesis of MMOFs, adapting the general procedure of their SMOF counterparts, starting from precursors of the desired metal elements in specific ratios required in the metal nodes and the corresponding organic linkers using reflux, hydrothermal, or solvothermal techniques, has been extensively employed. Although this approach has limitations, such as uneven metal distribution in nodes, it is straightforward and remains the most frequent procedure. This route allows for the synthesis of MMOFs with various structures and morphologies, including foam-like nano-octahedra, hierarchical 3D frameworks, multi-shelled hollow structures, and 2D morphologies. Derived MMOF structures generated through pyrolysis of the direct synthesis are also discussed in the last sections. As illustrated in Fig. 3, the reports on the direct synthesis of MMOFs can be classified into three methods of MMOF synthesis using special precursors. They are discussed in the following sections.

2.1.1. *In situ* **synthesis.** *In situ* synthesis is one of the most widely employed methods for MMOFs. It consists in using, in a conventional synthesis initially reported for an SMOF, a mixture of metal salts in specific molar ratios together with the corresponding organic linker to form MMOFs. Despite its simplicity, this method is influenced by factors such as the different reactivity of the metal ions, coordination environment, and pH. This often results in variability in the incorporation of metal ions in the lattice, with some metals failing to enter the MOF structure. Additionally, this method often requires high energy and is irreversible, meaning that incorporation of one metal ion cannot be reversed by the second metal due to its lower affinity. These negative factors can limit the applicability of the *in situ* incorporation of two or more metal ions in the structure. An example of *in situ* synthesis is the preparation of UiO-66(Zr/Ti) using specific molar ratios of titanium and zirconium salts combined with 1,4-terephthalic acid (H$_2$BDC) in a one-pot synthesis process.[47]
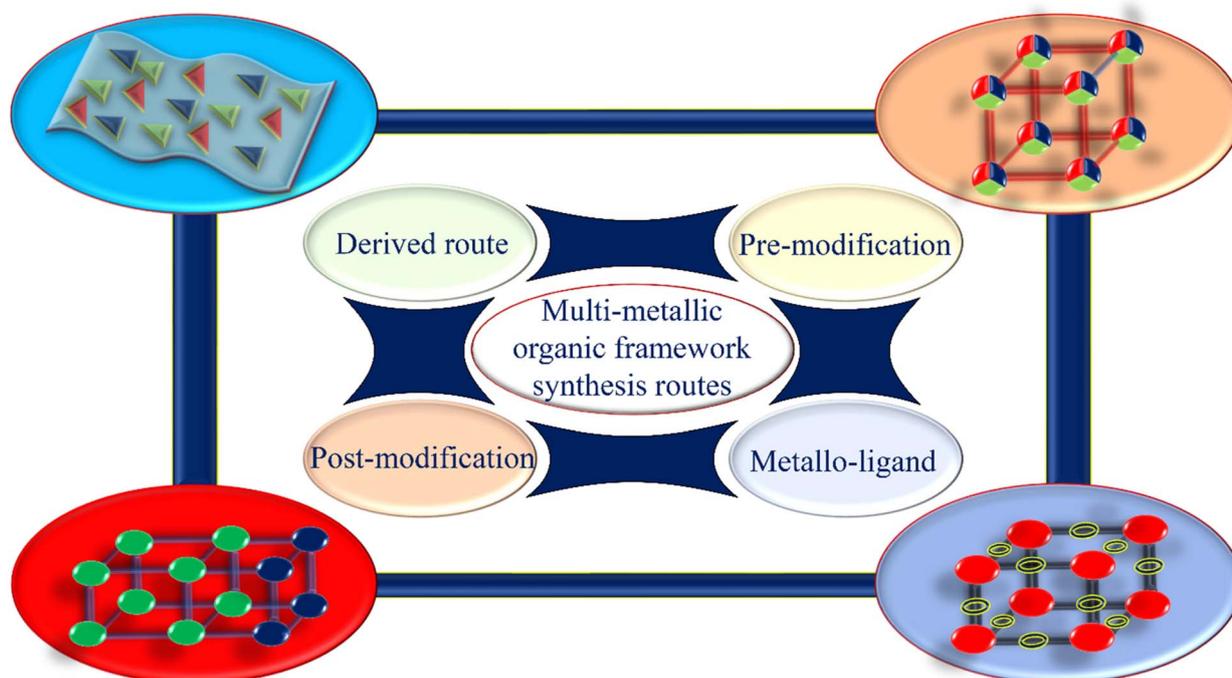

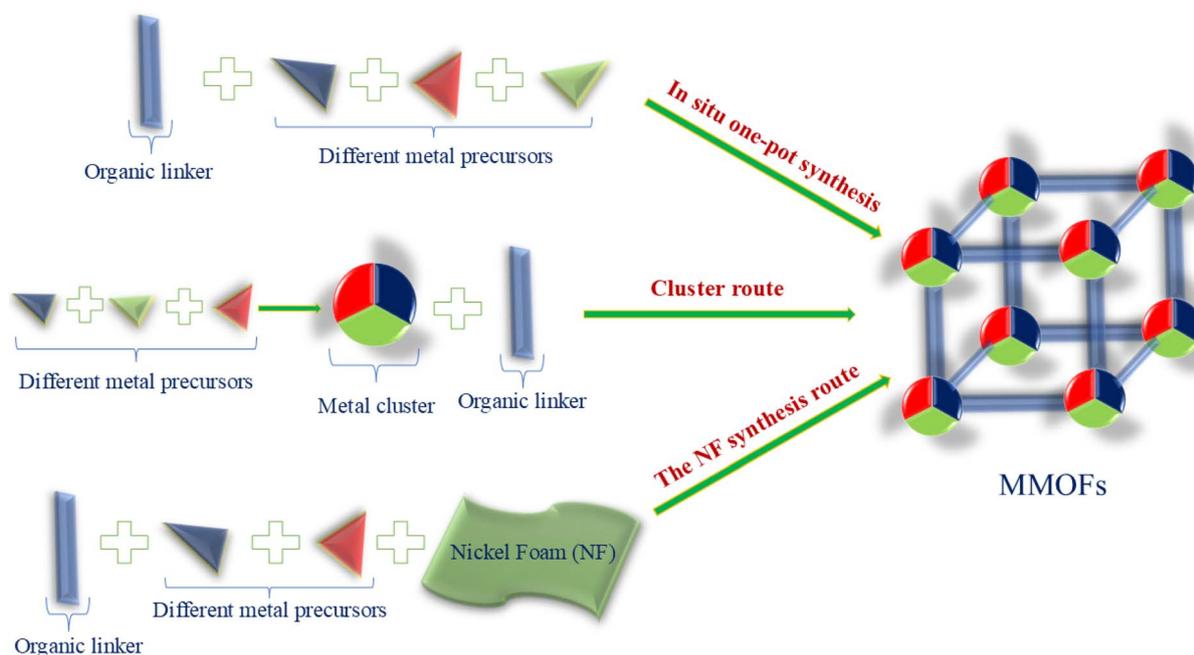**Fig. 2** Most employed synthesis methods for the preparation of MMOFs.

Fig. 3 Procedures for the direct synthesis of MMOFs in which several metals are incorporated simultaneously, including two approaches that employ special precursors.

2.1.2. Cluster synthesis route. The cluster synthesis route is another straightforward synthesis method of MMOFs, which is based on the controlled formation of multi-metallic metal clusters in a pre-synthesis phase. In this method, metal salts are first combined following specific protocols to form clusters of various metals. Organic linkers then react in precise ratios with these preformed clusters to form MMOFs. As an example, a PCN-250-Fe_2M MMOF is synthesized in two steps. First, $Fe_2M(\mu_3\text{-}O)(CH_3COO)_6(H_2O)_3$ clusters are prepared, and then these clusters are reacted with azobenzene tetracarboxylate (H_4ABTC) to produce the PCN-250 structure.[48]

2.1.3. *In situ* growth on nickel foam. The *in situ* growth method on nickel foam (NF) has recently gained considerable popularity, especially in energy-related applications, such as electrocatalysis.[49] This procedure enhances electrical conductivity and performance by achieving a good integration of the MMOF and the conductive NF electrode. This integration is much superior to depositing the preformed MMOF on NF that never achieves similar conductivity.

The process begins by cleaning NF with acid or other treatments to remove surface oxides. Clean NF serves as a Ni source, and it is combined in an autoclave with additional metal salts and linkers to form MMOFs. For example, FeCoNiMn-MOF/NF was synthesized by washing NF with a mixture of HCl, water, and ethanol under sonication. Subsequently, metal salts (Fe, Co, and Mn) and 2,3-dihydroxyterephthalic acid as a linker were added to the autoclave to form the MMOF structure.[50] These synthesis methods employing preformed metal clusters analogous to the metal nodes of the MMOF highlight the versatility and adaptability of MMOF fabrication, enabling the design of materials tailored for specific applications.

2.2. Metallo-ligand approach

The metallo-ligand approach represents a recent and innovative method for synthesizing a new MMOF synthesis route tailored for diverse applications. This technique involves using materials such as ferrocene or metalloporphyrins as organic linkers, allowing for the incorporation of mixed-metal ions into the MOF structure at various defined lattice positions.

In this approach, metal salts in specific ratios are combined with metallo-ligands to form MMOFs, in which at least one metal is not in nodal positions (Fig. 4). The material can then be utilized for various applications, particularly related to catalysis and sensing. Additionally, this method can be integrated with other previous synthesis techniques. For example, metal clusters can be combined with metallo-ligands to fabricate MMOFs, or NF can serve as a precursor and Ni source alongside the metallo-ligand. Although this synthesis route remains relatively underexplored, initial studies have demonstrated its potential for specific applications. For instance, defective $NiFc'_xFc_{1-x}$ MOFs (Fc and Fc': substituted ferrocenes as metallo-ligands) were synthesized by varying the ratios of Fc or Fc' and Ni. The metal sources in these syntheses can include salts or meshes, as illustrated in Fig. 5.[51]

The metallo-ligand approach offers promising opportunities to expand the diversity and functionality of MMOFs, particularly when combined with other advanced synthesis techniques. Further investigation into this method could unlock new possibilities for designing MMOFs with tailored properties for specific applications.

2.3. MMOF-derived materials

MMOF-derived materials have garnered significant attention for their versatility in applications, particularly in
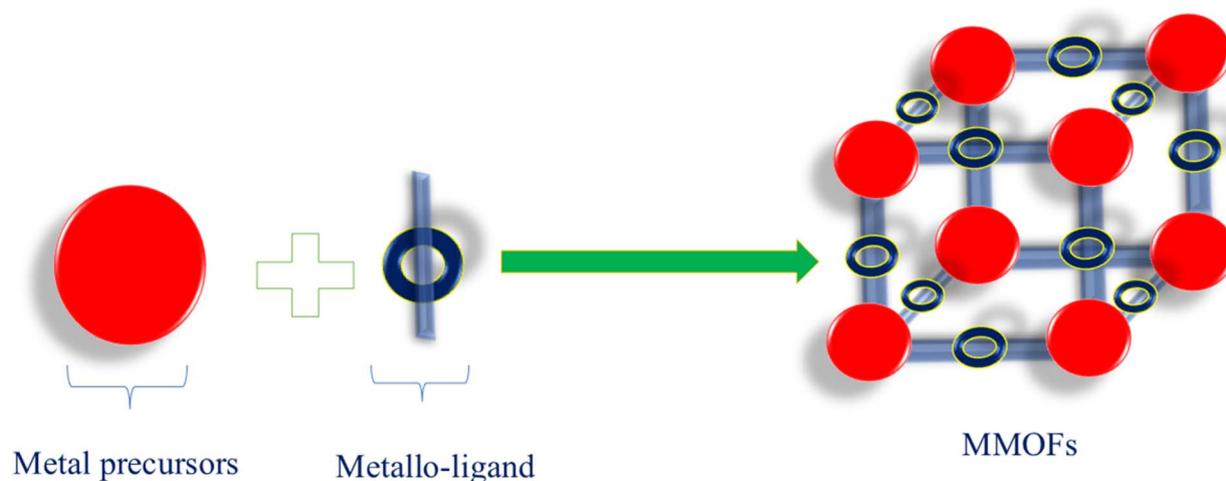
Fig. 4 Preparation of MMOFs using the metallo-ligand approach. It should be noted that metals are present at the nodes as well as at the ligands.

electrocatalysis and electrical energy storage systems.[28] These materials are formed when synthesized MMOF precursors are subjected to controlled transformation, resulting in changes in composition and structure, leading to unique MMOF-derived materials. The most commonly used procedure to obtain MMOF derivatives is high-temperature treatment under an inert atmosphere, which results in the graphitization of the MMOF organic linker. This process can generally result in a carbon matrix acting as a support for fine metal alloy nanoparticles.

The morphology of the derived MMOFs can vary widely, encompassing carbon nanoflowers, nanoflakes, porous frameworks, and hollow structures. These morphologies are influenced by factors such as the initial morphology of the MOFs, pyrolysis temperature, and other external and internal conditions. A growing area of interest is the synthesis of 2D-derived MMOFs, which again offer unique advantages in energy applications due to their notable electrical conductivity.

2.3.1. 2D structures in MMOF derived materials. Two primary methods are used to synthesize 2D MOF structures (nanosheets), either the top-down or the bottom-up route. The top-down approach involves the exfoliation of 3D MOFs into 2D nanosheets by breaking weak interactions, such as hydrogen bonds, π–π stacking, and van der Waals forces. These weak bonds are disrupted through chemical or physical treatments.
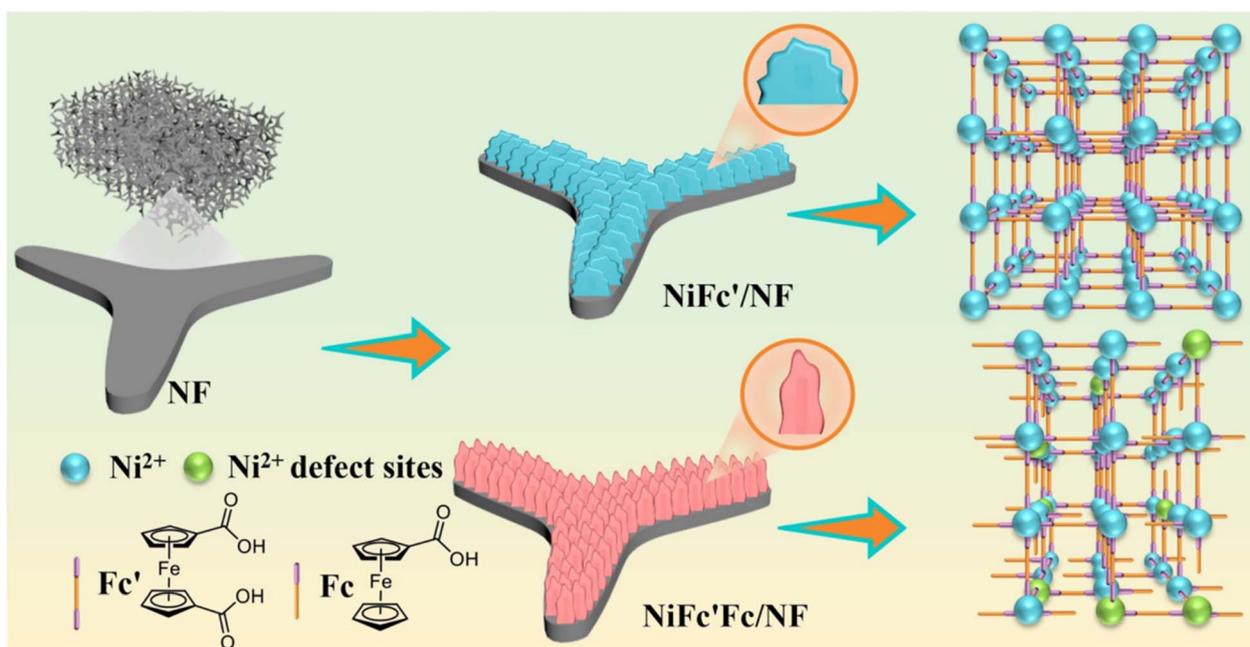

Fig. 5 Synthesis route of the $NiFc'_xFc_{1-x}$ MMOF series grown on NF for OER electrocatalysis. Reproduced with permission from ref. 51, copyright 2023 Wiley.

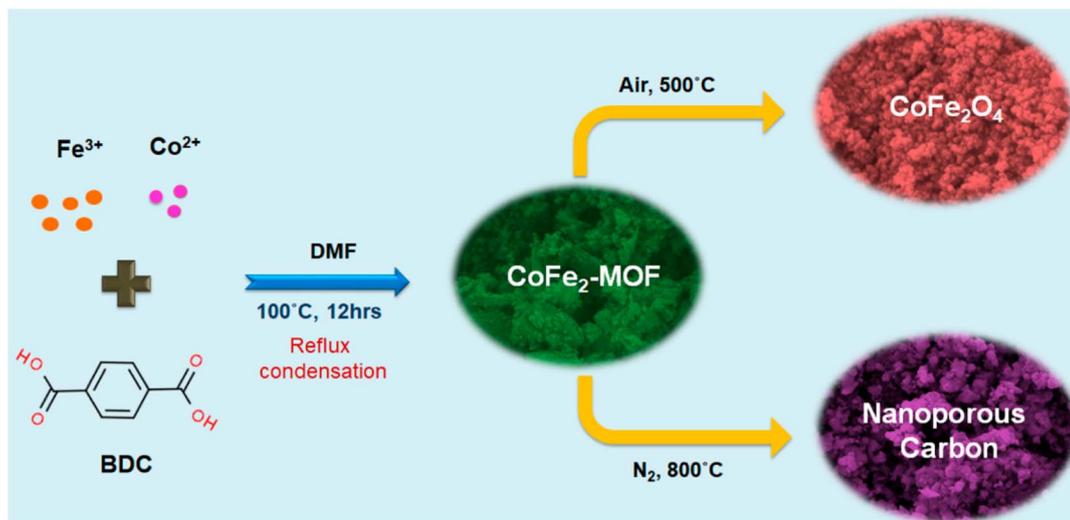**Fig. 6** Synthesis of $CoFe_2O_4$ and NPC solids by pyrolysis of bimetallic MOFs for supercapacitor applications. Reproduced with permission from ref. 53, copyright 2024 American Chemical Society.

In contrast, the bottom-up route generally uses surfactants and modulators to control the thickness of the nascent particles during the crystallization of the MMOF, resulting in 2D structures by arresting the growth in the z-direction.

Subsequently, when 2D MOFs are subjected to pyrolysis, they can form, among other possibilities, layered double hydroxides (LDHs), which are particularly valuable for energy applications due to their enhanced conductivity, cost-effectiveness, and ease of synthesis. LDHs derived from 2D MMOFs have been widely studied for their performance in energy-related technologies. 2D MMOF-derived materials are particularly attractive due to their larger specific surface area and easy site accessibility, which enhances their functionality across a range of applications. In electrochemical systems, they are especially promising because their enlarged surface area improves electrolyte–material interactions, thereby enhancing their performance.

One notable example of MMOF-derived materials for energy applications is trimetallic $Co_{0.2}Fe_{0.8}Ni$–OCNF (OCNF: oxide carbon nanoflower), which can be synthesized from trimetallic Hofmann nanoflower MOFs. After the spontaneous self-assembly of the 2D MOF sheets as nanoflowers, this morphology remains upon pyrolysis. This specific structure creates a large number of accessible active sites, making these materials highly effective for electrocatalysis.[52] In another example, bimetallic Fe_2Co-MOF was employed as a precursor to obtain $CoFe_2O_4$ oxides at 500 °C, and nanoporous carbon (NPC) at 800 °C (Fig. 6). This derivative showed enhanced specific capacitance, making it beneficial for supercapacitor applications.[53] Furthermore, Fig. 7 illustrates conventional synthesis routes for MMOF-derived materials, showcasing their utility in energy applications. By engineering the structure of MMOFs and transforming them into derivatives, it has been possible to obtain materials with enhanced performance and site accessibility, making them among the best candidates for advanced energy technologies.

2.4. Post-synthesis strategies

Post-synthetic modifications start from SMOFs that are subsequently treated to introduce additional metals. This approach encompasses various modification methods tailored for specific applications. The post-synthesis MMOF preparation generally can take place through one of the following three main
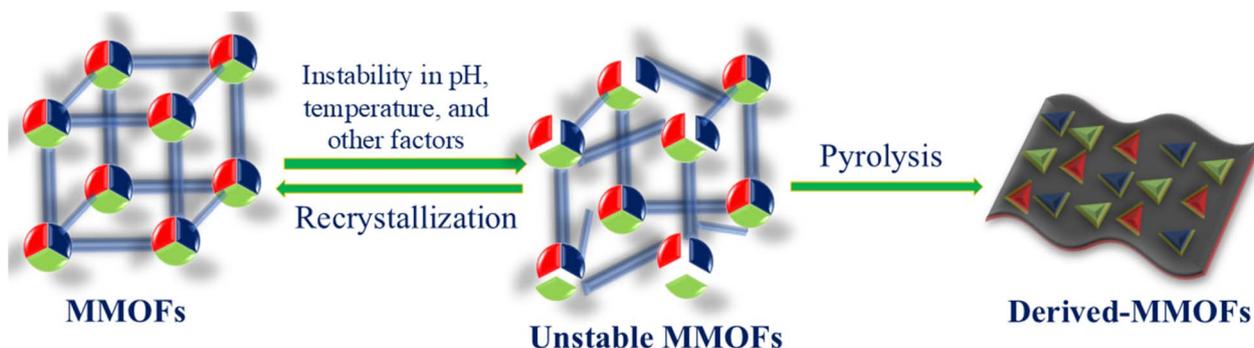

Fig. 7 Preparation of MMOF-derived materials from MMOFs as the precursors.

approaches: core–shell, or insertion, or exchange methods. Fig. 8 summarizes the post-synthetic modification methods.

2.4.1. Core–shell route. Although still poorly explored for MMOF synthesis, the core–shell route involves combining a MOF core with a MOF shell to form MMOFs in which two or more metals are in the material, but at different positions. This method is advantageous for regulating the spatial distribution of the metals in the MMOF, as it is possible to adjust the sizes of the shell and core, resulting in highly porous materials. However, it is challenging to obtain single crystals from the MOF shell, which limits its use in certain applications.[25] Also, core–shell can ensure uniform nucleation and strong adherence between the MOF and substrate and it is expected to be further applied for the synthesis of MMOFs in the future.[54]

2.4.2. Insertion methods. The insertion of metals into pre-formed MOF structures can occur through three primary strategies, namely:

• Functionalized group incorporation. Functional groups can be introduced either within the MOF cavities or on its surface. These groups coordinate with metal ions diffusing into the interior of the crystal to form MMOFs.

• Open metal site provision. Unsaturated coordination sites in the MOF structure enable the incorporation of secondary metals, resulting in MMOF formation.

• Metal penetration. By controlling the molar ratio of metal salts, secondary metals can be introduced into the structure, creating MMOFs.

2.4.3. Exchange methods. The exchange methods involve replacing existing metals or ions within the MOF structure by ions of other elements. Since the metal-linker coordination bond is reversible, additional metals can be, in principle, introduced into the structure by metal ion exchange, exposing the performed MOF to a high concentration of other metal salts, creating in this way MMOFs. There are three primary ways to achieve this exchange:

• Demetallation–addition route. Initially, a SMOF is synthesized. Then, a certain proportion of the metal atoms is removed (demetallation) to create structural vacancies, allowing additional metals to penetrate the structure and form MMOFs.

• Ion exchange. Metal ions within the SMOF structure are directly exchanged with other ions, creating MMOFs.

• Etching procedure. If ion exchange occurs only on the MOF surface rather than throughout the structure, etching can be applied. This approach enables a certain degree of control over the morphology and crystallinity of MMOFs.

While these post-modification methods are versatile and suitable for fine-tuning the morphology and crystalline properties of MMOFs, they present several challenges. For instance, doping, inserting, or exchanging metals may damage MOF crystallinity, which can be detrimental or beneficial depending on the specific application. These merits and limitations are further discussed in the Applications section (Fig. 8).[13,27,29]

3. Applications

This section explores the applications of bimetallic MOFs and MMOFs as well as MMOF-derived materials across various domains, including electrocatalysis, electrical energy storage,
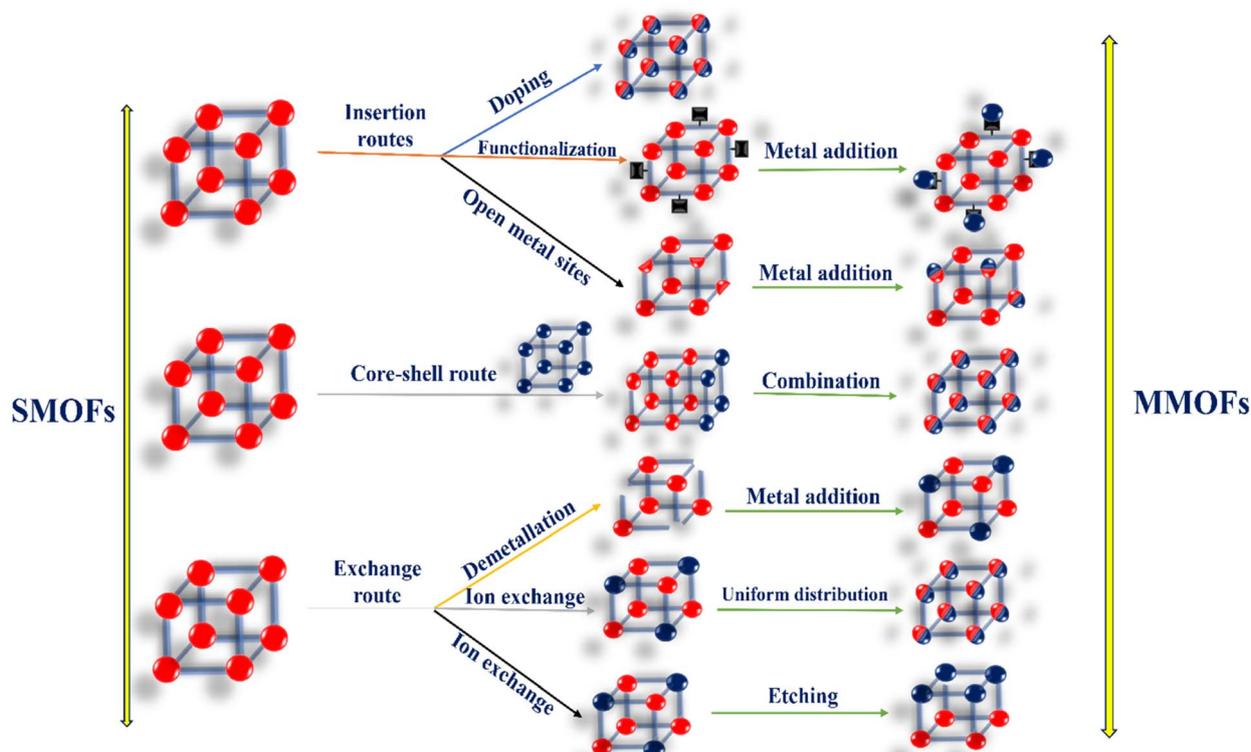

Fig. 8 Different post-synthesis strategies for the preparation of MMOFs.

catalysis, and photocatalysis, as well as sensing, medicine, removal of pollutants and adsorption. Each application is critically reviewed, focusing on the role played by the presence of various metals and their quantitative impact. Emphasis will be placed on the efforts to rationalize the results by advanced characterization, such as X-ray photoelectron spectroscopy (XPS), microscopy, electrochemical measurements, density functional theory (DFT) calculations, and other methods to understand the reasons for the synergy and modification of the electronic structures. While other reviews have covered MMOFs in general applications, this work emphasizes the specific contribution and synergy of mixed metals, resulting in improved MMOF performance.[29–31]

The most extensively studied applications of MMOFs are in energy-related fields, particularly electrocatalysis and electrical energy storage. These areas dominate due to the general observation of synergistic effects between metal ions, the development of cost-effective alternatives to precious metals by combining abundant metals, and the high electroactive potential of materials based on Ni, Fe, and Co. Despite significant progress, challenges, such as synthesis complexity, scalability, and stability, continue to pose limitations for broader adoption in other fields.

Electrocatalysis in MMOFs spans diverse reactions, including water splitting, OER, HER, oxygen reduction reaction (ORR), nitrogen reduction reaction (NRR), urea oxidation reaction (UOR), and CO_2 reduction (CO_2R), among the best studied. Water splitting involves two redox processes: the OER occurs at the anode and the HER at the cathode. While the HER is relatively efficient, the OER is hindered by thermodynamics and high kinetic barriers due to the sluggish four-electron transfer processes, resulting in increased overpotential. MMOFs with non-precious metals offer an alternative to electrodes based on expensive Ru and Ir catalysts for the OER by reducing overpotentials and Tafel slopes, while increasing stability and faradaic efficiency.[55–62] In one example of MMOFs circumventing the OER to reach enhanced H_2 production, the HER was coupled with the glycerol oxidation reaction (GOR), which results in an enhanced HER efficiency, while yielding valuable by-products, like formic acid. The ORR is pivotal for zinc–air batteries; the process requires four-electron reduction. More recent interest is focused on selective two-electron reduction, since it could enable an eco-friendly, electrochemical route for H_2O_2 production from air without the need for H_2. It appears that MMOFs and derived materials are among the best 2-electron ORR electrocatalysts.[63,64] Electrochemical CO_2R with MMOFs provides a sustainable pathway for CO_2 conversion using green electricity under mild conditions, reducing the need for high temperatures or pressures typically required in thermal catalysis. Although still underexplored, MMOFs have shown considerable potential for driving product selectivity in CO_2R to valuable products.[65] The UOR is an anodic reaction requiring a lower potential (0.37 V) than the OER, making it energetically favorable to be coupled with the HER with lower electrical energy consumption. MMOFs enhance the sluggish six-electron kinetics of the UOR, improving efficiency.[66,67] Breaking the $N\equiv N$ bond to convert N_2 into NH_3 demands

significant energy due to the bond stability. MMOFs, acting as Lewis acids, provide active sites for the NRR, facilitating this transformation.[68,69]

MMOFs are effective in supercapacitors and batteries, addressing key challenges related to high specific energy storage and high-power density. Known for their fast charge–discharge rates and high-power density, supercapacitors must overcome their low energy density limitation. MMOFs help expand the potential window and specific capacitance, boosting energy density.[70–76] Lithium-ion batteries (LIBs) have high energy density but require optimization for power density. MMOFs enhance LIB performance by balancing these two factors and improving specific capacity.

MMOFs are effective heterogeneous catalysts, with better performance than the corresponding SMOFs. MMOFs have shown promise in oxidation reactions, CO_2 transformations, and other catalytic processes and factors such as turnover number (TON), turnover frequency (TOF), stability and yield determine their catalytic efficiency.[77–79] Photocatalytic applications of MMOFs include water splitting, CO_2 reduction, and dye degradation. Their effectiveness is influenced by factors such as light absorption, band energy, and reaction yield.[16,80–83]

The performance of MMOFs in sensing applications, particularly using electrochemical or fluorometric response, is evaluated based on the limit of detection (LOD), which reflects the lowest concentration at which a substance can be detected. Challenges include the uniform distribution of metals and the development of suitable synthesis procedures.[84] Key challenges in pharmaceutical applications include biocompatibility, toxicity, and synthesis complexity. The cytotoxicity of different metal elements poses safety concerns, while large-scale production requires maintaining uniformity and structural integrity.[85,86] MMOFs are also employed in removal, separation, and adsorption applications. Challenges in these areas include stability, uniform metal distribution, and minimization of environmental impacts.[87]

Energy-related applications, particularly electrocatalysis, dominate the field of MMOFs due to the general observation of synergistic effects between metals and the higher electrical conductivity of pyrolysis-derived MMOFs. Non-precious metals like Ni, Fe, and Co are preferred candidates due to their cost-effectiveness and electrocatalytic activity. Less-studied applications, such as medicinal, sensing, and pollutant removal, are emerging areas with growth potential, requiring further research and development. This review underscores the versatility of MMOFs and highlights areas for future investigation to take advantage of MMOF properties in various fields. The following sections will describe MMOFs and their derivations, classified based on the metal element presented in the highest proportion in the composition of the material.

4. Iron-based MMOFs

Among the various types of MMOFs, Fe-based frameworks have seen rapid development and have attracted considerable interest from the scientific community. As the fourth most abundant element in the Earth's crust, Fe is widely available

and cost-effective, making Fe-based MOFs an attractive option for various applications. Furthermore, the low toxicity of Fe enhances its suitability for pharmaceutical uses, while its paramagnetic properties make Fe(III)-based MOFs highly effective in magnetic resonance imaging. Beyond pharmaceuticals, Fe-MMOFs find applications in sensing, catalysis, and other areas. In MOFs, Fe^{3+} ions act as Lewis acids, coordinating with oxygen-containing ligands that serve as Lewis bases. This robust coordination bond between Fe^{3+} and oxo ligands provides Fe-MMOFs with excellent stability in both aqueous and organic solvents, as well as high thermal and chemical resilience. When combined with other metals, Fe-based MMOFs benefit from the unique properties of each metal, expanding their potential applications, as will be discussed below.[88–90]

The incorporation of additional metals into Fe-MMOFs can eventually result in an enhancement of their surface area, pore size, and density of open metal or catalytically active sites, improving in this way their drug delivery capabilities. Enlarged pores in these frameworks facilitate larger drug adsorption capacity and release efficiency. As an example, M-MIL-100(Fe), a bimetallic MOF, was employed by Muder Al Haydar et al. as a carrier of the drug aceclofenac, which has low solubility in aqueous media. Compared to monometallic MIL-100(Fe), the incorporation of a second metal expanded the MOF pore size, enabling enhanced drug adsorption, and was beneficial for providing an adequate dose within the body. The aceclofenac loading capacity of MIL-100(Fe) was 27%, whereas the loading capacity was 37% in Ca(I)-MIL-100(Fe), 57% in Mn(II)-MIL-100(Fe), and 59% in Zn(II)-MIL-100(Fe), which exhibits the superior activity of bimetallic MOFs compared to monometallic MOFs. This highlights the superior performance of Fe-based MMOFs in drug delivery compared to their monometallic counterparts due to the higher loading of Fe-MMOFs.[91]

Fe-MMOFs demonstrate excellent electrochemical sensing properties due to their two available oxidation states, Fe^{2+} and Fe^{3+}, and their synergistic effect with other metals can further induce selectivity toward target detection.[92,93] The swing between these two states enables enzyme-like catalytic activity, making Fe-MMOFs valuable components in biosensing platforms. In this context, an Fe_3Ni-MOF (BDC as the linker) synthesized by Wang and coworkers demonstrated peroxidase-like activity. Also, Ni can enhance peroxidase-like activity and improve electron transport between H_2O_2 and 3,3',5,5'-tetramethylbenzidine (TMB), facilitating oxidation of Fe^{2+} to Fe^{3+} and generating more ˙OH radicals. This improvement enabled ultra-sensitive detection of H_2O_2, which was further used to develop a glucose detection system.[92] In another case, Yuan et al. developed a trimetallic MOF, FeCoNi-MOF (BDC as linker), for detecting thiophenol. The XRD pattern of FeCoNi-MOF after immersing in aqueous solution at pH 2, 7, and 12 for 24 h showed no characteristic changes in its pattern, thus showing its stability for sensor applications. This MOF exhibited both peroxidase- and oxidase-like activity, catalyzing the oxidation of TMB and directly oxidizing chromogenic substrates to oxTMB, resulting in a blue product. The synergistic effect and efficient electron transfer among Fe, Co, and Ni make FeCoNi-MOF a highly sensitive and stable sensor for detecting biomarkers

in water samples. The intensity of the EPR signal for trimetallic MOFs is stronger than for bimetallic FeCo, FeNi, and CoNi-MOFs and the bimetallic counterparts have a stronger EPR signal than the monometallic Fe, Co and Ni-MOFs, indicating synergistic effects among Fe, Ni, and Co in FeCoNi-MOF for activation of H_2O_2. Its rapid reaction speed demonstrated the potential of Fe-MMOFs for colorimetric sensing applications.[94] In another instance, $NH_2MIL-101(Fe)@Ag$ exhibits nearly 100% bactericidal activity against high concentrations of Staphylococcus aureus and Escherichia coli. DFT simulations have indicated that electrons are transferred from Ag to Fe-MOF due to lower Ag work functions and higher Fermi energy compared to Fe-MOF. Also, incorporation of Ag has little impact on the adsorption energy of Fe-MOF, which indicates that O_2 can be adsorbed on the $NH_2MIL-101(Fe)@Ag$ surface and produce more reactive oxygen species (ROS) upon irradiation at 880 nm.[95]

Fe-MMOFs are among the most extensively studied materials for the electrocatalytic OER due to their synergistic effects with other metals, which can result in highly efficient active sites.[96–99] The ability to release protons and alter the MOF structure significantly impacts the active site density and overall catalytic performance. The mixed valence states of Fe, such as Fe^{2+} and Fe^{3+}, contribute to improved electronic interactions with other metal ions, enabling enhanced intermediate production (e.g., *OOH in THE OER) with lower energy barriers. In one example, Co_4Fe_6-MOF (BDC as the linker) demonstrates a low over-potential (241 mV at 10 mA cm^{-2}) and a Tafel slope of 30.1 mV dec^{-1} for the OER.[100] The enhanced OER activity is attributed to the optimal Fe/Co ratio that increases adsorption/desorption processes and decreases crystallinity, yielding abundant active sites.[100] DFT calculation indicates that defect formation energies decrease as the Co/Fe ratio diminishes, corresponding to the introduction of defects and disordered atom architectures in the MOF. The defect structure can augment the number of active sites and high charge transport, and the incorporation of Fe ions can effectively optimize the electronic structure of metal Co nodes, thereby facilitating adsorption/desorption of OER intermediates. Also, the Co_4Fe_6-MOF shows a higher TOF value (1.04 s^{-1}) than the others, indicating its reinforced intrinsic activity in the OER process. In another example, PCN–Fe_2Co–Fe_2Ni, MMOF having simultaneously two different mixed metal clusters in the structure, either Fe_2Co-(μ-O)(CH$_3$COO)$_6$(H$_2$O)$_3$ or Fe_2Ni-(μ-O)(CH$_3$COO)$_6$(H$_2$O)$_3$, shows an overpotential of 271 mV and a Tafel slope of 67.7 mV dec^{-1}.[48] Also, no changes in the PXRD patterns of PCN–Fe_2Co–Fe_2Ni in a broad range of pH values from 1 to 14 demonstrate its stability. The higher OER activity was related to the lower ionization potential of the mixed metal cluster, increased electron density, and synergistic effects between Co, Ni, and Fe.[48] The density of states (DOS) of Co and Ni 3d orbitals for mixed-metal mixed-cluster MOFs exhibits a weaker negative shift compared to the PCN-250-Fe_2Co and PCN-250-Fe_2Ni counterparts, which indicates that incorporation of another Fe_2M cluster decreases the energy of Co and Ni atoms and leads to Co and Ni atoms receiving higher electron density in PCN–Fe_2Co–Fe_2Ni. Also, a high TOF value of 0.068 s^{-1} at 350 mV reflects their excellent intrinsic activity of mixed-

cluster MOFs compared to PCN-250-Fe$_2$Co (0.024 s^{-1}) and PCN-250-Fe$_2$Ni (0.038 s^{-1}). In another illustrative example, the Fe-MMOF derivative of MIL-88A(Fe) (fumaric acid as the linker) was prepared under hydrothermal conditions in the presence of Ni(NO$_3$)$_2$ and Ce(NO$_3$)$_3$ and urea. The resulting 30%CeNiFe-LDH obtained by etching of a CeNiFe MMOF exhibits superior OER activity due to Ce strong affinity for oxygen donors and its synergistic interaction with Fe and Ni, facilitating electron transfer.[101] Although the 3d orbitals of Ni and Fe play a critical role in OER activity, the Fe 3d orbitals cross the EF, supporting the stabilization of O-related species, while the Ni 3d band synergy with Fe and Ce at the commensurate positions can induce high electroactivity during the OER. Meanwhile, the Ce 4f orbitals overlap with Ni and Fe 3d orbitals, which can modulate the electronic structure and enhance electron transfer throughout the catalyst surface. In one of the examples, MIL-53(Fe) (BDC as the linker) was modified mechanochemically by adding Ni(OAc)$_2$ and Co(NO$_3$)$_2$. Ball milling decreases the particle size of MIL-53(Fe), while the Ni and Co metal salts are deposited on the external surface of the MOF crystallites. The resulting trimetallic Fe/Ni/Co MOF achieves a low overpotential of 180 mV (10 mA cm^{-2}) due to Fe–O–Ni/Co bonding, as supported by XANES and EXAFS analyses.[102] Regarding reported examples of V-MMOFs in electrocatalytic water splitting, it was found that the presence of V was favorable due to its multiple valences, optimizing the binding energy of redox reaction intermediates, lowering the overpotential and enhancing the electrocatalytic activity. For instance, various M$_2$V-MOFs (M = Zn, Co, Fe, Mg, and Ni; BDC as the linker) containing trimetallic clusters were explored for electrolytic water splitting in 1 M KOH.[103] Interestingly, these M$_2$V-MMOFs were prepared by the so-called pore-space-partition (PSP) strategy that consists of performing the solvothermal synthesis of the mixed metal MOF adding, besides the BDC linker, 2,4,6-tris(4-pyridyl)-1,3,5-triazine.[103] The bulky triazine linker occupies the pores generated in the framework by the coordination of the M$_2$V metal node and BDC dividing the internal space into three compartments while adding further structural robustness due to the additional coordination with the rigid triazine molecules. The electrochemical data show that the OER activity of Fe$_2$V-MOF has a calculated TOF of 0.0243 s^{-1} and an R_{ct} of 0.67 Ω measured by EIS characterization, resulting in better electrochemical activity than the other M$_2$V-MOFs containing other metals accompanying V and even compared to the commercial IrO$_2$ catalyst, which has an overpotential of 330 mV.[103] Furthermore, at a scan rate of 5 mV s^{-1}, both Fe$_2$V-MOF (overpotential = 198 mV at a current density of 10 mA cm^{-2}) and Mg$_2$V-MOF (overpotential = 195 mV at a current density of 10 mA cm^{-2}) have great performance for the HER in alkaline media. Notably, Mg$_2$V-MOF also exhibits HER activity in acidic media with an overpotential of 215 mV at a current density of 10 mA cm^{-2}. Also, Mg$_2$V-MOF has the highest C_{dl} (2.38 mF cm^{-2}) among M$_2$V-MOFs. Besides remarkable activity, both Fe$_2$V-MOF and Mg$_2$V-MOF exhibit long-term stability at a current density of 10 mA cm^{-2} for 12 h after 5000 cycles. The superior activity and stability of Fe$_2$V-MOF and Mg$_2$V-MOF were rationalized as derived from a combination of positive effects, including: (i)

higher valence states introduced by the presence of V that improve the electrostatic interactions with the linkers and establish a synergistic effect with the other metal ions at the node, as can be experimentally assessed by XPS analysis, (ii) higher hydrophobicity that favors bubble evolution during water electrolysis by decreasing the surface tension, (iii) the additional triazine linker at the pore space that further stabilizes the structure, particularly under operational pH conditions and electrochemical stress, and (iv) a decrease in the Gibbs free energy of the rate-determining transition state due to the effect of vanadium stabilizing the reaction intermediates, resulting in better electrocatalytic activity.[103] In another instance, tetra-metallic NiFeCoV-MOF-74 demonstrates an overpotential of 266 mV at a current density of 10 mA cm^{-2}, which is superior to its bimetallic and trimetallic counterparts. Due to the effective synergy among tetra-metals, electron transport from V^{4+} to Ni^{2+} and Co^{2+} is facilitated, and NiOOH and CoOOH on the surface act as the active sites.[104]

Furthermore, Fe-MMOFs have significant potential in supercapacitors and batteries. The synergistic effects of Fe with other metals enhance OH$^-$ adsorption, charge transfer, and conductivity.[105] In one example, the solid derived from CoFe$_2$-MOF (BDC as the linker) demonstrates improved storage capacity due to synergistic interactions, increased active sites, and higher conductivity.[53] Electronegativity facilitates charge transfer with the electrolyte, which is a crucial process in Li$^+$ ion batteries.

Fe-MMOFs serve as efficient catalysts due to their Lewis acidity, which enhances the activity and selectivity of catalytic processes. The presence of Fe in MOF structures results in high TOF values and reaction rates by decreasing electron density around neighboring metal ions, and oligomerization of Fe-oxo clusters is disfavored by the interaction with other metal ions. In one report, FCN–K MMOF derivative obtained by calcination under N$_2$ atmosphere at 550 °C from Fe–Co–Ni-MMOF with BDC linker promoted by K due to the augmenting surface basicity which leads to the increasing alkali-metal content, and shows exceptional performance in CO$_2$ hydrogenation via efficiency of CO$_2$ conversion of 47.5% and selectivity of light olefins 46.8% which is attributed to the synergistic effect between Fe and other metal ions within the MOF-derived solid, boosting catalytic activity. Fe species can boost the binding force of Fe–O and Fe–C, enhancing the stability of reactive phases, and supporting the construction of Fe$_5$C$_2$.[106] In another instance, bimetallic-derived FeMn-MOF was applied for non-radical oxidation of peroxydisulfate (PDS) and illustrated the performance of 96.5% within 10 min for the degradation of sulfamethoxazole (SMX). The Fe$_3$O$_4$/Mn$_3$O$_4$ interface, which can contain Fe–Mn bonds, could effectively boost PDS adsorption and electron-transport capacity.[107] Their high stability at pH = 2 is also due to the strong structural integrity and consistent redox cycling of Fe and Mn active sites anchored on biochar. This prevents metal leaching and maintains effective PDS activation. Furthermore, from DFT simulations, the adsorption energy of PDS on Fe$_3$O$_4$/Mn$_3$O$_4$ with Fe–Mn connections is 2.0 eV, which is higher than that of the Fe/Mn–O bonding model (1.7 eV), indicating enhanced PDS activation.[107] In addition, the

high valence (III) can also provide adequate stability to the framework structure for any application if there is an adequate Cr molar ratio, besides the expected synergistic effect derived from the combination with other metal ions such as Fe.[77] As one example, the catalytic activity of bimetallic MIL-101(Cr/Fe) (BTC as linker) for the Prins reaction between formaldehyde and β-pinene was studied and found to be higher than that of monometallic MIL-101(Cr). The enhanced catalytic activity is due to the complementary role of Cr^{3+} and Fe^{3+} ions, in a way that Cr^{3+} provides thermal and structural stability that is lacking for MIL-101(Fe), while the presence of Fe^{3+} ions in the MMOF results in an increase of the activity of the Lewis acid sites, therefore enhancing catalytic activity and stability.[77]

Fe-MMOFs are widely used in photocatalysis, where charge transfer from Fe to other metals enhances the active site availability and improves photocatalytic charge separation efficiency.[108–111] The multiple valence states of Fe facilitate strong interactions with donors like H_2O, optimizing photocatalytic reactions. This is exemplified by NH_2-MIL101(Fe, Co), with an optimal Co/Fe ratio of 0.15, which can achieve a nitrogen photo-fixation efficiency of 335.7 μmol g^{-1} h^{-1}. The synergistic interaction between Co and Fe strengthens light harvesting, lowers the conduction band (CB) potential, and activates N_2 more effectively. Monometallic Fe-MOF has a strong PL peak at 460 nm, which can be related to the high electron–hole recombination rate. However, the PL intensities in bimetallic MOF samples are weaker than those of monometallic MOF, that is related to the doping of Co, can suppress the recombination electron hole pairs. Moreover, bimetallic MOFs contain more oxygen vacancies that can be useful in the adsorption and activation of N_2.[109] In another instance, doping of Mn into MIL-53(Fe) illustrates that the incorporation of Mn into the MOF can reduce the band gap and result in better removal of crystal violet (CV) with a performance of 99.01% under a 100-W xenon lamp. In conclusion, for these materials in the photo-Fenton reaction, Mn^{2+} can promote the generation of $\cdot$OH radicals and Fe^{2+}. Furthermore, Fe^{2+} swiftly activates H_2O_2 and generates radicals in the case of CV degradation.[112]

From the above precedents, it can be concluded that Fe-MMOFs continue to be among the most researched MMOFs for a wide range of applications. In the case of biomedicine, Fe-MMOFs enhance drug delivery through increased pore size, higher cargo loading, and the immobilization of active sites. Fe-MMOFs have been widely used in electrochemical sensing, taking advantage of the various Fe oxidation states and the enzyme-like peroxidase/oxidase activity of these materials, combined with synergistic interactions with secondary metals. Regarding pollutant removal and adsorption, the Lewis acidity and structural robustness make Fe-MMOFs among the most suitable materials. However, among all the applications, Fe-MMOFs are mostly researched for their electrocatalytic activity with a focus on the OER and novel, promising developments in the UOR, HER, and other reactions. Also, the swing between two different Fe oxidation states and synergistic effects with other metals are very suited for this use, the enhanced activity deriving from high active site density and facile charge transfer, which results in low reducing overpotentials. Emerging

applications of Fe-MMOFs in supercapacitors and batteries leverage the ability of Fe to undergo charge transfer processes and active site optimization. Regarding catalysis, Fe-MMOFs exhibit high TOF values and selectivity due to the Lewis acid behavior of Fe ions and electron density modulation through interaction with other transition metal ions. In photocatalysis, Fe-MMOFs often exhibit enhanced activity through more efficient light harvesting, efficient charge separation, availability of multiple oxidation states, and d-orbital electron dynamics by interaction with the other metals present in the MMOF material. Fe incorporation into MMOFs enhances their stability and functionality, enabling efficient removal of pollutants from aqueous and gaseous environments. In all these applications, the use of Fe-MMOFs with Fe as the main metal has the advantage of cost-effectiveness due to its abundance and affordability, making Fe-MMOFs economically attractive for large-scale applications. In addition, the low toxicity allows their use in biomedical applications for drug delivery. Another general effect of the presence of Fe on the MMOF is the robustness of most of the materials due to the strong coordination bonds and the high coulombic charge of Fe^{3+}, both factors contributing to the structural stability in various solvents and under thermal treatment. Overall, the ability of Fe-MMOFs to combine with other metals opens avenues for a multitude of diverse applications. This review underscores the importance of Fe-MMOFs, particularly in sensing, medicinal, pollutant removal, and electrocatalysis applications, in which the intrinsic properties of Fe and synergy with other metals contribute to superior performance of the resulting Fe-MMOF. The applications of Fe-MMOFs are summarized in Table 1, illustrating the intense research on this type of material. This positions Fe-MMOFs as crucial materials for advancing sustainable and high-performance technologies. Further, Table 1 provides an extensive comparison of Fe-MMOFs amid diverse applications for their performance. Although numerous Fe-MMOFs demonstrate their efficiency for energy applications due to their electro-active intrinsic nature, their performance toward removal applications can also be promising compared to other MMOFs. Table 1 presents various types of Fe-MMOFs and their corresponding metal contributions, as well as their applications and efficiencies, to inform future research. Their synergistic interactions with Ni and Co represent one of the most favorable engineering approaches for constructing electrocatalysts and photocatalysts. Also, their synergistic effects with Mn can be further explored, especially in energy storage and conversion systems. In the future, Fe-MMOFs can not only be explored for less investigated applications, but also can be studied for optimizing the Fe content. Finding appropriate Fe content compared to other metals can especially affect their performance, notably in catalysis.

5. Nickel-based MMOFs

Nickel-based MOFs (Ni-MMOFs) have gained significant attention due to their remarkable properties, low cost, environmental compatibility, and corrosion resistance in alkaline environments. Very frequently, Ni-MMOFs also enjoy sufficient

Table 1 Summary of the application of Fe-MMOFs or their derived composites or materials, indicating their efficiency[a]

Fe-MMOF	Other metals	Application	Efficiency	Ref.
NiFeMo-MOF	Ni/Mo	Electrocatalyst/water splitting	C.d: OER and HER: 50 Cell voltage: 10/O.v: OER: 239 and HER: 119/T.f: OER: 87.0 and HER: 58.3/C.v: 1.50	113
$Fe_2O_3/ZnCo_2O_4$	Zn/Co	Electrocatalyst/water splitting	C.d: OER and HER: 10 Cell voltage: 10/O.v: OER: 212 and HER: 44.8/T.f: OER: 41.2 and HER: 35.8/C.v: 1.44	114
0.04Ru/FeCo-MOF	Ru/Co	Electrocatalyst/water splitting	C.d: OER: 50 and HER: 10 cell voltage: 10/O.v: OER: 309 and HER: 180/T.f: OER: 84.0 and HER: 146/C.v: 1.498	115
Co_4Fe_6-MOF	Co	Electrocatalyst/OER	C.d: 10/O.v: 241/T.f: 30.1	100
NiFe-MOF	Ni	Electrocatalyst/OER	C.d: 100/O.v: 277/T.f: 73	116
Fe_2Ni_1-MOF-TDC	Ni	Electrocatalyst/OER	C.d: 10/O.v: 211/T.f: 40.3	117
$Fe_{0.75}Ni_{0.25}S_2$	Ni	Electrocatalyst/OER	C.d: 10/O.v: 247/T.f: 47.6	118
$FeCo_{0.5}Ni_{0.5}$-LDH	Ni/Co	Electrocatalyst/OER	C.d: 10/O.v: 248/T.f: 38	119
$CoNiFeO_x$-NC	Ni/Co	Electrocatalyst/OER	C.d: 50/O.v: 265/T.f: 64.1	120
CoNiFeP-YSNSs	Ni/Co	Electrocatalyst/OER	C.d: 10/O.v: 261/T.f: 49.5	121
FeCoNi@NC	Ni/Co	Electrocatalyst/OER	C.d: 10/O.v: 285/T.f: 69.6	122
$FeCoNi(OH)_3(BDC)_{1.5}$	Ni/Co	Electrocatalyst/OER	C.d: 1000/O.v: 284/T.f: 29.5	123
MIL-59(FeNi)/Co NSs	Ni/Co	Electrocatalyst/OER	C.d: 20/O.v: 216/T.f: 38.46	59
M-NiA-CoN	Ni/Co	Electrocatalyst/OER	C.d: 10/O.v: 180/T.f: 41	102
FeCoNi-BHT	Ni/Co	Electrocatalyst/OER	C.d: 10/O.v: 266/T.f: 88	124
$FeNi_2Co_1$-MOF	Ni/Co	Electrocatalyst/OER	C.d: 10/O.v: 143/T.f: 68	125
30%CeNiFe-LDH	Ni/Ce	Electrocatalyst/OER	C.d: 10/O.v: 242/T.f: 34	101
$PCN-Fe_2Co-Fe_2Ni$	Ni/Co	Electrocatalyst/OER	C.d: 10/O.v: 271/T.f: 67.7	48
$(FeNiCoCrCu)_3O_4$	Ni/Co/Cr/Cu	Electrocatalyst/OER	C.d: 10/O.v: 270/T.f: 49	66
$(FeNiCoCrCu)_3O_4$	Ni/Co/Cr/Cu	Electrocatalyst/UOR	C.d: 10/O.p: 1.35/T.f: 33	66
FLaN-MOF	La	Battery/LIBs	C.d: 100/capacity: 337/cycle: 100	126
Fe–Mn–O/C	Mn	Battery/LIBs	C.d: 100/capacity: 1294/cycle: 200	127
$Fe-Fe_{0.33}Mn_{0.67}O/C$	Mn	Battery/LIBs	C.d: 1000/capacity: 626.8/cycle: 1000	128
NiFe/Mn-MOF	Ni/Mn	Supercapacitor	S.p: 1640/C.d: 1.0 (5000 cycle)/E.d: 75/P.d: 1166/retention: 94%	129
$CoFe_2$-MOF	Co	Supercapacitor	S.p: 112.1/C.d: 1.0 (12 000 cycle)/E.d: 56.2/P.d: 1091.5/retention: 97.91%	53
NH_2-MIL-88B ($Fe_{0.6}In_{0.4}$)	In	Photocatalyst/Cr(VI) reduction	86.83%/bandgap: 2.58	130
NM-Fe-0.15Co	Co	Photocatalyst/N_2 reduction	NH_3 evolution rate: 335.7 μmol g^{-1} h^{-1}	109
10%Ni/Fe-MOF	Ni	Photocatalyst/dye degradation	96%/Bandgap: 2.55/R^2: 0.98683/reuse: 5 cycles	131
Fe/Ni-T120	Ni	Photocatalyst/CO_2 reduction	CO evolution rate: 9.74/CO selectivity: 92.1%/bandgap: 1.69/AQE: 0.057%	132
Fe–Cu-T130	Cu	Photocatalyst/CO_2 reduction	CH_4 generation rate: 499.2/bandgap: 1.51/AQE: 0.0011%/reuse: 5 cycles	133
$Fe_{0.02}Ni_{0.10}-Co_{0.15}$-PCN-250	Ni/Co	Photocatalyst/CO_2 reduction	CO yield: 299/bandgap: 1.92	134
Fe_2Zn-MOF	Zn	Catalyst/imine synthesis	97%/80 °C/air/12 h/reuse: 5 cycles	135
MIL-101(Al/Fe)–NH_2(15 : 1)	Al	Catalyst/Knoevenagel condensation reaction	100%/90 °C/BDA/90 min/reuse: 5 cycles	136
Co/Fe-MOF	Co	Catalyst/synthesis of N-pyridinylamides	94%/DTBP/120 °C/24 h/reuse: 5 cycles	137
MIL-101(Cr/Fe)	Cr	Catalyst/Prins reaction	63.75% (for Nopol)/selectivity: 80%/reuse: 4 cycles	77
FCN–K(a)	Ni/Co	Catalyst/CO_2 hydrogenation	47.5%/320 °C/selectivity: 46.8%	106
MOF-(Al, 5Cr, 3Fe)	Al/Cr	Catalyst/aromatization of p-xylene	21%/450 °C/selectivity: 91%/reuse: 3 cycles	138
Fe Pt Rh MOF	Pt/Rh	Sensing/detection of heart-type fatty acid binding protein	LOD of 0.01–100 ng mL^{-1}	139
S-FCM-MOF@PCL	Co/Mn	Sensing/detection of bisphenol A and S	LODs (2.57, 2.91 μM)	140
Fe/4Cu-MOF	Cu	Sensing/selective colorimetric detection of *Salmonella typhimurium* in food	LOD of 1.0×10^2 CFU mL^{-1}	141
Fe/Ni-MOFs	Ni	Sensing/detection of thiamphenicol	LOD: 0.030 and 0.031 nM	142

Table 1 (Contd.)

Fe-MMOF	Other metals	Application	Efficiency	Ref.
Fe$_2$Ni MIL-88B	Ni	Sensing/selective detection of dopamine	LOD of 0.40 μM (S/N = 3) and higher sensitivity of 124.7 μA mM^{-1} cm^{-2}	143
Fe/Co-MOF	Co	Removal/toxic metals	Absorbance of samples: 64.5%	144
Fe–Mg MOF	Mg	Removal/heavy metal	Maximum adsorption capacity of Pb^{2+} (196 mg g^{-1})	145
FeCu-MOFs	Cu	Removal/adsorbents for gaseous elemental Hg removal	Equilibrium adsorption: 12.27 mg g^{-1}	146
UiO-66(Fe/Zr)	Zr	Removal/removal and immobilization of Se	Adsorption capacity for Se(IV) and Se(VI): 196 mg g^{-1} at pH = 3 and 258 mg g^{-1} at pH = 5	147
Ag–Fe MOF	Ag	Removal/Cd and Cu removal	Cd(II) and Cu(II) adsorption: 265 and 213 mg g^{-1}	148
Mn–Fe MOFs	Mn	Removal/reductive removal of Cr(VI)	Initial Cr(VI) concentration: 20 mg L^{-1}, and 10 mg of photocatalyst within 30 min	149
PCN-250(Fe$_2$Ni)	Ni	Adsorption and separation/SO$_2$	SO$_2$ uptake: 8.64 mmol g^{-1} at 0.1 bar and 298 K	150
FeNi$_x$-BDC	Ni	Adsorption and separation/organic dyes	2.472 vs. 1.188 min^{-1} for MB; 0.616 vs. 0.421 min^{-1} for MO	151
Cu/Fe-BTC	Cu	Adsorption and separation/U(VI)	Optimum pH: 7.0 adsorption capacity: 354 mg g^{-1}	152

[a] C.d: current density given in A g^{-1} or mA cm^{-2} for energy applications; O.v: overpotential given in mV; T.f: Tafel slope given in mV dec^{-1}; C.v: cell voltage given in V; O.p: onset potential given in V and S.p (specific capacitance) is given in F g^{-1}, C g^{-1}, and mAh g^{-1}; E.d: energy density given in Wh kg^{-1}; P.d: power density given in W kg^{-1}; all percentages in the photocatalyst or catalyst represent the yield, conversion or any efficiency of MMOFs; for further details, see the references; bandgap given in eV; AQE: apparent quantum efficiency; p.d: photocurrent density given in μA cm^{-2}; RT: room temperature; E_a: energy activation given in kJ mol^{-1}; for further details, see the references. YSNSs: yolk–shell nanospindles; NC: N-doped carbon; NS: nanosheets; BHT: benzenehexathiol; PCN: porous coordination network; FLaN: FeLaNa; NM: NH$_2$-MIL-101; Fe/Ni-T120 and Fe–Cu-T130: mixed metal MOFs prepared using dihydroxyterephthalic acid by solvothermal synthesis at the indicated temperature; FCN–K(a): FeCoNi MOF-derived carbon material incorporating K after calcination; PCL: polycaprolactone coated.

thermal and chemical stability. These characteristics, combined with a high specific charge capacity, make Ni-MMOFs versatile materials for applications in energy storage, catalysis, medicine, and sensing. Ni-MMOFs enhance their performance in these applications by incorporating additional metals, resulting in overall improvements in electrical conductivity, stability, and catalytic performance.[153,154]

Ni-MMOFs exhibit excellent stability and electrocatalytic performance in alkaline electrolytes, making them suitable for electrochemical sensors under certain conditions. Incorporating additional metals into Ni-MOFs enhances conductivity, active site density, and overall catalytic efficiency. In one example, NiCo-BTC/CC, a bimetallic MOF (BTC: 1,3,5-benzenetricarboxylate, as the linker) on carbon cloth (CC), significantly improves glucose sensing due to the presence of cobalt with enhanced oxygen adsorption and charge redistribution between Ni and Co ions. The synergistic effect between Ni and Co augments the activity and stabilizes the MOF architecture, which leads to premier sensitivity and stability compared to monometallic MOF counterparts. The bimetallic MOF exhibits a sensitivity of 2701.29 μA mM^{-1} cm^{-2} with a low detection limit of 0.09 μM.[155]

Ni-MMOFs are highly effective for removing heavy metals in aqueous media due to their large surface areas, expanded pore sizes, and augmented negative charge layers. This is exemplified by 2D Ni/Cd-MOF sheets (BDC as the linker) that outperform monometallic Ni-MOF in Pb^{2+} removal due to increased

electrostatic repulsion between the 2D MOF sheets, minimizing their stacking and improving the adsorption capacity. The bimetallic MOF exhibits a larger surface area and pore size, facilitating efficient contaminant removal. Stability at various pH illustrated that the bimetallic MOF is well maintained as evidenced by XRD results, but slightly collapses at pH 2. However, Ni-MOF and Ni/Cd-MOF in strong alkaline solutions led to the dissolution of 2D MOFs. Furthermore, bimetallic MOFs contain more crystal defects and vacancies. Thus, compared to monometallic Ni-MOF, bimetallic Ni/Cd-MOF shows a higher specific surface area and higher surface electronegativity, which leads to effective, rapid diffusion of Pb^{2+} to its active sites.[156]

In the pharmaceutical field and health monitoring, Ni-MMOFs demonstrate potential usage for antibacterial and wound-healing, and piezoresistive sensor applications.[157,158] As an example, NiCoCu-based MOF nanosheets (BDC as the linker) exhibit peroxide-like activity, catalyzing H$_2$O$_2$ to ˙OH radicals. This enhances antibacterial performance against methicillin-resistant *Staphylococcus aureus* and Gram-positive *Escherichia coli*. Copper incorporation accelerates wound healing due to the combination of 2D NiCoCu-MMOF, which has good stability in DMF solution and absolute ethanol, and H$_2$O$_2$ by facilitating electron transfer and stabilizing nanoenzymes, which results in preventing inflammation and accelerating skin growth. These results make NiCoCu-MMOF a promising candidate for therapeutic applications. The addition of Cu^{2+} as a cofactor enhances

the high POD-like activity, and Ni and Co can shorten the electron transport and ion diffusion pathways.[157]

Ni-MMOFs and their derived forms have been extensively studied as electrocatalysts in OER, HER, and UOR applications.[159–164] Incorporating metals such as Fe, Co, and Cu further enhances electron transfer, reduces overpotential, and increases active sites. In the OER, Ni-MMOFs benefit from the synergistic effects of multiple metals, which enhance electrical conductivity and optimize intermediate adsorption. In one example, Ni–BDC MOFs incorporating Er showed improved OER and HER activity. The $Er_{0.5}Ni$–BDC MOF exhibits an overpotential of 420 mV for the OER, while the ErNi–BDC MOF achieves an overpotential of 270 mV for the HER, demonstrating the impact of Er in enhancing active sites and improving electrocatalytic efficiency.[165] In another example, the $NiFe_{0.2}Co_{0.3}$-ZIF trimetallic MOF (2-methylimidazole as linker) exhibits an even lower overpotential of 216 mV and a Tafel slope of 23.25 mV dec^{-1} at 100 mA cm^{-2}. The synergistic interaction among Fe, Co, and Ni reduces the energy barrier and increases active sites, boosting OER performance. Also, the higher intrinsic activity of $NiFe_{0.2}Co_{0.3}$-ZIF in the OER was evidenced by achieving a TOF of 0.0259 s^{-1} compared to Ni-ZIF and $NiFe_{0.2}$-ZIF solids, both of which are below 0.01 s^{-1}.[166] In another instance, bimetallic NiFe-MOF-BF$_4^-$-0.3 NSs exhibit a low overpotential of 237 mV at a current density of 10 mA cm^{-2} with a Tafel slope of 41 mV dec^{-1} in alkaline media. Based on XPS analysis, electron transport from Ni or Fe to F in the counterion leads to better charge transfer and alters the coordination environment of metals, therefore accelerating OER kinetics in the electrochemical procedure and enhancing OER activity. Fig. 9 illustrates the theoretical calculations where the introduction of Fe into the monometallic Ni-based MOF leads to a conduction band closer to the Fermi level. During synthesis, Fe^{2+} ions are converted to Fe^{3+} ions and exchanged with some of the Ni^{2+} ions. Furthermore, the addition of counterions also augments the electron number close to the Fermi level which both Fe and counterions favor to a new electronic state which is evidenced by better conductivity and activity of the synthesized MOF. Also, achieving lower energy shifts for bimetallic counterion MOFs in comparison to monometallic and bimetallic MOFs can increase OER activity by regulating OH*, O*, and OOH* adsorption in an electrochemical procedure. A higher charge density and lower energy barrier are also important factors for better OER activity of NiFe-MOF-BF$_4^-$-0.3 NSs.[167]

In another example, $Ni_{0.5}Fe_{0.5}$-THQ exhibits better OER activity in comparison with Ni-THQ, $Ni_{0.8}Fe_{0.2}$-THQ, $Ni_{0.5}Fe_{0.5}$-THQ, $Ni_{0.2}Fe_{0.8}$-THQ, and Fe-THQ, as evidenced by a higher C_{dl} efficiency of 0.852 mF cm^{-2}, a larger ECSA of 21.25 cm^2, a higher mass activity of 175 mA mg^{-1} which is pertinent to the intrinsic activity of the MOF, and a higher TOF of 0.026 s^{-1}, as
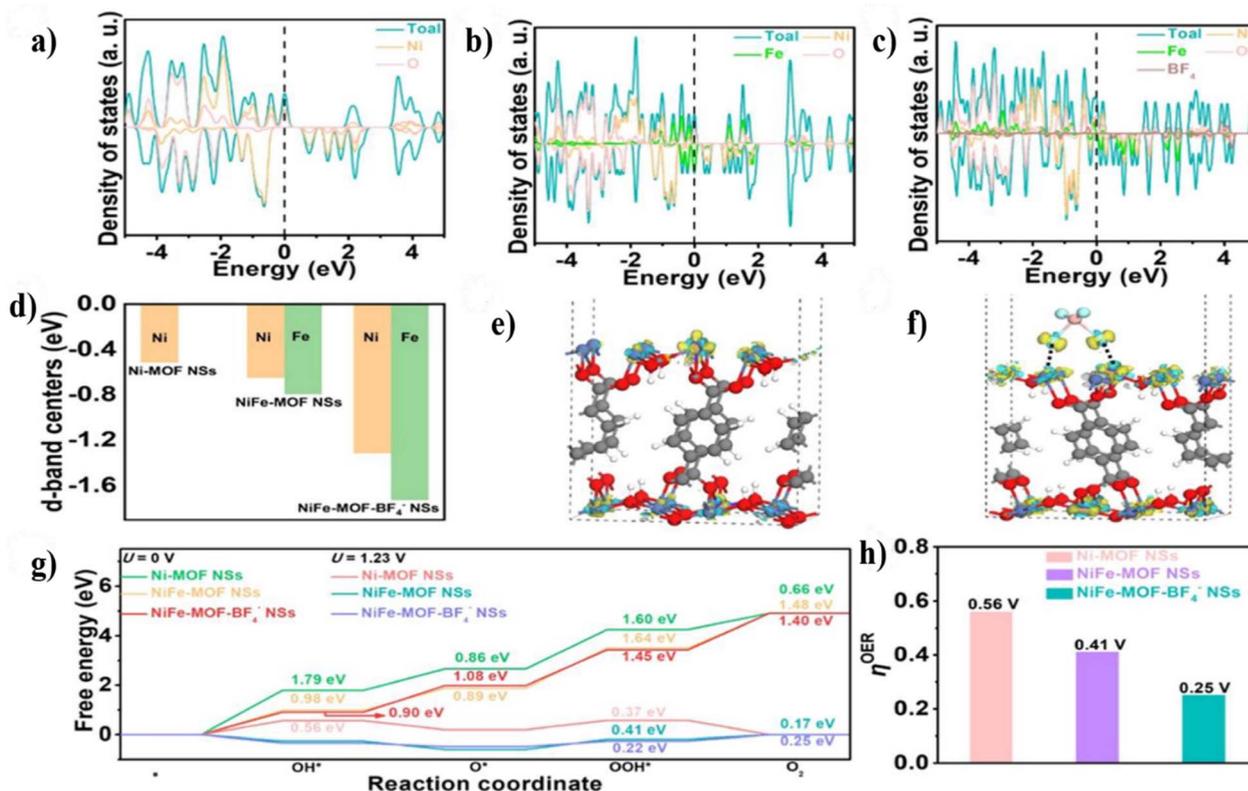

Fig. 9 DOSs of (a) Ni-MOF NSs; (b) NiFe-MOF NSs; (c) NiFe-MOF-BF$_4^-$ NSs; (d) d-band center of Ni in Ni-MOF NSs, and Ni and Fe in NiFe-MOF NSs and NiFe-MOF-BF$_4^-$ NSs; and the density difference of (e) NiFe-MOF NSs and (f) NiFe-MOF-BF$_4^-$ NSs with an isosurface value of 0.003 eV Å^{-3}. Yellow and cyan regions represent charge depletion and accumulation, respectively; (g) calculated free energy for the OER with Ni-MOF NS, NiFe-MOF NS, and NiFe-MOF-BF$_4^-$ NS surfaces at 0 and 1.23 V; and (h) η_{OER} comparison of Ni-MOF NSs, NiFeMOF NSs, NiFe-MOF-BF$_4^-$ NSs. Reproduced with permission from ref. 167, copyright 2022 American Chemical Society.
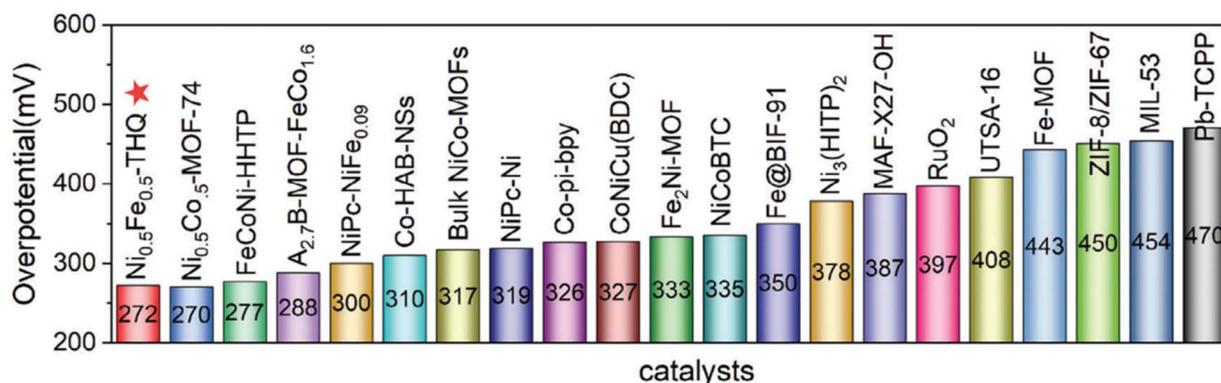
Fig. 10 Comparison of the performance of $Ni_{0.5}Fe_{0.5}$-THQ with other MOFs and commercial RuO_2 for OER applications. Reproduced with permission from ref. 168, copyright 2024 Wiley.

well as other catalysts performance exhibited in Fig. 10. The adsorption energy of OH^- species on iron sites is -0.54 eV in $Ni_{0.5}Fe_{0.5}$-THQ, which is lower than that on adjacent nickel sites, which is -0.05 eV, resulting in the Fe sites acting as active metal centers for the OER. Also, the synergistic effect between Fe and Ni in bimetallic MOFs can reinforce the OER activity by decreasing the energy barrier of the intermediate product. In addition, the highest d-band center of Fe sites in bimetallic MOFs illustrates strong adsorption capacity for species, which leads to higher OER activity due to the transport of d-electrons of the Ni site to the Fe site *via* d–π conjugation on the surface of the bimetallic MOF.[168]

In another pertinent example, NiCoFe–NDA (NDA: 1,6-naphthalenedicarboxylic acid) grown on NF showed a lower overpotential of 215 mV and a lower Tafel slope of 64 mV dec^{-1} at a current density of 10 mA cm^{-2} and higher C_{dl} compared to monometallic Ni–NDA/NF, Co–NDA/NF, and Fe–NDA/NF and commercial IrO_2. In addition, NiCoFe–NDA exhibited enhanced stability (a current density of 100 mA cm^{-2} *via* 6% decay after 50 h), as shown in Fig. 11. This enhanced performance in the OER application is related to the (i) lower coordination environment for NiCoFe–NDA (4-coordinated) *via* applying Fe also, $Fe^{2+/3+}$ can decrease overpotential by optimizing rate-determining steps, leading to better OER activity, which is provided by theoretical methods; (ii) synergistic effect between metal ions and the formation of metal oxyhydroxides, which is beneficial for OER application.[169]

High entropy MOFs have recently been explored due to their diverse synergistic effect between metals for electrocatalysis.[170] For instance, a penta-metallic high entropy MOF composed of Ni, Co, Zn, Fe, and Mo metals (HE-MOF) exhibits an over-potential of 254 mV at a current density of 50 mA cm^{-2}. High-entropy materials can minimize Gibbs-free energy but have flaws in the OER process due to the harsh synthesis conditions. They produce bulk forms in which adjacent nanoparticles of bulk high-entropy materials can overcome this demerit. Furthermore, the synthesis of ultrathin HE-MOFs due to rich active sites, synergy between metal ions, and high entropy can lead to better OER activity compared to their counterparts, as shown in Fig. 12.[171] Compared to other multi-metallic MOFs, Ni-

MMOFs have been less explored as heterogeneous catalysts, primarily because other metal ions often exhibit superior catalytic activity. Nevertheless, the incorporation of Ni alongside other metals can enhance catalytic performance by creating open metal sites and oxygen vacancies and by reaction inter-mediate stabilization. These features make Ni-MMOFs valuable for applications such as dehydrogenation and hydro-deoxygenation. One of the recent examples of Ni-MMOFs as an electrocatalyst is the use of a NiFe-GA (GA: gallate) bimetallic MOF for the OER, showing superior activity with overpotentials of 185 mV and 236 mV for 10 mA cm^{-2} and 100 mA cm^{-2} in 1.0 M KOH, respectively. This performance was attributed to the hexagonal structure of NiFe-GA, ample active sites, and strong d–p orbital overlaps between Ni, Fe, and oxygen, reducing activation barriers and enhancing catalytic efficiency.[172]

Similarly to the OER, the HER activity in Ni-MMOFs can also improve significantly upon the introduction of metals that shift the d-band center to lower energy levels. For example, $NiRu_{0.13}$-BDC, a bimetallic MOF, achieves remarkable HER activity with a remarkably low overpotential of 36 mV at 10 mA cm^{-2}. Ruthenium incorporation enhances electron interactions and modifies the Ni electronic structure, optimizing intermediate adsorption and facilitating H_2 release.[173] Regarding the UOR, Ni-MMOFs facilitate urea oxidation by generating highly oxidizing Ni^{3+} species that enhance electron withdrawal and boost catalytic activity. In one of the reports on multi-metallic Ni MOFs, Fc-NiCo-BDC (Fc denoted as ferrocene carboxylic acid) demonstrates superior UOR and OER activity due to ferrocene electronegativity, which enhances active site accessi-bility and reduces the bandgap of NiCo-BDC, improving elec-trical conductivity.[174] Control of the electronic density of Ni and Co using Fc plays a crucial role in adjusting the adsorption of reaction intermediates, which is essential for achieving high turnover frequencies. In this way, a NiMg-MOF-74-derived Ni–N–C catalyst containing single Ni atoms demonstrates a fara-daic efficiency of 90% in CO_2 reduction towards CO, high-lighting its potential for energy storage applications.[65] In this solid, the role of Mg was to dilute Ni in the MOF structure that upon transformation into the N-doped carbonaceous material, becomes isolated as single atoms, rather than forming Ni
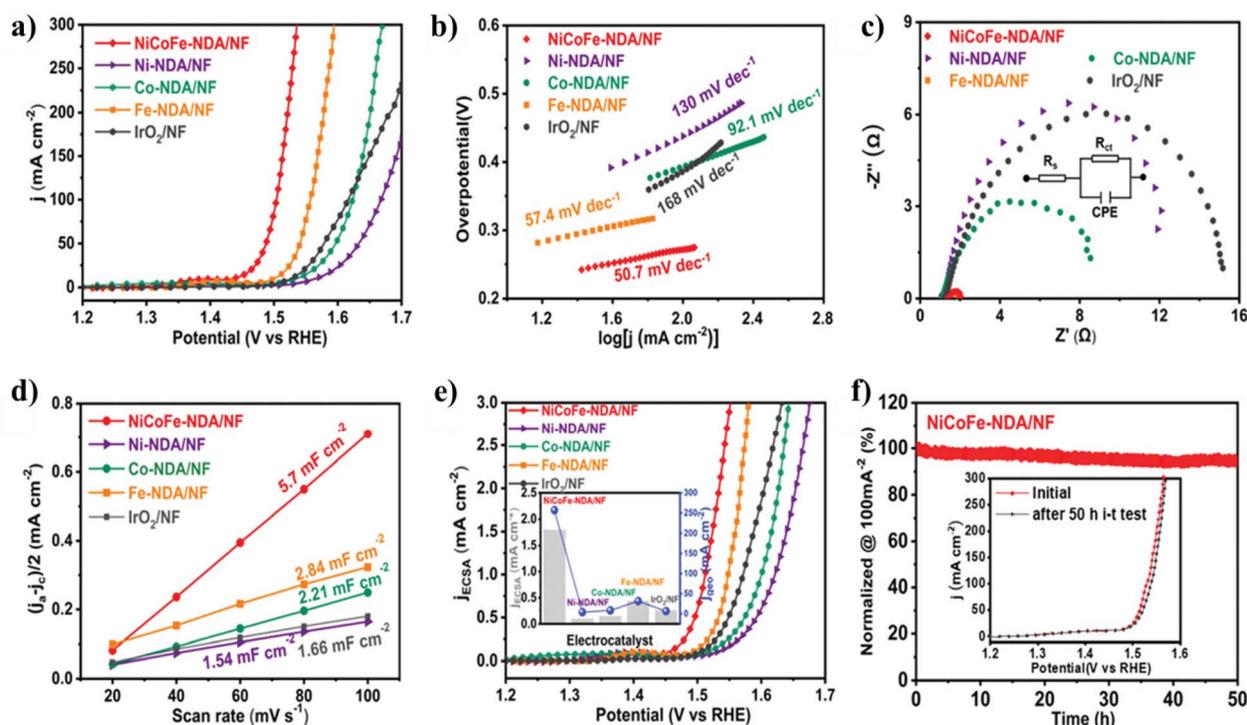
Fig. 11 Evaluating OER activity of NiCoFe–NDA/NF in terms of (a) LSV curves, (b) Tafel slope, (c) Nyquist plots, (d) C_{dl}, (e) ECSA-normalized LSV curve, and (f) chronoamperometric curves. Reproduced with permission from ref. 169, copyright 2021 Royal Society of Chemistry.

nanoparticles. The activity of Ni metal in MMOFs is fully investigated toward electrocatalysts. Reports demonstrate that Ni is one of the most vital metals for electrocatalysts in MMOFs. Due to the electroactive nature of Ni, this metal can be a pivotal candidate for electrocatalytic activity by reducing the overpotential and energy barrier of the RDS. Approximately, most of the Ni incorporation is pertinent to mixed Ni-FeMOFs, whose synergistic effect demonstrates higher electrocatalytic activity due to the lowering of overpotential by Fe and increased

conductivity by Ni. Furthermore, when the location of Ni is adjacent to the Fe and Co, can be considered to be a potential candidate for electrocatalysts for MMOFs engineering. For example, a Ni_5In_3-Fc/NF MOF, due to the synergistic effect between Ni and In, can optimize the electronic structure and the adsorption of intermediates, including *COOH and *CO, which lead to better CH_4 production with a faradaic efficiency of 76% and superior structural stability over a 16 000-second period. The incorporation of $FcDA^{2-}$ (ferrocene-
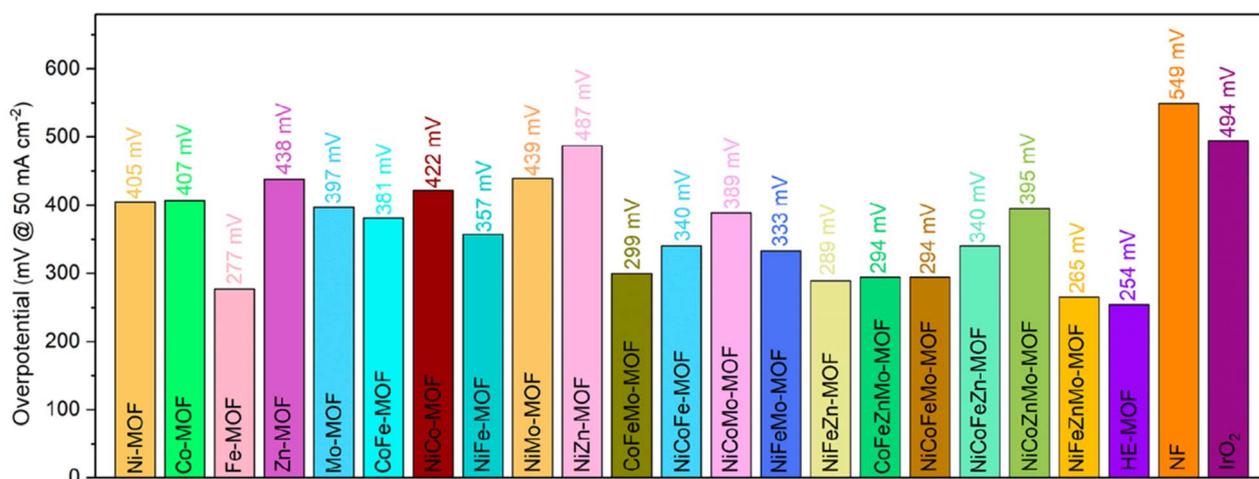

Fig. 12 Comparison of the overpotential of HE-MOF with other mono-, bi-, tri-, and tetra-metallic MOFs, bare NF, and commercial IrO_2 solids. Reproduced with permission from ref. 171, copyright 2022 American Chemical Society.

1,1′dicarboxylate) with π-conjugation and reversible redox features can support the electron conductivity and prompt catalytic selectivity. Based on DFT simulations, the *CO intermediate formation illustrated that Ni/In dual sites have a high energy barrier, validating its role as the rate-determining step for total reaction kinetics. Also, the Ni-only configuration illustrated that the lowest energy barrier for $*CH_4$ desorption leads to rich active sites and buffers subsequent reactions.[175]

Ni-MMOFs have demonstrated exceptional potential for energy storage applications, including batteries and supercapacitors, owing to their ability to enhance charge transport, increase specific capacitance, and generate abundant active sites.[70,176,177] In one of the studies in this area, a bimetallic Ni, Co MOF of 1,3,5-benzenetricarboxylic acid with an optimal 15%v Co submitted to *in situ* etching exhibits a specific capacity of 108.5 mAh g^{-1} at 0.5 A g^{-1}, with 84.3% retention over 6500 cycles reported. Its unique morphology, comprising aggregated nanowires, offers abundant active sites that facilitate charge transport and accelerate redox reactions through synergistic interactions.[70] In another study, a bimetallic NiMn sulfide derived from the corresponding bimetallic MOF-74 containing 2,5-dihydroxybenzene-1,4-dicarboxylic acid as the linker was transformed into the corresponding sulfide derivative by sulphuration of the mixed NiMn oxide resulting from the calcination of the MOF at 450 °C in air. NiMnS exhibits a specific capacitance of 2510.15 F g^{-1} at 1 A g^{-1} and 84.5% retention after 5000 cycles. The reason for this excellent performance is the mesoporous structures that increase the surface area and pore size, enhancing ion transfer rates and facilitating electrolyte access. XPS data confirm the presence of Ni^{2+} and Mn^{2+}, which enhance conductivity and provide redox activity for charge storage.[178] In a trimetallic phosphide supported on carbon derived from NiCoZn-MMOF-74, it was found that segregated ZnO plays the role of preserving the porous structure inherited from the MOF, while Ni and Co undergo phosphidization to form mixed NiCoP nanoparticles in intimate combination with ZnO. The material stores electrical energy through a mixed mechanism combining double-layer capacitance and faradaic charge storage, reaching energy densities of 44.6 Wh kg^{-1} at 1500 W kg^{-1} using a liquid electrolyte and 35.4 Wh kg^{-1} at 1500 W kg^{-1} with a quasi-solid-state electrolyte. The energy storage capacity was maintained at over 90% of the value of the fresh material after 5000 charge–discharge cycles. This NiCoZnP/C material illustrates the synergistic effects that can be derived from different roles played by the various metals.[176] The redox potential of Ni ions makes Ni-MMOFs among the most widely used materials for energy storage systems. Several conclusions can be drawn from the analysis of these reports, including: (i) prevalence of Ni metal: Ni-MMOFs account for 31.25% of total energy storage systems, highlighting the significance of this element in this field; (ii) Ni-CoMOFs correspond to approximately 75% of the Ni-MMOFs used in electrical energy storage systems implying synergistic interactions between Ni and Co, attributed to their appropriate redox potentials that allow reaching high specific capacitance, and (iii) the multiple Mn oxidation states complement Ni, resulting in enhanced charge transport and energy storage efficiency for NiMn-MMOFs. The

key features provided by Ni metal in Ni-MMOFs applied to energy storage are (i) mixed Ni^{2+}/Ni^{3+} valence states occurring at high potentials, enhancing electron availability, and supporting higher specific capacitance; (ii) occurrence of synergistic effects with other metals, such as the previously discussed Ni–Co and Ni–Mn pairs, improving conductivity, redox charge storage, and ion transfer rates; (iii) possibility of synthesizing materials with unique morphologies, such as nanowires and mesoporous frameworks providing a high surface area and exposure of abundant active sites for electrolyte interaction; and (iv) durability exhibiting a high energy retention percentage over multiple cycles to ensure long-term stability. Table 2 offers additional examples of Ni-MMOFs in energy storage, showcasing their versatility and potential for advancing next-generation battery and supercapacitor technologies.

Regarding thermal catalysis, a Ni-MMOF derivative containing a Ce/Ni atomic ratio of 1/3 was obtained by calcination of NiCeMOF (with trimesic acid as the linker) at 500 °C under a N_2 flow. The resulting derivative consists of rod-shaped mesoporous CeO_2 with high oxygen vacancy density supported on carbonaceous residue containing Ni nanoparticles. Ni–CeO_2/C demonstrates outstanding catalytic activity for hydrodeoxygenation of lignin model molecules, like vanillin, achieving a >95% conversion rate and 81.4% selectivity to 2-methoxy-4-methylphenol with four-cycle reusability. This performance is attributed to the synergistic effect of Ce and Ni, which increases oxygen vacancy density on the CeO_2, facilitating vanillin conversion.[79] Ni-MMOFs exhibit significant potential in photocatalysis and removal of dyes due to their synergistic effects between Ni and other metal ions.[80,179] These effects diminish the energy band gap, which increases light harvesting and improves the regulation of energy barriers and Gibbs-free energy. Ni high affinity for π* orbitals, enabled by its d^8 electron configuration, makes it particularly effective for photocatalytic CO_2 reduction and hydrogen evolution. Ni-MMOFs excel in CO_2 photoreduction due to their ability to stabilize intermediates and to lower energy barriers when combined with other metals. In one report, $Ni_{0.75}Mg_{0.25}$-MOF-74 was found to achieve a yield of 0.64 mmol h^{-1} g_{MOF}^{-1} of $HCOO^-$ in pure CO_2, much higher than the yield of Ni-MOF-74 as a photocatalyst (0.29 mmol h^{-1} g_{MOF}^{-1}). Mg-MOF-74 was, on the other hand, inactive as a photocatalyst. It was proposed that the activity of $Ni_{0.75}Mg_{0.25}$-MOF-74 arises from the strong CO_2 affinity of Mg and the synergistic interaction between Mg^{2+} and Ni^{2+}, stabilizing the *OCOH intermediate, decreasing the energy barrier and enhancing efficiency.[46] In another example, NiZrCu-BDC, a two-dimensional trimetallic MOF, reduces CO_2 to methanol and ethanol with efficiencies of 41.05 μmol h^{-1} g^{-1} and 36.62 μmol h^{-1} g^{-1}, respectively. The ultrathin structure (4 nm) diminishes the distance required by charge carriers to reach the surface, while Zr and Cu promote CO_2 chemisorption and intermediate stabilization.[16] Ni-MMOFs are efficient materials to promote the HER. Their performance can be further optimized by regulating the free energy values of hydrogen adsorption (ΔG_{H*}), which is a suitable descriptor to predict the proton reduction efficiency. Incorporating additional metals, like Pt, can increase Ni intrinsic HER catalytic activity. In one

Table 2 Summary of the reported studies describing Ni-MMOFs or their derived composites and materials in diverse applications, indicating additional metals and their efficiency data[a]

Ni-MMOF	Other metals	Application	Efficiency	Ref.
$Er_{0.5}Ni$–BDC MOF	Er	Electrocatalyst/water splitting	C.d: OER: 100 and HER: 10/O.v: OER: 420 and HER: 270/T.f: OER: 99.0 and HER: 103	165
MIL-53(Ru–NiFe)	Ru/Fe	Electrocatalyst/water splitting	C.d: OER and HER: 50 Cell voltage: 50/O.v: OER: 210 and HER: 62/T.f: OER: 42.0 and HER: 49/C.v: 1.6	181
$Mn_{0.52}Fe_{0.71}Ni$-MOF-74	Mn/Fe	Electrocatalyst/water splitting	C.d: OER: 100 and HER: 10/O.v: OER: 267 and HER: 99/T.f: OER: 36.7 and HER: 103.8	60
Co–Ni–Al-MOFs[b]	Co/Al	Electrocatalyst/water splitting	C.d: OER and HER: 50/O.v: OER: 220 and HER: 174/T.f: OER: 97 and HER: 108	182
Pt–NiFeMOF[c]	Pt/Fe	Electrocatalyst/water splitting	C.d: OER and HER: 100 Cell voltage: 10/O.v: OER: 261 and HER: 125/T.f: OER: 40.43 and HER: 77.34/C.v: 1.45	183
FeCoMnNi-MOF-74	Fe/Co/Mn	Electrocatalyst/water splitting	C.d: OER: 50, HER: 10, and cell voltage: 10/O.v: OER: 250 and HER: 108/T.f: OER: 41.28 and HER: 72.89/C.v: 1.62	184
$Co_{0.2}Fe_{0.8}Ni$–OCNF	Fe/Co	Electrocatalyst/water splitting	C.d: OER, HER, and cell voltage: 10/O.v: OER: 291 and HER: 259/T.f: OER: 36.1 and HER: 94.2/C.v: 1.65	52
Ni-MOF-Fe-2	Fe	Electrocatalyst/OER	C.d: 10/O.v: 269/T.f: 47.1	185
$Ni_{0.5}Fe_{0.5}$-THQ	Fe	Electrocatalyst/OER	C.d: 10/O.v: 272/T.f: 47.9	168
$Fe_{0.5}$-BMM-10-700[d]	Fe	Electrocatalyst/OER	C.d: 50/O.v: 359/T.f: 79.2	186
NiFe-NDC$_{0.9}$BDC$_{0.1}$	Fe	Electrocatalyst/OER	C.d: 10/O.v: 295/T.f: 69.4	187
NiFe-MOF-BF4$^-$-0.3	Fe	Electrocatalyst/OER	C.d: 10/O.v: 237/T.f: 41	167
NiFc$'_{0.4}$Fc$_{1-0.6}$/NF[e]	Fe	Electrocatalyst/OER	C.d: 100/O.v: 213/T.f: 45	51
NiFe–GA	Fe	Electrocatalyst/OER	C.d: 100/O.v: 236/T.f: 28.74	172
$(Ni_2Co_1)_{0.925}Fe_{0.075}$-MOF[f]	Fe/Co	Electrocatalyst/OER	C.d: 10/O.v: 257/T.f: 41.3	188
NiCoFe–NDA/NF	Fe/Co	Electrocatalyst/OER	C.d: 10/O.v: 215/T.f: 64	169
FCN-BTC/NF	Fe/Co	Electrocatalyst/OER	C.d: 300/O.v: 268/T.f: 29.3	189
$NiCo_{1.09}BDC$-$Fc_{0.25}$/NF	Fe/Co	Electrocatalyst/OER	C.d: 50/O.v: 263/T.f: 41	190
FeCoNi-btz/NF	Fe/Co	Electrocatalyst/OER	C.d: 10/O.v: 263/T.f: 64	191
NiFe$_{0.2}$Co$_{0.3}$-ZIF[g]	Fe/Co	Electrocatalyst/OER	C.d: 100/O.v: 216/T.f: 23.25	166
NiFeZn MOF nanosheets[f]	Fe/Zn	Electrocatalyst/OER	C.d: 10/O.v: 233/T.f: 37.8	192
$Ni_1Fe_1Cr_{0.3}$-MOFs[f]	Fe/Cr	Electrocatalyst/OER	C.d: 10/O.v: 333/T.f: 66	193
$Ni_4Co_4Fe_2$-MOFs[f]	Fe/Co	Electrocatalyst/OER	C.d: 10/O.v: 243/T.f: 48.1	194
Ru@NiCo-MOF HPNs	Ru/Co	Electrocatalyst/OER	C.d: 10/O.v: 284/T.f: 78.8	195
$(Ni_3Co_1)_3Fe_1$-MOFNSs[f]	Fe/Co	Electrocatalyst/OER	C.d: 10/O.v: 245/T.f: 50.9	196
$FeCo_{0.5}Ni_{2.5}$-NBs	Fe/Co	Electrocatalyst/OER	C.d: 10/O.v: 273/T.f: 51.1	197
FeNiCo-1,3,5-BTC-MOF	Fe/Co	Electrocatalyst/OER	C.d: 10/O.v: 239/T.f: 42.4	198
Fc-NiCo-BDC	Fe/Co	Electrocatalyst/OER	C.d: 200/O.v: 273/T.f: 32	174
NiFe-25[h]	Fe	Electrocatalyst/OER	C.d: 10/O.v: 299/T.f: 48.7	199
t-NiCoFe-LDH	Fe/Co	Electrocatalyst/OER	C.d: 10/O.v: 277/T.f: 68.83	200
Ni-MOF-Fe-Se-400	Fe	Electrocatalyst/OER	C.d: 10/O.v: 242/T.f: 41.25	201
CoNi–Cu(BDC)	Co/Cu	Electrocatalyst/OER	C.d: 10/O.v: 327/T.f: 75.7	202
FeCoNiMnMOF/NF	Fe/Co/Mn	Electrocatalyst/OER	C.d: 50/O.v: 239/T.f: 62.05	50
HE-MOF	Fe/Co/Zn/Mo	Electrocatalyst/OER	C.d: 50/O.v: 254/T.f: 61	171
CoNiP-0.25[i]	Co	Electrocatalyst/HER	C.d: 20/O.v: 170/T.f: 52	203
NiMo/CuO@C	Cu/Mo	Electrocatalyst/HER	C.d: 10/O.v: 85/T.f: 290	204
NiRu$_{0.13}$-BDC	Ru	Electrocatalyst/HER	C.d: 10/O.v: 36/T.f: 32	173
In/Ni-MOF[p]	In	Electrocatalyst/HER	C.d: 10/O.v: 215/T.f: 131.11	205
NiFe-MIL-53-NH$_2$	Fe	Electrocatalyst/UOR	C.d: 50/O.p: 1.398/T.f: 14	206
TM-MOF-800	Co/Zn	Electrocatalyst/UOR	C.d: 10/O.p: 1.37/T.f: 137	207
Fc-NiCo-BDC	Fe/Co	Electrocatalyst/UOR	C.d: 10/O.p: 1.35/T.f: 41	174
NiFeMn-pma	Fe/Mn	Battery/LIBs	C.d: 100/capacity: 624/cycle: 100	208
Fe–Co–Ni NFSs	Fe/Co	Battery/LIBs	C.d: 1000/capacity: 489/cycle: 1000	209
Ni–MnO/PC	Mn	Battery/AZIBs	C.d: 3000/capacity: 347.4/cycle: 6000	210
Co/Ni-MOF[j]	Co	Supercapacitor	S.p: 2608/C.d: 1.0 (5000 cycle)/E.d: 47.3/ P.d: 780/retention: 88%	211
NiCoMOF-2[i]	Co	Supercapacitor	S.p: 108.5/C.d: 0.5 (6500 cycle)/E.d: 45.7/ P.d: 450.6/retention: 84.3%	70

Table 2 (*Contd.*)

Ni-MMOF	Other metals	Application	Efficiency	Ref.
2D CoNi(1 : 6)-MOF[k]	Co	Supercapacitor	S.p: 455/C.d: 0.5 (3000 cycle)/E.d: 38.8/ P.d: 263.3/retention: 73.9%	212
VNi-MOF NSAs/NF	V	Supercapacitor	S.p: 516.5/C.d: 1.0 (12 000 cycle)/E.d: 43/ P.d: 800/retention: 85.6%	213
Zn_1Ni_3-M[l]	Zn	Supercapacitor	S.p: 466.5/C.d: 0.5 (2500 cycle)/E.d: 9.55/ P.d: 3600/retention: 44%	214
NiMn–S[m]	Mn	Supercapacitor	S.p: 2510.15/C.d: 1.0 (5000 cycle)/E.d: 82.2/P.d: 800/retention: 84.5%	178
Ni–Co–$Mn_{0.25}$ MOF[k]	Co/Mn	Supercapacitor	S.p: 1575/C.d: 1.0 (5000 cycle)/E.d: 73.56/ P.d: 399/retention: 81.64%	215
NiCoMn-MOF[n]	Co/Mn	Supercapacitor	S.p: 1000/C.d: 4.0 (5000 cycle)/E.d: 55/P.d: 2467/retention: 97%	216
NiCoMn–HMT[n]	Co/Mn	Supercapacitor	S.p: 905/C.d: 3.0 (5000 cycle)/E.d: 78/P.d: 3500/retention: 96%	217
$[Ni(\mu_3\text{-pic})_2\text{-K}(\mu\text{-SCN})]_n$	K	Photocatalyst/dye degradation	94%/R^2: 0.964/reuse: 4 cycles	218
Fe–Ni–P[f]	Fe	Photocatalyst/water splitting	H_2 and O_2 production: 5420 and 900.3/ reuse: 4 cycles	80
FeNi-MOFs[f]	Fe	Photocatalyst/pollutant degradation	Fe^{2+} recovery with Fe^{3+}/Fe^{2+} cycling efficiency >58%	219
$Ni_{0.75}Mg_{0.25}$-MOF-74	Mg	Photocatalyst/CO_2 reduction	$HCOO^-$ yield: 0.64	46
HTHATN-Ni-Pt-NS	Pt	Photocatalyst/hydrogen evolution	Band gap: 1.11/hydrogen evolution rate: 47.2 mmol g^{-1} h^{-1}	82
NiZrCu-BDC	Zr/Cu	Photocatalyst/CO_2 reduction	Methanol: 41.05 μmol h^{-1} g^{-1}/ethanol: 36.62 μmol h^{-1} g^{-1}	16
3Ni–Ce/C[i]	Ce	Catalyst/hydrodeoxygenation of lignin derivatives vanillin	>95.0%/selectivity: 81.4%/reuse: 4 cycles	79
CuNi-MOFs[f]	Cu	Catalyst/reduction of 4-nitrophenol	Apparent rate constant: 0.153 s^{-1}/reuse: 5 cycles	220
Ni/Cu-MOFs[o]	Cu	Sensing/glucose biosensors	Detection limit: 0.51 μM/sensitivity: 26.05 μA cm^{-2} mM^{-1}	221
NiCo-HHTP	Co	Sensing/biosensor for miRNA-141	Detection limit: 0.69 fM	222
Ni/Co(HHTP)MOF	Co	Sensing/determination of glucose in serum and beverage	Detection limit: 100 nM/sensitivity: 3250 μA mM^{-1} cm^{-2}	223
NiCo-MOF	Co	Sensing/glucose biosensing	Detection limit: 0.29 μM/sensitivity: 0.6844 mA mM^{-1} cm^{-2}	224
NiCoFe-MOF	Fe/Co	Sensing/H_2O_2	Detection limit: 2.1 μM	225
Ni Fe-MOF	Fe	Removal/dye and antibiotic	Adsorption removal (Q_{max}): 395.9 mg g^{-1}/ removal of tetracycline: 568.1 mg g^{-1}	226
BUT-85	Ni	Separation/C_2H_2: CO_2	pH stability: 3 to 13	227

[a] C.d: current density given in A g^{-1} or mA cm^{-2} for energy applications; O.v: overpotential given in mV; T.f: Tafel slope given in mV dec^{-1}; C.v: cell voltage given in V; O.p: onset potential given in V; and S.p (specific capacitance) is given in F g^{-1}, C g^{-1}, and mAh g^{-1}; E.d: energy density given in Wh kg^{-1}; P.d: power density given in W kg^{-1}; for further details, see the references; bandgap given in eV; AQE/photocurrent density (pd) given in μA cm^{-2}; RT: room temperature; TOF; TON; E_a: energy activation given in kJ mol^{-1}; for further details, see the references. NS: nanosheets; LDH: layered double hydroxide; OCNF: derived oxygen carbon nanoflower; THQ: tetrahydroxy-1,4-benzoquinone hydrate; GA: gallic acid; HPNs: hollow porous nanospheres; NBs: nano-bundles; HE: high entropy; TM: trimetallic; pma: benzene-1,2,4,5-tetracarboxylic acid; NFSs: nano frame superstructures; HTHATN: S-terminated hexathiohexaazatrinaphthylene; HHTP: 2,3,6,7,10,11-hexahydroxytriphenylene; BUT: Beijing University of Technology; NSAs: nanosheet arrays. [b] BTC and bipyridine as linkers. [c] NiFe-BDC nanosheet agglomerates grown on nickel foam. [d] Linkers for BMM denoted as H_3TPO (tris-(4-carboxyphenyl) phosphine oxide) and dabco (1,4-diazabicyclo[2.2.2]-octane). [e] Composed of mixed ligands 1,1'-ferrocene dicarboxylic acid (Fc') and defective ferrocene carboxylic acid (Fc). [f] BDC as the organic ligand. [g] 2-Methylimidazole as the organic linker. [h] Derived from MOF-74. [i] BTC as the linker. [j] p-Phthalic acid. [k] BPDC: biphenyldicarboxylate as the linker. [l] Containing melamine (MA) and 2,5-thiophene dicarboxylic acid (TDA) as the ligand. [m] 2,5-Dihydroxybenzene-1,4-dicarboxylic acid (H_4DOBDC) as the linker. [n] HMT: hexamethylenetetramine as the linker. [o] Glutaraldehyde as the linker. [p] BDC and Trz (1,2,4-triazolate) as organic linkers.

illustrative example, a bimetallic 2D HTHATN-Ni-Pt-NS MOF (HTHATN: hexathiohexaazatrinaphthylene; NS: nanosheets) was used as a hydrogen evolution co-catalyst and quencher of the ruthenium(II) trisbipyridyl photosensitizer. Upon irradiation with visible light (λ > 420 nm) using the ruthenium(II) polypyridyl complex as a light harvesting photosensitizer and in the presence of N,N-dimethylaniline as a sacrificial electron donor, HTHATN-Ni-Pt-NS achieves a H_2 evolution rate of 47.2 mmol g^{-1} h^{-1}, significantly outperforming the mono-metallic counterpart and becoming among the most efficient HER materials in photocatalysis. Pt^{2+} ions create active metal centers and optimize the ΔG_{H*} value of Ni^{2+} sites, facilitating efficient proton reduction and H_2 desorption. The π-conjugated system of the MOF supports electron transfer, further enhancing activity.[82] Ni-MMOF-derived materials show exceptional photocatalytic efficiency for simultaneous overall H_2 and
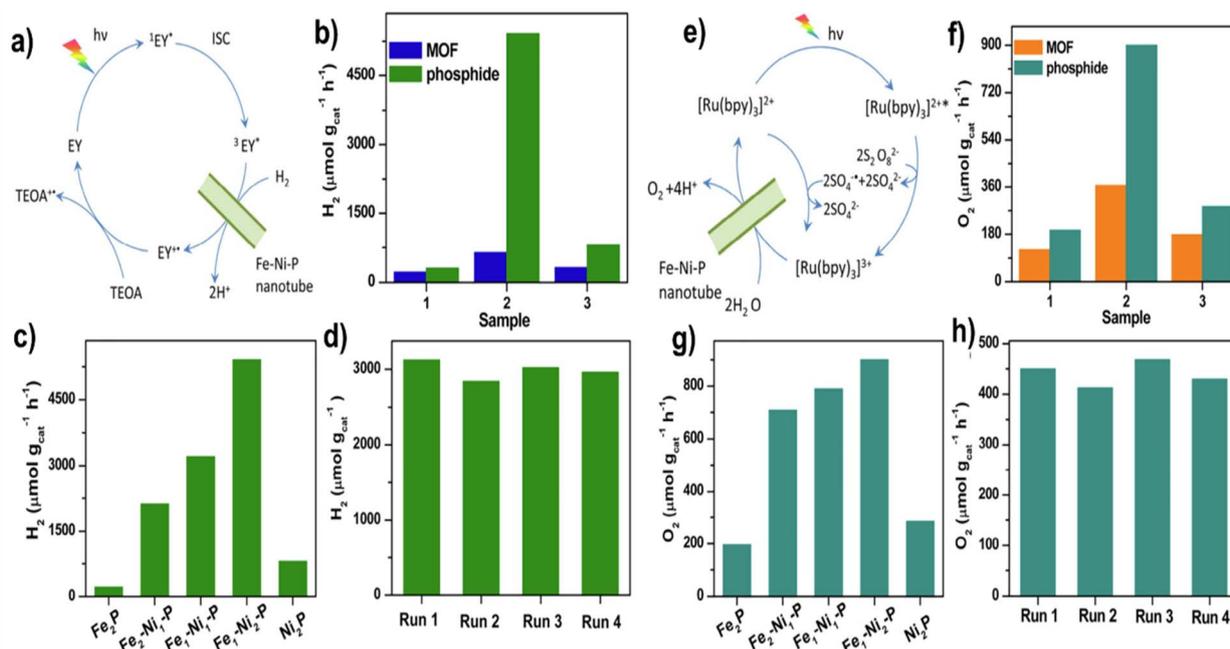
Fig. 13 (a) Proposed mechanism for the Eosin-Y photosensitized H_2 evolution promoted by MOF-derived bimetallic Fe−Ni−P; (b) H_2 production rates of Fe_2P (1), $Fe_1−Ni_2−P$ (2), and Ni_2P (3) and their MOF precursors, (c) H_2 production rates of diverse MOF derived phosphides; (d) stability of $Fe_1−Ni_2−P$ nanotubes in the Eosin-Y photosensitized H_2 evolution; (e) proposed mechanism for the O_2 evolution promoted by MOF derived Fe−Ni−P using $Ru(bpy)_3^{2+}$-photosensitization; (f) O_2 production rates of Fe_2P (1), $Fe_1−Ni_2−P$ (2), and Ni_2P (3) and their MOF precursors; (g) O_2 production rates of diverse MOF derived phosphides; (h) stability of $Fe_1−Ni_2−P$ nanotubes in the O_2 evolution rates using $Ru(bpy)_3^{2+}$-photosensitization. Reproduced with permission from ref. 80, copyright 2020 Elsevier.

O_2 production. As an example, $Fe_1−Ni_2−P$ phosphide nanotubes derived from Fe−Ni/MIL-88 by phosphatization with in situ generated PH_3 exhibit a H_2 production rate of 5420 μmol g^{-1} h^{-1} and an O_2 production rate of 900.3 μmol g^{-1} h^{-1}. The phosphatization process improves kinetics and enhances the photocatalytic activity compared to monometallic Fe_2P or Ni_2P[80] (Fig. 13). In another instance, derived-FeNi MOFs illustrate a degradation efficiency of 91% for rhodamine B (RhB) and 89% for Congo red, which is superior compared to conventionally prepared FeNi-MOFs. Based on DFT simulation, Ni and Fe form clusters that are arranged in proximity to each other and, through proper interaction, modulate the electronic and catalytic features of MOFs. Fe/Ni sites decrease the strength of dye molecule bonds and reinforce the degradation procedure; meanwhile, carboxyl groups in bimetallic MOFs can establish a hydrogen bond and stability.[180]

The incorporation of other metal ions creates synergistic effects, improving both performance and durability. Additionally, the mixed valence states of nickel (Ni^{2+}/Ni^{3+}) contribute to increased electron availability, further enhancing energy storage capabilities. For battery applications, Ni-MMOFs outperform Ni-MOFs due to the interaction of Ni possessing strong Lewis acid character with anions and other metals. These interactions enable effective electrolyte penetration and ion migration, such as Li^+ ions, through the MOF porous structure. The synergistic effects between Ni and other metals enhance the conductivity, stability, and overall performance of battery systems. Table 2 provides additional examples of Ni-MMOFs in

battery systems. For energy storage applications based on Ni-MMOFs, Ni sites via a synergistic effect with adjacent metals can generate more active sites by enhancing charge transport and altering the structure to achieve better performance of energy storage. Also, mixed valence $Ni^{2+/3+}$ alongside other metal ions can generate more electrons during storage applications and increase specific capacitance. Strong Lewis acid/base interactions between Ni and anions, modulated with other metals in Ni-MMOFs, can improve the performance of battery applications via a synergistic effect due to the effective penetration of the electrolyte and facile migration of ions through the micropores, particularly Li^+, which is highly relevant in batteries. In total, the activity of Ni metal in MMOFs illustrates as one of the most used metals in energy storage systems, which show their significance toward this application. Also, the synergistic effect between Co and Mn has attracted considerable interest from researchers. Ni and its synergistic effect with Co (Ni-CoMOFs) demonstrate higher performance due to rich redox activity and an augmentation in the specific capacitance. Also, Mn and its synergistic effect with Ni exhibit great energy storage performance due to the multi-valent nature of Mn. Besides batteries, Ni-MMOFs are also highly efficient materials for storing electrical energy in supercapacitors due to the high specific capacitance values that Ni-MMOFs can achieve and their durability over extended charge–discharge cycles. The combination of Ni with metals like Co and Mn enhances the redox activity of the resulting MMOF, accelerating Faraday redox reactions and providing additional active sites for

electrolyte interaction. In this way, materials exhibiting pseudo-capacitance that combine double-layer charge storage of supercapacitors with reversible redox processes characteristic of batteries can be obtained. Furthermore, Ni can lower the energy barrier of gas formation and evolution, and it has more affinity for π^* orbitals due to the large number of d orbital electrons (d^8), which is beneficial for reactions requiring CO_2 activation. Furthermore, their synergistic effect with Fe can also enhance the photocatalytic activity due to the increase in the number of attainable active sites and the regulation of the d-band energy center becoming closer to the Fermi level. However, as a general effect, the presence of Fe lowers the affinity of the Ni for CO_2 and increases the affinity of the Fe–Ni MMOF for H_2O due to the lower number of d orbital (d^6) electrons. Also, similar to the Fe-MMOF, the Ni-MMOF can be explored more in the future in terms of application and modulation of the content of Ni in the MMOF besides other metals to achieve their best performance. However, electrocatalytic procedures are well defined in this category, but their applications in photocatalytic, sensing, and catalytic organic transformations warrant further investigation in the future.

6. Cobalt-based MMOFs

Co-MMOFs and their relative derived materials are utilized in various applications, including sensing, electrocatalysis, catalysis, energy storage systems, and even photocatalysis.[228–235] The incorporation of a second metal into the structure of cobalt-based MOFs has been reported to enhance the performance of Co-MMOFs compared to monometallic Co-based MOFs. Enhanced efficiency can be attributed to the synergistic effect between the multiple metals present in MOFs.[236]

It has been demonstrated that the synthesis of bimetallic MOFs with a uniform distribution of metal centers can be achieved by placing two ions with similar radii in the MOF structure. The Co^{2+} ion has a similar radius to that of the Zn^{2+} ion, which allows for the uniform distribution of these two metals. Consequently, Co^{2+} and Zn^{2+} can be distributed uniformly within the bimetallic MOF system, thereby facilitating the synthesis of an appropriate CoZn-MMOF with enhanced performance.[237] For example, Jianbin Zheng and colleagues synthesized a dopamine electrochemical sensor. Dopamine is a neurotransmitter that plays a vital role in the human body. It is widely distributed throughout the cardiovascular system, the central nervous system, the kidneys, and the endocrine system. An elevated concentration of dopamine is indicative of pathological disorders such as Parkinson's disease and schizophrenia. For this reason, the quantification of this substance in body fluids is of great significance. In the 2D Co/Zn-TCPP material (TCPP: tetrakis(4-carboxyphenyl)porphyrin), the doping of cobalt and zinc metal ions is beneficial for electron exchange and transfer with dopamine. Consequently, the cooperative effect of Zn^{2+} and Co^{2+} active centers enhances the electrocatalytic activity of this MOF, thereby facilitating an excellent sensing capability for dopamine detection with a detection limit of 1.67 nM for a signal-to-noise ratio of 3 and the response being linear with the dopamine concentration in

the range from 5 nM to 177.8 μM.[228] Besides parent Co-MMOFs, Co-MMOF-derived materials are widely employed in electrochemical sensing, the removal of organic pollutants, medicine, and other areas. The transformation of the Co-MMOF can be accomplished by calcination under an inert atmosphere. The calcination of Co-MMOFs at low temperatures to carbonize the organic ligand results in the production of metal hybrids in the form of homobimetallic hollow nanocages (C-CoM-HNC; C: carbonization at 350 °C for 2 h; HNC: hollow nanocages). This procedure allows for the controlled alteration of the structure of Co-MMOF precursors, while simultaneously facilitating the formation of synergistic active sites with cobalt alloys, thereby enhancing the catalytic activity and subsequently improving the performance of the derived material. These materials are utilized in fields such as catalysis and electrocatalysis, including electrochemical sensing and pollutant removal. For instance, Yuming Huang et al. calcined a CoCu-MOF and employed this material as a multifunctional nanoenzyme for the degradation of organic pollutants, including RhB, and for a bioassay targeting acetylcholinesterase (AChE). Copper-doped C–CoCu–HNC nanostructures demonstrate enhanced performance with respect to other monometallic C–Co–HNCs as peroxymonosulfate (PMS) and oxidase activators. The incorporation of copper into the structure of this MOF results in a higher density of surface oxygen vacancies during the conversion of CoCu-MOF to C–CoCu–HNC, thereby enhancing its catalytic activity. The enhanced catalytic activity of C–CoCu–HNC is reflected in the production of higher quantities of $SO_4^{\cdot-}$ through the effective activation of PMS, thereby accelerating the decomposition of RhB dye. Moreover, this enhanced catalytic activity enables C–CoCu–HNC to exhibit potent sensitivity for the detection of AChE activity, with a detection limit of 0.1 mU L^{-1}. AChE is a primary cholinesterase in the body, and its activity is associated with neurodegenerative disorders such as Alzheimer's disease. Therefore, measuring its activity in real body fluids is important from an analytical standpoint. The C–CoCu–HNC, produced with its oxidation activity, may be considered a sensitive bioassay for screening AChE activity. After configuration optimization, the O_2 chemically binds with one of the terminal oxygens connecting to the surface of Co_3O_4. But in terms of $CuCo_2O_4$, both oxygen atoms connect to the Co and Cu on the surface. This tighter connection can enhance electron transport from the Co and Cu to the antibonding π^* orbital of O_2, lower the strength of the O–O bond in O_2 and lead to superior adsorption and electron-donating capability toward PMS.[238] In another instance, the bimetallic Co–Pr–BDC MOF exhibits performance in bio-sensing applications via response to altering creatinine concentrations, resulting in a detection limit of 0.12 mM. The synergistic effect between Co and Pr (praseodymium), which incorporates lanthanides such as Pr into the structure, can enable f–f transitions, boost the absorption in the visible spectrum, and with the possibility of forming hydrogen bonds, may account for the better performance of the bimetallic MOF.[239]

Also, Co-MMOFs are some of the most commonly used materials in electrocatalysis. In bimetallic Co/M MOFs, the presence of an additional metal can facilitate charge transfer,

Table 3 Summary of reported applications of Co-MMOFs or their derived materials with their efficiency[a]

Co-MMOF	Other metals	Applications	Efficiency	Ref.
OX-Co$_3$O$_4$–Ru	Ru	Electrocatalyst/water splitting	C.d: OER and HER: 100 Cell voltage: 500/O.v: OER: 286 and HER: 49/T.f: OER: 51.2 and HER: 63.3/C.v: 1.71	240
Co–V-FeNiLDHs	Ni/Fe/V	Electrocatalyst/water splitting	C.d: OER: 50 and HER: 10 Cell voltage: 10/O.v: OER: 244 and HER: 180/T.f: OER: 58 and HER: 121.5/C.v: 1.62	241
Ni/Co-DH	Ni	Electrocatalyst/OER	C.d: 10/O.v: 229/T.f: 86.6	257
NiCo(OH)$_x$@Co-MOF^b	Ni	Electrocatalyst/OER	C.d: 10/O.v: 210/T.f: 43	258
CoY-MOF/NF^c	Y	Electrocatalyst/OER	C.d: 10/O.v: 100/T.f: 68	61
Co/Fe (1 : 1)-MOF^d	Fe	Electrocatalyst/OER	C.d: 500/O.v: 490/T.f: 42	259
Co-MOF/Fe$_{10}^e$	Fe	Electrocatalyst/OER	C.d: 10/O.v: 260/T.f: 46.8	260
Co$_{0.6}$Fe$_{0.4}$-S-MOF	Fe	Electrocatalyst/OER	C.d: 10/O.v: 260/T.f: 56	236
CoFe(dobpdc)-III	Fe	Electrocatalyst/OER	C.d: 300/O.v: 240/T.f: 35.1	242
Co$_{0.8}$Fe$_{0.2}$-MOF^f	Fe	Electrocatalyst/OER	C.d: 10/O.v: 237/T.f: 36.3	261
Co$_{0.9}$Ce$_{0.1}$-BTC	Ce	Electrocatalyst/OER	C.d: 10/O.v: 308/T.f: 107	262
Co$_{15}$Ni$_1$-MOF-3,5-H$_2$pdc	Ni	Electrocatalyst/OER	C.d: 10/O.v: 384/T.f: 59	263
A$_{2.5}$B–CoNi MOFs^g	Ni	Electrocatalyst/OER	C.d: 10/O.v: 300/T.f: 45.27	264
WCoFe$_{0.3}$-CNF	Fe/W	Electrocatalyst/OER	C.d: 100/O.v: 258/T.f: 44.8	246
G-FeNi-Co-ZIF-L	Fe/Ni	Electrocatalyst/OER	C.d: 10/O.v: 248/T.f: 49.5	265
NF/Co$_3$O$_4$/CoFe$_2$O$_4$	Fe	Electrocatalyst/OER	C.d: 10/O.v: 215/T.f: 90	245
Co–CIF:FeNiMo	Fe/Ni/Mo	Electrocatalyst/OER	C.d: 100/O.v: 238/T.f: 34	266
MoCoFe@NC	Fe/Mo	Electrocatalyst/OER	C.d: 10/O.v: 285/T.f: 72	267
FeCo$_{0.6}$Ni$_{0.4}$–CAT	Fe/Ni	Electrocatalyst/OER	C.d: 10/O.v: 277/T.f: 44.7	229
Fe–Ni–CoOOH-TPA	Fe/Ni	Electrocatalyst/OER	C.d: 10/O.v: 236/T.f: 39	244
Co$_{2.36}$Fe$_{0.19}$Ni$_{0.45}$-btca	Fe/Ni	Electrocatalyst/OER	C.d: 10/O.v: 292/T.f: 72.6	268
CoNiFe-ZIF-MFs	Fe/Ni	Electrocatalyst/OER	C.d: 10/O.v: 273/T.f: 87	269
CuCoNi–OH	Ni/Cu	Electrocatalyst/OER	C.d: 10/O.v: 290/T.f: 57.8	270
CoNiMn-MOF^h	Ni/Mn	Electrocatalyst/OER	C.d: 20/O.v: 220/T.f: 66	271
Ir@Co-BPDC	Ir	Electrocatalyst/HER	C.d: 100/O.v: 57/T.f: 33.39	272
CoNi-MOF^h	Ni	Battery/ARZBs	C.d: 20/capacity: 344/cycle: 1500	64
TTFTB-MnCo-MOF	Mn	Battery/NMC 62	C.d: 100/capacity: 154.9/cycle: 200	73
Co–Mn–O/C-0.2	Mn	Battery/LIBs	C.d: 1000/capacity: 1088.5/cycle: 600	273
ZNC ZIF-67	Ni/Zn	Supercapacitor	S.p: 247/C.d: 0.1 (5000 cycle)/E.d: 27.94/P.d: 1300/retention: 99%	231
Cu$_2$CoSnS$_4$	Cu/Sn	Supercapacitor	S.p: 393.5/C.d: 0.7 (8000 cycle)/retention: 88.5%	274
Ni–Zn–Co–S-0.25^b	Ni/Zn	Supercapacitor	S.p: 1930.9/C.d: 1.0 (10 000 cycle)/E.d: 32.8/P.d: 864.8/retention: 92.2%	275
Zn$_{0.25}$Ni$_{0.75}$Co-LDH-BA$^-$	Ni/Zn	Supercapacitor	S.p: 275/C.d: 1.0 (10 000 cycle)/E.d: 51.8/P.d: 789/retention: 94.6%	248
ZnCo$_2$Ni-LDH	Ni/Zn	Supercapacitor	S.p: 348.2/C.d: 1.0 (10 000 cycle)/E.d: 54.4/P.d: 4439/retention: 86%	276
NiCoMn–S^b	Ni/Mn	Supercapacitor	S.p: 2098.2/C.d: 1.0 (6000 cycle)/E.d: 50/P.d: 850/retention: 73.6%	249
Cu(NiCo)$_2$S$_4$/Ni$_3$S$_4$	Ni/Cu	Supercapacitor	S.p: 1320/C.d: 1.0 (5000 cycle)/E.d: 40.8/P.d: 7859.2/retention: 85%	277
NiCoC/O–NiCoAl LDH	Ni/Al	Supercapacitor	S.p: 2400/C.d: 1.0 (5000 cycle)/E.d: 80/P.d: 750/retention: 82.3%	278
CoNiSe$_2$/FeNiCoSe$_2$ YSBs^b	Ni/Fe	Supercapacitor	S.p: 1091.2/C.d: 1.0 (5000 cycle)/E.d: 76.5/P.d: 2378.7/retention: 85%	279
NiCo-MOF-31	Ni	Supercapacitor	S.p: 1697.2/C.d: 1.0 (5000 cycle)/E.d: 26.56/P.d: 750/retention: 85%	280
NiCo-BDC@MIM	Ni	Supercapacitor	S.p: 2252/C.d: 1.0 (2000 cycle)/E.d: 40.2/P.d: 972/retention: 73.2%	281
Zn$_{0.1}$Co$_1$-MOF-D2-24	Zn	Catalyst/epoxidation of cycloalkenes	95.5%/90 °C/air/5 h/selectivity: 96.7%/reuse: 10 cycles	282
Co$_1$Cu$_1$–MOF/PSM	Cu	Catalyst/degrades tetracycline in water	98.17%/30 min/reuse: 4 cycles	283
CuCo@C	Cu	Catalyst/hydrogenation of levulinic acid	100%/220 °C/4 h/reuse: 5 cycles	284
La$_2$Co$_8$-MOF-BTC-H	La	Catalyst/epoxidation of cycloalkenes	96.2%/airflow/80 °C/5 h/selectivity: 98.7%/reuse: 5 cycles	285

Table 3 (*Contd.*)

Co-MMOF	Other metals	Applications	Efficiency	Ref.
Pd_2Co_8-ZIF	Pd	Catalyst/cycloaddition reaction of CO_2	E_a: 98.7/97.3%/12 h/TON: 5754/TOF: 479/ reuse: 3 cycles	286
$Pd_{0.3}Co_{0.7}(bim)_2$	Pd	Catalyst/cycloaddition reaction of CO_2	94.3%/80 °C/6 h/TOF: 2501/reuse: 3 cycles	255
NUC-31	Tb	Catalyst/cycloaddition reaction of CO_2	98.7%/*n*-Bu4NBr/75 °C/12 h/selectivity: 99%/TOF: 8.23/reuse: 5 cycles	230
$Cu_6Fe_{0.8}Co_{3.2}$@MIL-101	Fe/Cu	Catalyst/ammonia borane hydrolysis	E_a: 37.2/298 k/TOF: 23.2/reuse: 7 cycles	287
CoNi-MOF[i]	Ni	Sensing/deoxynivalenol (DON) and salbutamol (SAL)	Detection limits: 0.05 and 0.30 pg mL^{-1} toward DON and SAL	288
Cu–Co-ZIF	Cu	Sensing/glucose	High sensitivity: 18.68 mA mM^{-1} cm^{-2}/ response time: 1.5 s/detection limit: 2 μM	289
CoZn-MOF	Zn	Sensing/dopamine	Detection limit: 0.67 μM	290
MnCo-MOF-74	Mn	Sensing/glucose	Sensitivity: 233.8 μA mM^{-1} cm^{-2}/ detection limit: (S/N: 3): 1.31 μM	291

[a] C.d: current density based on A g^{-1}, mA g^{-1} or mA cm^{-2} for energy applications/O.v: overpotential based on mV/T.f: Tafel slope based on mV dec^{-1}/C.v: cell voltage based on V/O.p: onset potential based on V and S.p (specific capacitance) is based on F g^{-1}, C g^{-1}, and mAh g^{-1}/E.d: energy density based on Wh kg^{-1}/P.d: power density based on W kg^{-1}/all percentages in the photocatalyst or catalyst represent the yield, conversion or any efficiency of MMOFs; for further details, see the references/bandgap based on eV/apparent quantum efficiency (AQE)/ photocurrent density (pd) based on μA cm^{-2}/RT: room temperature/TOF: turnover frequency/TON: turnover number/E_a: energy activation based on kJ mol^{-1}/for further details, see the references. LDH: layered double hydroxide; NC: N-doped carbon; dobpdc: 4,4′-dihydroxybiphenyl-3,3′-dicarboxylate; H_2pdc: pyridine-2,4-dicarboxylic acid; CNF: carbon nanoflakes; TPA: terephthalic acid; btca: benzotriazole-5-carboxylate; BPDC: biphenyldicarboxylate; YSBs: yolk–shell nano boxes; TTFTB: tetrabenzoate TTF (tetrathiafulvalene). [b] MIM: 2-methylimidazole as the organic ligand. [c] Mixed ligands of triethylenediamine (TED) and 1,4-benzenedicarboxylic acid (BDC). [d] 4,40-Oxydibenzoic acid as the linker. [e] BDC as the organic ligand. [f] dobpdc as the linker. [g] Terephthalic acid (A) and 2,5-dihydroxyterephthalic acid (B). [h] BTC as the linker. [i] Mixed organic ligands of 4-(1*H*-tetrazol-5-yl)benzoic acid (H_2TZB) and 2,4,6-tri(4-pyridyl)-1,3,5-triazine (TPT).

augment interaction between the MOF and electrolyte, tune the redox properties of the active sites, regulate the amorphous and crystalline MOF structure, optimize the electronic structure, and increase the intrinsic activity of Co MOFs as electrocatalysts. In one example, a bimetallic Ru-doped Co-oxalate MOF was transformed at 300 °C for 2 h in a muffle to achieve OX-Co_3O_4–Ru that exhibits excellent electrocatalytic activity for the HER and OER due to the increase in oxygen vacancies and higher surface hydrophobicity.[240] The performance of OX-Co_3O_4–Ru is summarized in Table 3. In another example, multimetallic Co-based MOF-derived material used in electrochemical water splitting is tetra-metallic Co–V–FeNi LDHs obtained by using ZIF-67 as a source of Co that, in combination with vanadyl acetylacetonate and Ni and Fe salts, form a FeNi-LDH doped with Co and V. The role of ZIF-67 is key to controlling the three-dimensional morphology of the resulting LDH. This tetrametallic Co–V–FeNi LDHs operate at a cell voltage of 1.62 V at a current density of 10 mA cm^{-2}, which is a lower voltage than those of other counterparts. This enhanced performance has been attributed to the morphology inherited from ZIF-67 with accessible sites, the presence of Co, which is a more active site, the electronic interaction between V and Co, and synergistic effects with the other metal ions, all contributing to the augmentation of intrinsic electrocatalytic activity and a larger surface area.[241] In one of the examples, the OER activity was reported using bimetallic Co-based MOFs, CoFe(-dobpdc) (dobpdc: 4,4′-dihydroxybiphenyl-3,3′-dicarboxylate) nanorods grown on NF. As commented earlier, electrocatalysts grown on NF generally result in better electrocatalytic performance due to the lower internal electrical resistance between

the electrocatalyst and the NF because of the better interfacial contact between them. Thus, the optimal CoFe(dobpdc) shows better electrocatalytic activity compared to another type of synthesized nanorods in both 0.1 M and 1.0 M KOH electrolyte due to (i) the appropriate morphology and long aspect ratio improves positively the electrocatalytic activity, Co contributing to the MOF thickening, therefore, adjusting growth and orientation, (ii) the solvent used in the MOF synthesis also influences OER activity that requires high wettability of the porous materials to augment affinity of MOF for NF and optimize nanorod growth, and (iii) analogously to other electrocatalytic processes, also in OER exposure of a high density of active sites and synergistic effect between metal ions improves the electrocatalytic response.[242] In another example, a 2D Co-based MOF formed from ultrathin nanosheets was prepared and submitted to post-synthetic Fe doping to obtain mixed valent $(Fe(\text{II})_1$-$Fe(\text{III})_1)_{0.6}$/NMOF-Co (NMOF: MOF nanosheets). This $(Fe(\text{II})_1$-$Fe(\text{III})_1)_{0.6}$/NMOF-Co was found to exhibit superior OER activity compared to its bulk counterparts and commercial RuO_2, with a lower Tafel slope of 50 mV dec^{-1} in alkaline media. The excellent performance of this MOF was found to derive from the fast charge transport, higher density of exposed active sites, and synergistic effect between mixed valence Fe and Co-based ultrathin nanosheet MOFs.[243] In another case of CoFe MMOFs, a 2D Co/Fe MOF containing tetrapyridyl linkers coordinated in equatorial positions around the metal ions to form the structure and two sulfocyanide groups coordinated in apical positions with the optimal Co/Fe ratio of $Co_{0.6}Fe_{0.4}$-MOF exhibited superior activity compared to its Co-MOF, Fe-MOF, Co-Ce-MOF, Co/Mn-MOF, and Co/Ni-MOF counterparts, thus

illustrating the potential of MMOFs to tune the electrocatalytic activity. However, the C_{dl} of Co/Fe-MOF is lower than that of Co/Ce-MOF. Based on XPS data, the larger C_{dl} of Co/Ce-MOF was attributed to the weak coordination of Ce ions, which causes more structural defects and, therefore, a larger ECSA. However, despite the larger C_{dl}, Co/Ce-MOF has a small number of active sites, which is detrimental to the OER activity. The higher Fe/Co-MOF activity is due to the influence of doping Fe on the redox properties of Co–S–Co that makes it easier to reach the Co^{3+} valence state and increases the density of active sites. Also, sulfur in this structure plays a positive role in enhancing OER activity.[236] In one case of trimetallic Co MMOFs, 2D Fe–Ni–CoOOH-TPA (TPA denoted as terephthalic acid) with ligand defects exhibited lower R_{ct} and higher C_{dl} for OER activity. The material consisted of a heterojunction of polycrystalline metal (oxy)hydroxide (MOOH) and amorphous metal oxides/hydroxides coordinated with TPA. It was prepared using ZIF-67 as a source of Co^{2+} ions that were etched with TPA to form a novel Fe–Ni–CoOOH-TPA composite. In this heterojunction, the valence band potential of Fe–Ni–CoOOH-TPA is 0.2 eV, which is lower than that of other counterparts, indicating that the installation of functional 1,4-BDC shifts the valence band of Fe–Ni–CoOOH-TPA closer to the Fermi level (E_F). As the band gap decreases, the conductivity increases by reducing the electron transition barrier from the valence to the conduction band. Also, the hydrophilicity of Fe–Ni–CoOOH-TPA can enhance electrolyte penetration into the electrocatalyst micropores, resulting in an increased active surface area and accelerated reaction kinetics, besides the positive impact of structural defects in increasing the density of undercoordinated metal positions.[244] Co MMOFs have also been used to obtain derived materials to be used as OER electrocatalysts. In one of the examples, bimetallic $Co_3O_4/CoFe_2O_4$ decorated on NF was derived from a mixed metal Co/Fe MOF using nicotinic acid as a linker grown on NF, followed by calcination at 500 °C. The resulting material exhibits an overpotential of 215 mV, and this good performance was attributed to: (i) the presence of Fe^{3+} in octahedral sites of $CoFe_2O_4$ acting as active sites and decreasing overpotential of the bimetallic derived MOF, (ii) the presence of octahedrally coordinated Co^{3+} sites in Co_3O_4 that boost conductivity and adsorption–desorption of oxygen intermediates, and (iii) integration and synergistic effect between Co_3O_4 and $CoFe_2O_4$ to boost OER.[245] Another example of multimetallic derived Co-based MOFs as electrocatalysts for the OER is trimetallic $WCoFe_{0.3}$-CNF (CNF: carbon nanoflakes) derived from a multimetallic hybrid zeolitic imidazolate framework using Co^{2+}, Fe^{2+}, and WO_4^{2-} ions as metal salts. When the feed Fe/Co ratio is 0.3, the molar ratio of Co^{3+}/Co^{2+} reaches 1.38, which is the highest molar ratio among the samples in the series, resulting in the best OER activity as shown in Table 3. It has been proposed that each metal has a specific prevalent role, with Co playing the role of the active site, Fe improving conductivity, and W acting as an electron density donor to optimize the electronic structure of Fe and Co.[246] CoY-MOF grown on NF has been reported to be an electrocatalyst for HER-GOR, which exhibits major electrocatalytic activity with a low cell voltage of 1.36 V. Co acts as the active center and Y regulates its electronic structure with a synergic effect between them, with the high surface area of the MOF leading to improved HER and GOR activity by exposure of a large density of active sites. A low overpotential of 100 mV at a current density of 10 mA cm^{-2} with a Tafel slope of 68 mV dec^{-1} was reported for the HER. Also, the Tafel slope for the GOR was only 98 mV dec^{-1}, indicating faster kinetics than the OER, for which the Tafel slope on the CoY-MOF/NF electrode was 123 mV dec^{-1}.[61] Regarding the ORR and zinc–air batteries, trimetallic MOF-derived MnCoNi–C–D exhibits a half-wave potential of 0.82 V for the ORR. Moreover, zinc–air batteries reached good power density, specific capacity, and higher open-circuit potential (OCV) in 1.46 V, which indicates better electrochemical performance for this MOF-derived material due to the generation of $MnCo_2O_4$ and NiO, while the hollow structure facilitates electron transfer and provides a large density of accessible active centers for ORR/OER catalysis.[247] Furthermore, the presence of an additional metal can also increase the yield and faradaic efficiency of Co in the NRR, providing sites for the adsorption and dissociation of N_2 molecules. In the case of the NRR, the bimetallic MOF-derived Co-based material Zn–Co_3O_4 exhibits an ammonia yield of 22.71 μg h^{-1} mg$_{cat}$$^{-1}$. The high electrochemical activity is achieved through a combination of oxygen vacancies, which act as Lewis acid centers, cobalt, which acts as an electron-rich center to enhance the adsorption and dissociation of nitrogen molecules, and zinc dopant sites, which facilitate electron transport. Based on XPS analysis, electron transfer from zinc to cobalt was observed, thus increasing the electron density of Co^{2+}. Hence, for an adequate charge balance in the mixed oxide, some oxygen atoms should exit from the structure and produce oxygen vacancies. Optimization of these parameters leads to the highest NRR activity.[68] For more details on Co-MMOFs, see Table 3.

Co-MMOFs are some of the most widely used materials for energy storage. The synergistic effect between Co and other metals can result in higher activity and stability of the material as an electrocatalyst in reactions and as a supercapacitor active material, which indicates the positive impact of using mixed valence $Co^{2+/3+}$. Also, materials derived from Co-MMOFs are among the materials with the highest energy storage performance. For instance, $Zn_{0.25}Ni_{0.75}$Co-LDH-BA$^-$/AA$^-$ (BA$^-$ = benzoate anion and AA$^-$ = acetate anion) shows a specific capacity of 275 mAh g^{-1} at a current density of 1 A g^{-1}, making the resulting assembled supercapacitor device of this MOF-derived material interesting for energy storage applications. The high specific charge storage performance of this MOF-derived material is the result of (i) the unique LDH morphology, which facilitates penetration of electrolyte into the material and a large specific surface area that leads to premier electrochemical proficiency and (ii) the synergistic effect between the three metal ions and the optimization of the Zn/Ni ratio since Co and Ni ions accelerate redox reactions and lead to the regulation of specific capacity, while the Zn ions enhance the electrical conductivity.[248] In another example of a Co MMOF-derived material employed as an active component in supercapacitors, NiCoMn–S was found to have superior storage efficiency compared to NiCoMn–OH, Co–S, NiCo–S, CoMn–S,
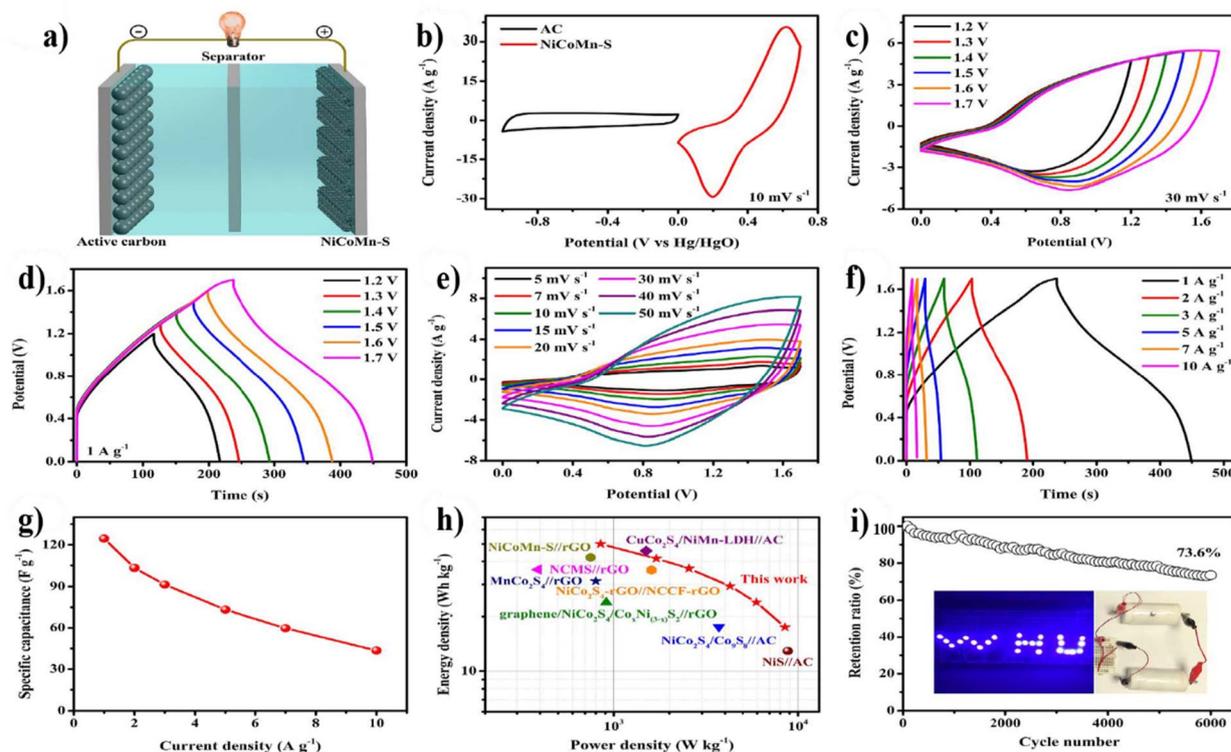
Fig. 14 (a) Illustration of the assembled NiCoMn–S//AC device; (b) CV curves of NiCoMn–S and AC at 10 mV s^{-1}; (c) CV curves at a scan rate of 30 mV s^{-1} in different potential windows for the assembled device; (d) GCD curves at a current density of 1 A g^{-1} in different potential windows for the assembled device; (e) CV curves at different scan rates; (f) GCD curves at different current densities for the assembled device; (g) specific capacitance at different current densities for the assembled device; (h) Ragone plots (energy density *vs.* power density) of NiCoMn–S//AC and other assembled devices; (i) cycling stability of the assembled device at 10 A g^{-1}. Reproduced with permission from ref. 249, copyright 2022 Elsevier.

Ni$_1$CoMn$_3$–S, and Ni$_3$CoMn$_1$–S, thereby showing that optimized trimetallic derived NiCoMn–S has better performance compared to its mono-metallic, bi-metallic, and trimetallic analogues with other ratios of the three metals. Thus, optimized trimetallic MMOF-derived NiCoMn–S exhibits a specific capacitance of 2098.2 F g^{-1} at a current density of 1 A g^{-1}, an energy density of 50 Wh kg^{-1}, and a power density of 850 W kg^{-1}, and maintains 73.6% for 6000 cycles, exhibiting notable capacitance retention. As shown in Fig. 14, the potential window of the assembled device made of NiCoMn–S//AC is 0–1.7 V. This high activity was attributed to (i) the appropriate electronegativity of sulfur being lower than that of oxygen implying that sulfide structures are more porous and flexible than their oxide counterparts, facilitating electron transport, (ii) the smaller band gap of sulfides than that of oxides which increases charge storage efficiency and is responsible for more efficient promotion of redox reactions, (iii) the larger BET area and higher porosity that lead to more exposed electroactive sites and facilitate electron or ion transport, emphasizing the importance of NiCoMn–S having a higher surface area than CoS, α-NiS, CoS$_2$, NiMn sulfide, NiCo$_2$S$_4$, NiCo$_2$S$_4$–Co$_9$S$_8$, Ni$_x$Co$_{3-x}$S$_4$, Cu(NiCo)$_2$S$_4$–Ni$_3$S$_4$ counterparts, and (iv) the existence of mixed-valence Ni^{2+}/Ni^{3+}, Co^{2+}/Co^{3+} in the material as revealed by XPS, which with their synergistic effect with Mn^{2+} provide a higher density of electro-active sites for redox reactions and boost energy storage

applications.[249] Furthermore, incorporation of Co into Mn-MOF also affords new energy storage devices.[73] However, based on the properties with a wide range of possible electronic configurations for Mn, it appears reasonable that MMOFs that contain Mn should also have considerable potential in those fields.[73] In one example of Mn-MMOFs, TTFTB-MnCo-MOF (TTFTB = tetrabenzoate tetrathiafulvalene), galvanostatic charge–discharge (GCD) performed in the range from 0.1 V to 3.0 V *versus* Li$^+$/Li exhibits an initial Coulombic efficiency of up to 57.1%. The full lithium-ion battery cell with a configuration of TTFTB-MnCo-MOF‖NMC 622 (NMC 622 corresponds to lithium nickel manganese cobalt oxide, with the numbers indicating the percentages of Ni, Mn and Co in LiNi$_6$Mn$_2$Co$_2$O$_2$ used as the cathode material) reaches a capacity of 154.9 mAh g^{-1} at 100 mA g^{-1} in the 200th cycle. Also, the TTFTB-MnCo-MOF‖AC (AC: active carbon) hybrid lithium-ion capacitor can achieve a specific energy of 141.4 Wh kg^{-1} at a specific power of 0.25 kW kg^{-1}. The high energy storage efficiency of this battery–supercapacitor hybrid device containing the TFF moiety in the MOF structure was attributed to several synergistic factors including the high porosity of the MOF, the presence of the sulfur-rich TTF ligand, and the bimetallic Mn^{2+} and Co^{2+} metal nature of the site. XPS analysis provides evidence that the S atoms of the TTF group are the sites associated with Li$^+$ storage. Besides the S-rich TTF ligand, Mn^{2+} is responsible for good cycling

performance and Co^{2+} increases the specific capacity.[73] Furthermore, incorporation of Cu into MOFs as one of the most widely employed elements in MMOFs illustrates their capability in medicine and energy storage as well as their use as a corrosion inhibitor and photocatalyst in their mixed-metal forms.[250–253] In the case of energy storage, a trimetallic NiCoCu-TPA MOF showed a specific capacity of 417C g^{-1} at 0.5 A g^{-1}. Also, NiCoCu-TPA//AC attains an energy density of 49.05 Wh kg^{-1} at 0.5 A g^{-1} and a power density of 6400 W kg^{-1} at 8 A g^{-1}, and exhibits cycling stability. This performance can be attributed to the incorporation and synergistic effects among Ni, Co, and Cu, where Ni induces redox activity, while Co can not only induce redox activity but also improve structural stability, and eventually Cu incorporation can provide more faradaic redox sites and enhance the conductivity within the architecture.[254]

Co-MMOFs exhibit a wide range of catalyst applications, due to the synergistic effect frequently found for Co combined with other metal ions. Co can easily activate O_2 molecules and promote catalytic aerobic oxidation reactions and this catalytic activity can be enhanced by combination with other metals. Particularly, Co alongside heavy metals forms MOF structures with a larger density of unsaturated coordination positions that can activate substrates and exhibit high TOF values, indicating better catalytic activity. One of the recent studies investigated the catalytic activity of bimetallic $Pd_{0.3}Co_{0.7}(bim)_2$ (PdCo-ZIF) with a range of Pd/Co ratios toward CO_2 cycloaddition. It was found that the presence of Pd generates defects at the Co sites in the structure, reaching a TOF of 2501 h^{-1} which is superior to those of its monometallic counterparts (Co-ZIF and Pd-ZIF). It was found that Pd-ZIF has no activity for this reaction, implying that undercoordinated cobalt ions at defects are the active centers in the material. The role of Pd was proposed to be the generation of a porous material with a high concentration of defective Co distorted sites acting as Lewis acids.[255] Regarding Ir incorporation with Co, such materials have attracted interest in photocatalyst applications, due to the use of Ir polypyridyl complexes in photo/electroluminescent devices and in photoredox synthesis.[256] One of the examples is based on UiO-67, containing some 2,2′-bipyridyl-4,4′-dicarboxylic acid ligands able to complex Ir at framework satellite positions. Besides the linker, other coordination positions around Ir were completed by either 2-phenylpyridine (ppy) or coumarin 6 (Cou6), of which the Ir complex with the UiO-67 framework and two Cou6
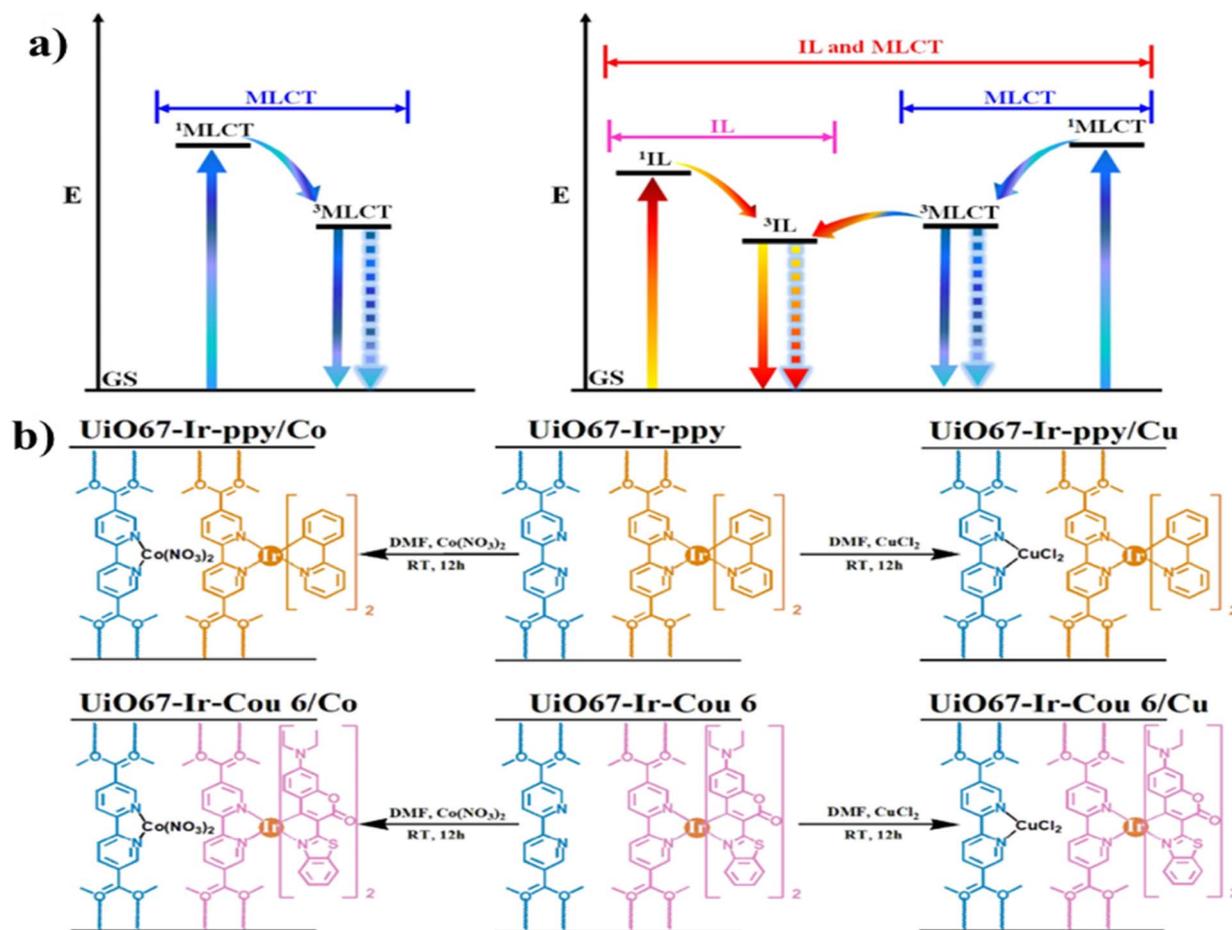

Fig. 15 (a) Diagram of the various energy levels available for Ir UiO-67 depending on the coordination environment around Ir ions; (b) illustration of the structure and post-synthetic modification of UiO67-Ir to form UiO-67-Ir-ppy or UiO67-Ir-Cou6 and the subsequent incorporation of Co(II) and Cu(II) ions. Reproduced with permission from ref. 256, copyright 2022 Wiley.

molecules was the best performing.[256] Subsequent incorporation of either Co or Cu in the series of UiO67-Ir (ppy or Cou6) is illustrated in Fig. 15. Ir complexes attached to the MMOF lattice act as strong visible-light-absorbing chromophores, particularly when containing Cou 6 as a ligand. The presence of Cou6 alters the lowest unoccupied excited state of the system from the ^{3}MLCT to the ^{3}IL state (IL meaning internal ligand), which is much longer lived and more suited for photocatalytic reactions. In this way, when Co is also attached to free 2,2′-bipyriduyl units, the UiO67-Ir-Cou6/Co system reaches an H_2 production yield of 2440.4 μmol g^{-1} h^{-1}, over 100-fold higher than that of UiO67-Ir-ppy/Co (22.3 μmol g^{-1} h^{-1}) with a 3MLCT excited state. Co-incorporation of Cu centers, rather than Co, is very appropriate for photocatalytic CO_2 reduction, forming HCOOH in a remarkable yield of 480.7 μmol g^{-1} h^{-1}. Therefore, it was concluded that the elaborated UiO67-Ir-Cou6/M, containing Zr, Ir, and either Co or Cu, has remarkable photocatalytic efficiency due to the properties of the ^{3}IL-type excited state of long lifetime as well as a strong visible light harvesting ability, thus favoring photoreduction.[256]

In the OER, the use of an additional metal adjacent to Co can produce coordinatively unsaturated sites to facilitate nucleophilic attack of OH$^-$, making more feasible the formation of reaction intermediates, such as $Co(OH)_2$ and CoOOH, which result in an enhancement of C_{dl} and the reaction kinetics. Also, the presence of an additional metal can favor the mixed valence of Co^{3+}/Co^{2+} with the formation of Co^{3+}, which has a higher oxidation potential than Co^{2+}, facilitating better OER performance. In summary, Co, compared to other transition metals, is one of the most commonly used metals in reports dealing with MMOFs in catalytic applications. In one of the most studied combinations, Co and Zn in MMOFs and derived materials exhibit a synergistic effect and complementary activity, with Co activating O_2 and Zn being particularly efficient for H_2 activation. This complementarity, together with the tuning of the electron density due to the differences in electronegativity, can be very beneficial for aerobic oxidation. Besides Zn, the combination of Co and heavy metals is beneficial for catalytic activity due to the generation of unsaturated coordination Co ions. Furthermore, the simultaneous incorporation of heavy metals and Zn results in stable, highly porous MMOFs. It seems that Zn induces porosity, while heavy metals increase structural stability. Also, their different affinity compared to Co and Zn is a powerful tool for further tuning of the electronic density of the active sites. In comparison to other applications, Co-MMOFs have been less studied as photocatalysts. However, it can be implied that crystal engineering regulating Co-MMOF structures should also be beneficial for their photocatalytic activity, as reported also in other sections. Although Fe and Ni-MMOFs are suggested to be focused more in the future, but synergistic effect between Co and Zn can be focused more on diverse applications such as energy storage. However, synergistic impact between Fe, Ni, and Co are growing trend in electrocatalysis with engineering in the content of mentioned metals and altering the linker of MOFs to see what kind of enhancing can occur in their performance compared to the bimetallic and monometallic counterparts, but in some experimental cases

this idea might not be properly work due to the structural issues or change in their performance with outstanding results.

7. Zirconium-based MMOFs

Zr-MMOFs have been less investigated for energy storage and conversion systems due to their lower conductivity or when doping with other Zr MOFs. However, Zr-MMOFs have unique structures and considerable stability, which can be beneficial for some energy applications. Thus, the addition of electroactive metals to Zr-MOFs can mitigate this low electrical conductivity, reaching a good stability/conductivity balance that makes Zr-MMOFs worth exploring in diverse energy applications. In one example, a multi-metallic Zr-based MOF 10Fe:90Ni@Zr-BTB (BTB: 1,3,5-tris(4-carboxyphenyl)benzene) was studied as an OER electrocatalyst exhibiting a high efficiency as indicated in Table 4. Initially, a Zr-based MOF was chosen for this application due to its unique morphology, but large concentrations of Ni and Fe are required to promote OER activity. Also, Ni@Zr-BTB exhibits a high overpotential of 647 mV, showing that the introduction of Fe into the MOF structure is necessary to regulate the activity of Ni oxyhydroxide and enhance OER catalytic activity.[292] Also in terms of medicine, these types of materials are less explored. In this case, there are examples of using Zr-MMOFs in medicine, such as Zr–Cu MOF@ES@aH, which illustrates efficiency toward human epidermal growth factor receptor 2-positive (HER^{2+}) breast cancer.[250] The role of Cu can be attributed to the conversion of Cu^{2+} to Cu^+, which produces ˙OH to hamper redox homeostasis and Cu^+ binding to lipoylated tricarboxylic acid (TCA) cycle proteins, destabilizing iron–sulfur clusters that lead to mitochondrial proteotoxicity.[250]

Due to the high valence of Zr^{4+}, this element can introduce ultra-high structural stability, while modifying the acidity of Lewis centers, resulting in high catalytic activity of other metal ions present in the composition of the MOF.[293–295] Also, in the case of high entropy MOFs, they can reduce the energy barrier and help the hydrogenation process.[296] Thus, a bimetallic Zr-based MOF was prepared starting from $Zr_6(\mu_3-O)_4(\mu_3-OH)_4$ (MOF-808, BTC as ligand) with $ZnEt_2$ to form MOF-808-Zn. This bimetallic ZrZn-MOF was used as a catalyst for selective CO_2 hydrogenation to methanol. The MOF catalyst was stable for at least 100 h at 250 °C. This stability is remarkable considering the relatively high temperature and H_2O is also formed as reaction products.[297] It was found that the notable catalytic activity of the bimetallic MOF was due to the formation of Zn^{2+}–O–Zr^{4+} centers in the post-treatment of MOF-808, as confirmed by XAS analyses. H_2 activated by Zn^{2+} centers and open Zn^{2+}–O–Zr^{4+} sites result in CO_2 adsorption, activation, and conversion to methanol. The mechanism was addressed by DFT calculations that indicate that H_2 should be able to easily produce Zn^{2+}–H$^-$ and Zr^{4+}–O–H$^+$ through heterolytic H–H splitting at the Zr^{4+}–O–Zn^{2+} center with a low energy barrier of 17.1 kcal mol^{-1}. Then, in the second step, H_2 can also be dissociated by the zinc(II) ion site and another Zr^{4+}–OH group, triggering the production of the HCOO* intermediate with an activation energy of 11.2 kcal mol^{-1}, even lower than the first step.[298] In another instance, a bimetallic Ce Zr-MMOF with a UiO-66 structure and

Table 4 Represent reported Zr-MMOFs or derived materials in diverse applications, with their efficiency in specific applications[a]

Zr-MMOF	Other metals	Applications	Efficiency	Ref.
10Fe:90Ni@Zr-BTB[b]	Ni/Fe	Electrocatalyst/OER	C.d: 10/O.v: 380/T.f: 72	292
MIL-173(Zr/Ti)-40	Ti	Photocatalyst/water splitting	381 and 145 μmol g^{-1} for H$_2$ and O$_2$ production/35 °C/22 h/reuse: 3 cycles	299
ZrCeTi-UiO-66-NH$_2$	Ti/Ce	Photocatalyst/dye degradation	38%	304
UiO-66 (Zr/Ti)	Ti	Catalyst/PET polycondensation	E_a: 22.37	47
UiO66-NH$_2$ (Zr/Ce)	Ce	Catalyst/synthesis of propylene carbonate	94%/5% Ce/nBu$_4$NBr/100 °C/4 h/selectivity: 98%/reuse: 5 cycle	293
Zr-CPB-Cu	Cu	Catalyst/carboxylation of styrene	97%/TBHP/nBu$_4$NBr/80 °C/12 h/selectivity: 95%/reuse: 6 cycles	305
MOF-808-Zn	Zn	Catalyst/CO$_2$ hydrogenation	190.7 mg$_{MeOH}$ g$_{Zn}^{-1}$ h^{-1}/250 °C/selectivity: 99%	298
Ni–Ce–Zr MOF[c]	Ni/Ce	Catalyst/reduction of MB	99.77%/reuse: 4 cycles	306

[a] C.d: current density based on A g^{-1} or mA cm^{-2} for energy applications/O.v: overpotential based on mV/T.f: Tafel slope based on mV dec^{-1}/C.v: cell voltage based on V/O.p: onset potential based on V and S.p (specific capacitance) is based on F g^{-1}, C g^{-1}, and mAh g^{-1}/E.d: energy density based on Wh kg^{-1}/P.d: power density based on W kg^{-1}/all percentages in the photocatalyst or catalyst represent the yield, conversion or any efficiency of MMOFs; for further details, see the references/bandgap based on eV/apparent quantum efficiency (AQE)/photocurrent density (pd) based on μA cm^{-2}/RT: room temperature/TOF: turnover frequency/TON: turnover number/E_a: energy activation based on kJ mol^{-1}/for further details, see the references. CPB: 1,2,3,4,5,6-hexakis(4-carboxyphenyl)-benzene. [b] BTB: 1,3,5-tris(4-carboxylatephenyl)benzene. [c] BDC as the organic linker.

aminoterephthalate ligand was used as a catalyst in the synthesis of propylene carbonate under batch conditions. The Ce Zr-MMOF was relatively stable with less leaching after 4 cycles. It is known that the presence of NH$_2$ as a substituent of the terephthalate ligand increases CO$_2$ adsorption of the MOF due to its basicity. In addition, bifunctional Lewis acid/base catalysts like UiO-66-NH$_2$(Zr/Ce), containing nodal defects with acid character and basic –NH$_2$ substituents, are very appropriate to promote CO$_2$ insertion into epoxides due to the dual activation of CO$_2$ by basic sites and epoxide by the nearby acid sites according to the mechanism indicated in Fig. 16. The role of Ce in UiO-66-NH$_2$(Zr/Ce) is to generate defective structural centers by effectively decreasing the coordination of the nodal joints. Appropriate control of the Ce/Zr ratio to 5% results in optimal UiO-66-NH$_2$(Zr/Ce).[293]

Zr-MMOFs have also found applications as photocatalysts and for adsorption.[299–302] Theoretical modeling of crystal orbitals in some Zr MOFs, however, indicates that the overlap between the empty Zr^{4+} 4d atomic orbitals and the π^* aromatic orbitals of the ligand is very poor, hampering an efficient photoinduced electron transfer from the electronically excited state of the linker to the metal node. Inserting additional metals in the structure of Zr-MMOFs can improve overlap between these two orbitals, resulting in increased photocatalytic activity. This is apparently the reason for the higher photocatalytic activity observed upon insertion of Ti in UiO-66(Zr). The 3d orbital of Ti is larger in size and higher in energy than the smaller 4d orbital of Zr; therefore, it is better suited to overlap with the terephthalate linker in its excited state.[303] Doping Zr with other metal ions can also lead to the enrichment of these metals on the outer surface, which can be correlated to better CO$_2$ adsorption and to the enhanced photocatalytic activity for CO$_2$ reduction. For instance, MIL-173(Zr/Ti), containing 5,10,15,20-tetrakis(3,4,5-trihydroxyphenyl)porphyrin as a linker

with 40% Ti, produces 381 and 145 μmol g^{-1} of H$_2$ and O$_2$, respectively, in an overall water splitting reaction that is higher than that of the single metal MIL-173(Zr) photocatalyst. The better photocatalytic activity of the mixed metal MIL-173(Zr/Ti) can be attributed to the (i) porphyrin linker, which acts as a natural light harvester with high absorption in the visible region, (ii) Ti 3d orbitals having a closer energy to the oxygen orbitals than Zr 4d orbitals, allowing better overlap to produce a crystalline orbital, (iii) decrease of the band gap, and (iv) higher efficiency of the photoinduced LMCT elementary step.[299]

In summary, Zr-MMOFs can be beneficial for diverse applications. Applying Zr in nodal positions with various metals, including Ti, Ce, or even Zn, can be focused on more in the future for catalytic transformations and photocatalytic reactions, including CO$_2$ hydrogenation or reduction. In the case of sensing applications, Zr-MMOFs are less investigated, but their synergistic effect can be explored with lanthanides. Due to the high porosity and stability of the Zr-MOFs, multi-metallic structure, especially with lanthanides in sensing applications can also be achieved. Although in electrocatalysis and energy storage, Zr-MOFs can provide higher stability, their non-electroactive intrinsic features can hamper their vast usage in the mentioned applications. Therefore, using the synergistic effect between Zr and Ni, Fe, Co, or even Mn can enhance their capability toward energy conversion and storage. Thus, it is believed that Zr-MMOFs with electro-active metal introductions can not only possess high stability but also provide higher activity toward energy applications, including batteries, supercapacitors, and water-splitting. But structural issues can also hamper this goal; therefore, optimizing the content of each metal can be vital.
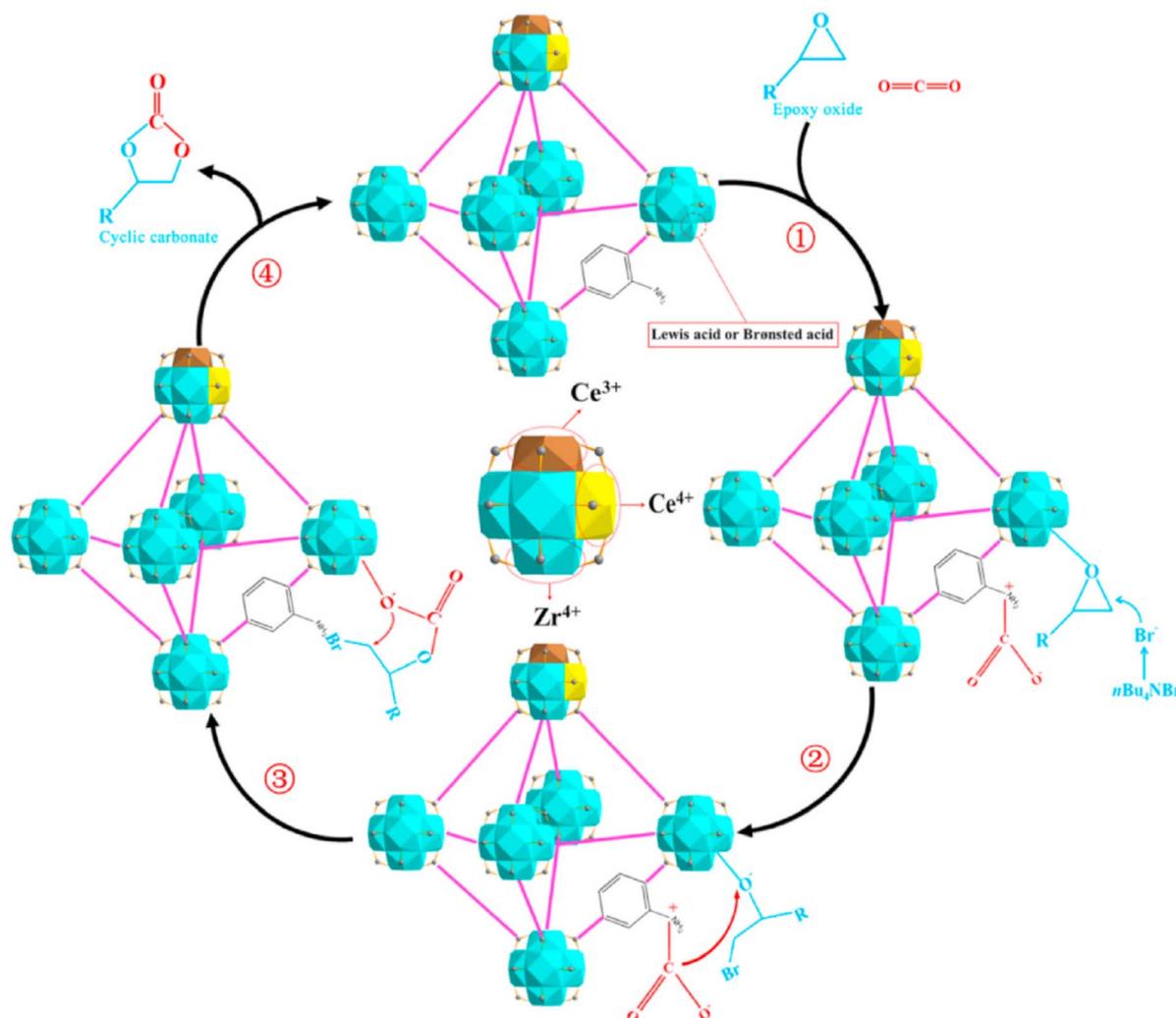
Fig. 16 Proposed mechanism for the cycloaddition of CO_2 and epoxides by a defective bimetallic UiO-66-NH$_2$(Zr/Ce) catalyst. (1) Through the catalyst, epoxy oxide is integrated with Lewis or Brønsted acid sites and is activated. Due to the presence of the −NH$_2$ group on the MOF, CO_2 is adsorbed and polarized; (2) the nucleophilic Br ion attacks the β carbon atom of epoxide to form the oxygen anion intermediate; (3) the intermediate interacts with CO_2 to create halogenated carbonate; (4) through internal cyclization, halogenated carbonate is converted into cyclic carbonate, while the catalyst is regenerated. Reproduced with permission from ref. 293, copyright 2021 Elsevier.

8. Zinc-based MMOFs

Zn is one of the transition metal elements that is highly biocompatible with the human body and can also act as an antibacterial and anti-inflammatory agent and possess medicinal properties. Zinc is a relatively inexpensive element that can be used as a substitute for more costly elements in the medical field, such as silver.[307,308] The Zn^{2+} ion is a vital component of the human body, fulfilling a multitude of essential functions. Zinc-based MOFs are employed in a multitude of fields, including medicine, sensing, and other areas. The several applications of Zn-MOFs in medicinal chemistry are due to the antibacterial properties of Zn^{2+}, as exemplified by TMU-3.[309] Such MOFs can provide a stable and long-lasting antibacterial effect by gradually releasing Zn^{2+} as an antibacterial agent. Zn-based MOFs possess the capacity to function as chemical sensors due to the luminescent properties of Zn complexes. Zn^{2+}, with a d^{10} electronic configuration with full d orbital

shells, is a suitable transition metal condition for the purpose of building a fluorescent probe. This phenomenon requires the placement of the desired ligand within the MOF structure, and the incorporation of another metal in conjunction with Zn has been reported as an effective strategy for fluorescence sensing and detection purposes.[310–312] Consequently, the incorporation of additional metals into the composition of Zn-based MOFs has the potential to yield diverse applications with enhanced performance, a subject that will be elaborated upon subsequently.

Zn-MMOFs exhibit novel properties and enhanced performance relative to their monometallic counterpart in medicine, as well as environmental pollutant adsorption and removal applications.[313–315] For example, Lin Wang and colleagues employed Mn-ZIF-8 to accelerate the healing of infected wounds. The incorporation of manganese ions was found to influence the activity of immune cells (macrophages and neutrophils) and inflammatory cells by modulating the

surrounding oxidation-reduction environment. Manganese nanoenzymes have the potential to perform the same functions as superoxide dismutase (SOD), glutathione peroxidase (GPx), and catalase (CAT). The final inhibitory effect on inflammation is exerted by copper, iron, and zinc. Zn in Mn-ZIF-8 was found to exhibit antibacterial activity, effectively destroying bacteria associated with infected wounds. Mn present in this MMOF is responsible for reducing inflammation, and the overall result is better wound healing through its SOD activity. Furthermore, the simultaneous presence of Mn^{2+}/Mn^{4+} in ZIF-8 frameworks enables the scavenging of excessive reactive oxygen species (ROS). It was clearly proven that bimetallic Mn-ZIF-8 exhibits an enhanced performance relative to its monometallic counterparts. The incorporation of 20% Mn into the ZIF-8 structure improves its bactericidal efficacy approximately two-fold with respect to ZIF-8, thereby substantiating its role as a key contributor. The combination of the two metals results in a synergistic effect that enhances the performance of Mn-ZIF-8. Fig. 17 illustrates the synthesis of bimetallic Mn-ZIF-8 and its action mechanism, accelerating the healing of infected wounds.[313]

Compared to MMOFs based on Ni, Co, and Fe, the number of reports exploring Zn-MMOFs as electrocatalysts is relatively limited, but from the existing literature, it can be concluded that the incorporation of Zn ions into the MMOF structure can assist the electrocatalytic activity of the resulting MMOF. Thus, typically Zn/M MOFs exhibit lower charge transfer resistance and higher electrical conductivity. Due to its d^{10} electronic configuration in its orbital, Zn^{2+} ions can shuttle electrons to other metal ions with open d orbitals in their valence shell and stabilize the structure in the alkaline environment. As an example, Zn adjacent to other electronegative metal ions was found to increase NH_3 yield and electrocatalytic NRR activity. In one example of the application of Zn-based bimetallic MOFs for the OER, the performance of pillared MnZn-MUM-1 $[(Zn_2(\mu_4\text{-}odba)_2(\mu\text{-}bpdh)]_n \cdot n$DMF; odba: 4,4′-oxydibenzoic acid and bpdh: 2,5-bis(4-pyridyl)-3,4-diaza-2,4-hexadiene) grown on NF having various ratios of Mn and Zn was studied.[316] It was found that $Mn_{0.5}Zn_{0.5}$-MUM-1 exhibits excellent OER performance compared to its counterparts, measuring an overpotential of 253 mV and a Tafel slope of 73 mV dec^{-1} at a current density of 10 mA cm^{-2}, and a high C_{dl} proficiency of 9.2 mF cm^{-2}. These values indicate that $Mn_{0.5}Zn_{0.5}$-MUM-1 exhibits excellent OER activity and the chronoamperometric measurements shown in Fig. 18 indicate that this material also has great stability after 6000 cycles. It has been proposed that the reason behind the
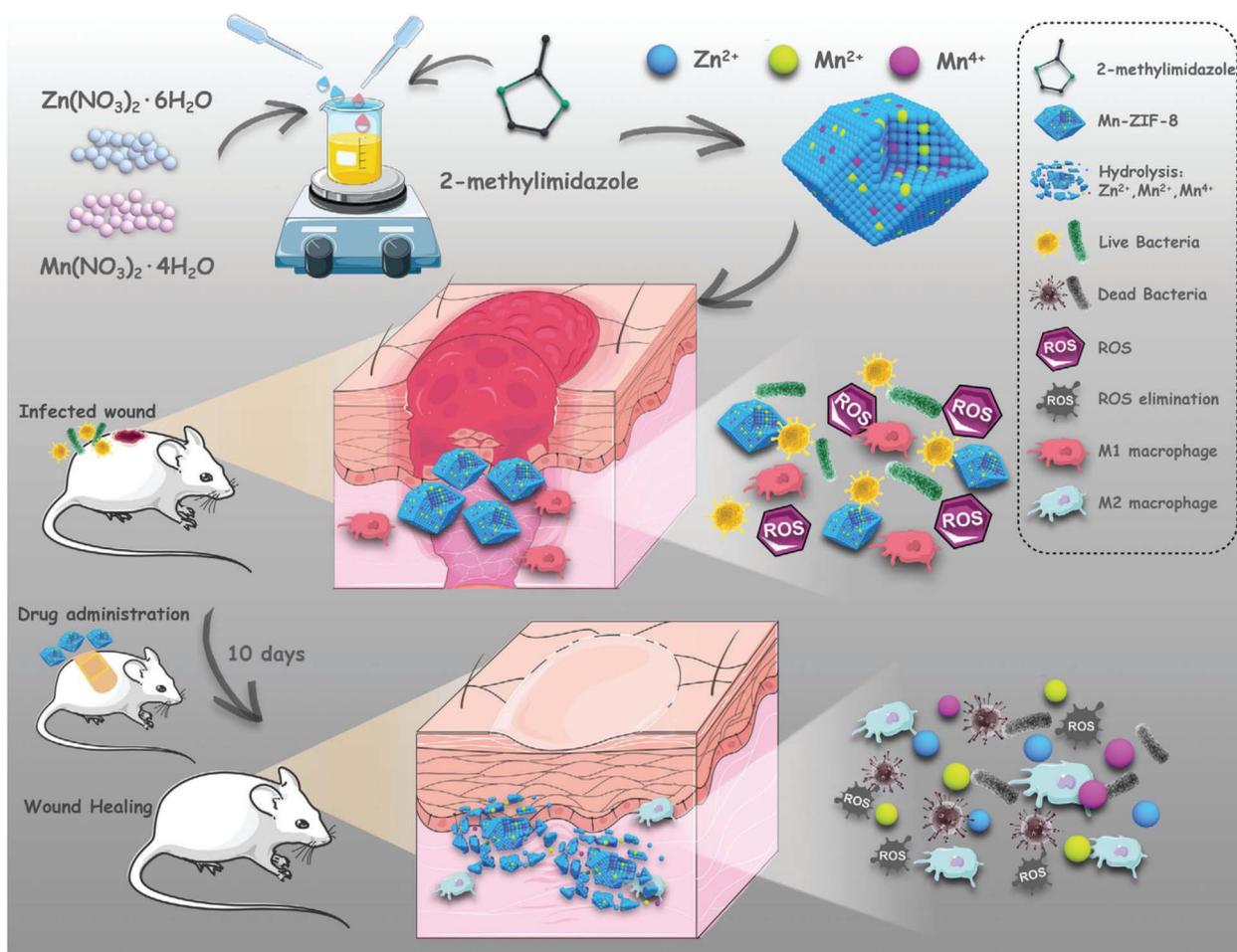

Fig. 17 Synthesis of bimetallic Mn-ZIF-8 and its healing mechanism on infected wounds. Reproduced with permission from ref. 313, copyright 2021 Wiley.
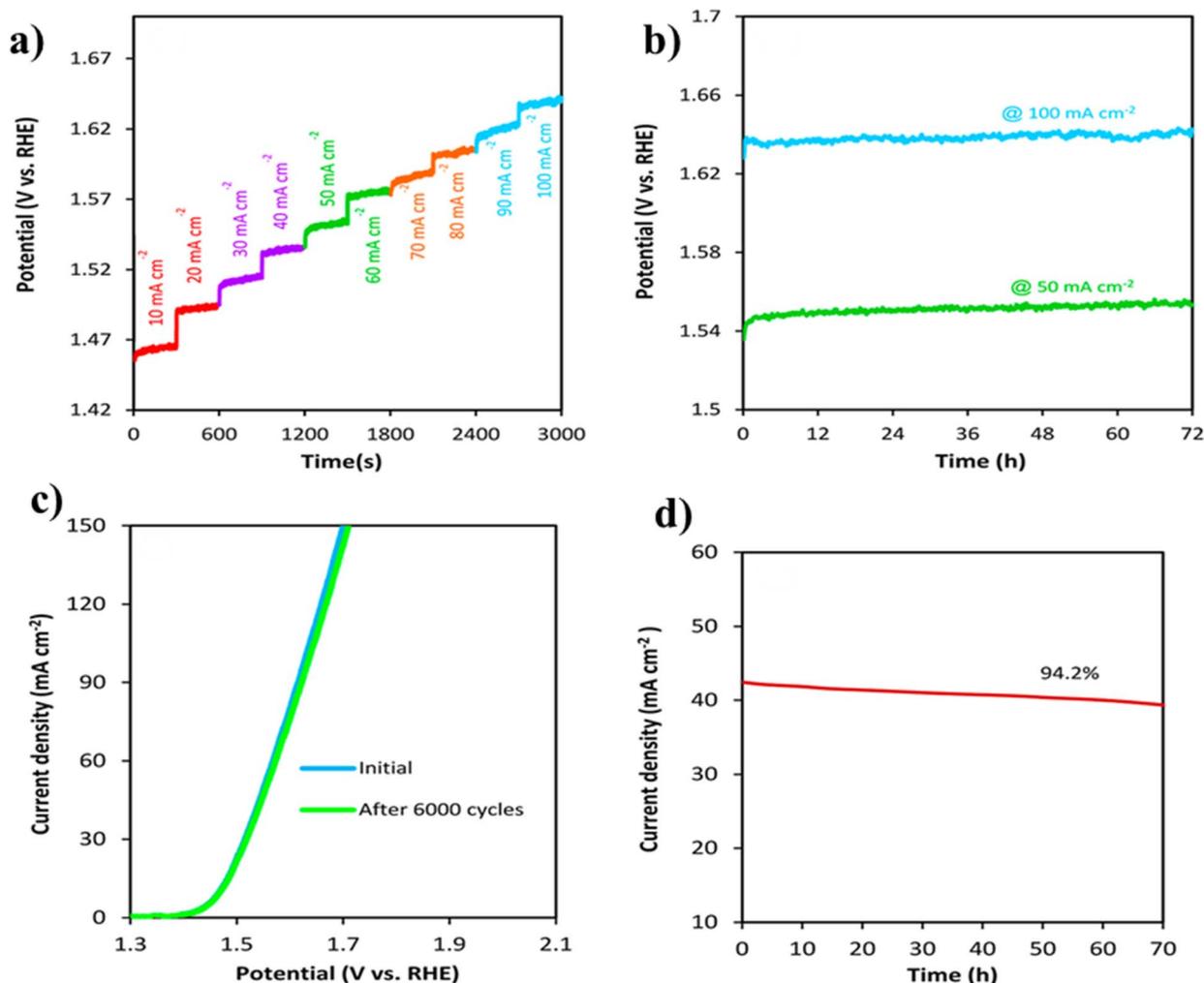

retains 91.1% of its initial capacity in 6000 cycles. Mechanistic studies indicate that Zn storage on MNi-MnO/PC occurs through co-intercalation of H^+ and Zn^{2+}.[210]

Regarding the use of Zn-MMOFs in thermal catalysis, it has been reported that the combination of heavy metal ions with Zn into the MOF structure increases accessibility to the heavy metal active sites by the porosity of the MOF, while the different affinity to ligands of Zn and heavy metals can serve to regulate the resulting catalytic activity. Thus, it is known that Zn-MOFs cannot activate oxygen molecules, but the incorporation of a heavy metal can introduce this catalytic activity, thereby resulting in a catalyst with interesting aerobic oxidation activity. In contrast to oxygen activation, Zn can activate H_2 and control hydrogenation selectivity. One well-known case is selective CO_2 hydrogenation to methanol, in which the combination of Cu and Zn is necessary to drive methanol formation. In a realization of this concept in Zn-MMOFs, bimetallic MOF-74(Zn) (2,5-dihydroxyterephthalte as the linker) was prepared by mechanochemical synthesis. Cu was incorporated subsequently, taking advantage of the dual coordination sites of the linker, either at the carboxylate sites or at the phenolic hydroxyl groups in Zn-based MOFs. The generation of defects by further mechanochemical treatment of desolvated samples results in an amorphous, low surface area and non-porous a-ZnCu-MOF-74 that presents better catalytic activity for CO_2 reduction and selectivity toward methanol compared to inactive monometallic Cu-MOF-74 and crystalline ZnCu-MOF-74. The reasons behind the better catalytic activity and selectivity of the catalyst are related to the following: (i) Zn increases the binding energy of the reaction intermediates decreasing activation energy and providing more attainable active sites, (ii) the incorporation of defect sites in the MOF increases the number of active sites, and (iii) the amorphization reduces the surface area, but it also decreases the particle sizes and alters the coordination environment of the nodes in MOF-74, therefore augmenting the methanol productivity.[319] In one of these examples related to catalysis, bimetallic $[Cd_2Zn\text{-}(DPTTZ)_{0.5}(OBA)_3(H_2O)(HCOOH)]$ (DPTTZ = 2,5-di(4-pyridyl)thiazolo[5,4-d]thiazole and OBA = 4,4′-oxybis(benzoic acid)) was found to exhibit good performance as a catalyst in cyclooctene epoxidation.[320] Good yields were obtained with this CdZn-MMOF after optimization of various parameters in the material including: (i) the reaction temperature, since higher temperatures facilitate overcoming the activation barrier of the rate-limiting step, (ii) the nature of the oxidizing reagent, since tert-butylhydroperoxide (TBHP) was found to be more convenient than H_2O_2 in aqueous medium, (iii) catalyst amount, since a higher amount leads to higher yields, (iv) reaction time, with optimum times avoiding overoxidation and epoxide decomposition, (v) solvent, with epoxidation performing better using CCl_4 due to its low coordination capability and low dielectric constant which can impact diffusion to the active centers, whereas complexing solvents reduce the epoxide yield by inhibiting the coordination environment around the metal center, and (vi) the presence of a co-catalyst and Lewis acid, since the presence of Al^{3+} ions as Lewis acid sites leads to enhanced reactivity.[320] In one study, a Pb, Zn-based bimetallic MOF, namely $[PbZn_{0.5}L(H_2O)]_{0.5}NMP\cdot\{H_2O\}_n$

(L: 1H-tetrazol-5-yl)terephthalic acid, (NMP: N-methyl-2-pyrrolidone) was synthesized for catalysis.[321] The ligand selection, synthesis, and resulting structure of PbZn-MMOF follow the rules of the hard-soft acid–base theory, since Pb has a preference to coordinate with the oxygen atoms of the carboxylate groups, while Zn coordination occurs through the N atoms of the tetrazole unit. In that way, while monometallic Pb or Zn with the tetrazolylterephthalate does not form porous structures, the bimetallic Pb,Zn-MMOF is a porous framework, thus corresponding to a MOF material that requires porosity as a structural property.[321] This PbZn-MMOF is a catalyst for CO_2 fixation onto epoxides to form cyclic carbonates, a reaction of importance to obtain solvents and monomers.[321] Up to 98% yield for CO_2 conversion was achieved for epichlorohydrin 1-butene oxides using tetra N-butylammonium bromide as a co-catalyst. In this PbZn-MMOF, Zn provides porosity in structure, and the synergistic structural effect between them results in a highly stable porous MOF achieving CO_2 conversion efficiencies of up to 98%. The two reaction mechanisms were suggested to involve either interaction of epoxide O atoms with the Lewis sites of the MOF with the assistance of the bromide to the epoxide ring opening or activation of CO_2 by the MMOF.[321]

In total, Zn-MMOFs can be used as electrocatalysts and in energy storage systems, because they can facilitate charge transfer. Therefore, the synergistic effect between Ni, Co, and Mn can be beneficial for energy applications. Due to its d^{10} electronic configuration in its orbital, Zn^{2+} ions can shuttle electrons to other metal ions with open d orbitals in their valence shell and stabilize the structure in the alkaline environment; therefore, it can not only be beneficial for energy applications but also can be useful for photocatalysis, catalysis, and sensing applications. Table 5 summarizes recent work on Zn-MMOFs for various applications, including key performance metrics.

9. Lanthanide-based MMOFs

In recent years, multi-metal MOFs based on lanthanides (La-MMOFs) have been the subject of considerable scientific interest especially in sensing applications.[328,329] However, the use of La-MMOFs as catalysts is considerably less explored.[330,331]

Lanthanides have partially filled 4f orbitals, which provide many accessible electronic levels, leading to interesting optical properties. Except for $Lu^{3+}(4f^{14})$ and La^{3+} ($4f^0$), all lanthanide ions exhibit luminescence emission, some in the visible region and some in the near-infrared region. The electronic transitions observed in lanthanide-based polymetallic MOFs, including charge transfer (such as metal-to-metal charge transfer (MMCT), metal-to-ligand charge transfer (MLCT), and ligand-to-metal charge transfer (LMCT) charge transfer) and 4f–5d transitions, can result in atomic emission from the lanthanide ions.[332]

The unique behavior of some luminescent MOFs to respond to specific external stimuli by modifying the emission intensity or turning the emission off and on has attracted the attention of the scientific community.[333] La-MMOFs have demonstrated efficacy in sensing a range of analytes, including small

Table 5 Summary of reported Zn-MMOFs or derived materials, indicating their use and their performance[a]

Zn-MMOF	Other metals	Applications	Efficiency	Ref.
$Mn_{0.5}Zn_{0.5}$-MUM-1	Mn	Electrocatalyst/OER	C.d: 10/O.v: 253/T.f: 73	316
$Zn_{0.33}V_{0.66}$-MOF/NF[b]	V	Electrocatalyst/UOR	C.d: 50/O.p: 1.42/T.f: 122	67
NiCoZn-BDC-MOF	Ni/Co	Supercapacitor	S.p: 582.8/C.d: 5 (3000 cycle)/ E.d: 40.47/P.d: 687.5/ retention: 92.44%	317
CDZ-20	Cu	Photocatalyst/water splitting	H_2 generation rate: 13.9/ Bandgap: 4.42/AQE: 9.08%/ P.D: 34	322
Cu@ZIF-8	Cu	Catalyst/hydrocarbon oxidation	16%/120 °C/O_2/24 h/ selectivity: 85%/reuse: 2 cycles	323
Cu@ZIF-8	Cu	Catalyst/hydrogenation of alkenes	>99%/RT/$N_2H_4.H_2O$/14 h/ selectivity: 99%/reuse: 3 cycles	324
NUC-51a	Ba	Catalyst/knoevenagel condensation reaction	97%/55 °C/n-Bu$_4$NBr/5 h/ selectivity: 99%/TON: 97.2/ TOF: 16.2/reuse: 5 cycles	325
PtZn-MOF-74	Pt	Catalyst/CO oxidation	E_a: 101.31/TOF: 2.32/reuse: 5 cycles	326
a-ZnCu-MOF-74	Cu	Catalyst/CO_2 reduction	E_a: 78.6/200 °C/selectivity: 99%	319
IUST-4	Cd	Catalyst/epoxidation reaction of olefins	99%/TBHP/60 °C/4 h/ selectivity: 99%/reuse: 5 cycles	320
$[PbZn_{0.5}L(H_2O)]_{0.5}NMP\{H_2O\}_n$	Pb	Catalyst/CO_2 conversion	98%/TBAB/RT	321
Zn/Ca-MOF[c]	Ca	Sensing/Fe^{3+} and $Cr_2O_7^{2-}$	Detection limits: 18.8 μM for Fe^{3+} and 29.1 μM for $Cr_2O_7^{2-}$	327

[a] C.d: current density based on A g^{-1} or mA cm^{-2} for energy applications/O.v: overpotential based on mV/T.f: Tafel slope based on mV dec^{-1}/C.v: cell voltage based on V/O.p: onset potential based on V and S.p (specific capacitance) is based on F g^{-1}, C g^{-1}, and mAh g^{-1}/E.d: energy density based on Wh kg^{-1}/P.d: power density based on W kg^{-1}/all percentages in the photocatalyst or catalyst represent the yield, conversion or any efficiency of MMOFs; for further details, see the references/bandgap based on eV/apparent quantum efficiency (AQE)/photocurrent density (pd) based on μA cm^{-2}/RT: room temperature/TOF: turnover frequency/TON: turnover number/E_a: energy activation based on kJ mol^{-1}/for further details, see the references. [b] Linear N-donor piperazine (Hprz), rigid planar imidazole-4,5-dicarboxylate (IDC^{3-}) as linkers. [c] 5,5'-(Propanen-1,3-diyl)-bis(oxy) diisophthalic acid as the linker.

molecules, ionic species, pH, explosives, and temperature, due to these optical properties of lanthanides. Moreover, the intrinsic chemical and structural attributes of MOFs containing lanthanides render them valuable in bioassays. Illustrative examples of the use of La-MMOFs for sensing are described below.[332]

The sensing of hydrogen peroxide, as one ROS in living organisms, is significant, for example, to gain a deeper understanding of the mechanism of activity enhancement and the early detection of plant health. In this context, Kun Wang *et al.* reported a bimetallic-Ce/Zr organic framework (Ce/Zr-MOF) that demonstrated enhanced performance in mimicking enzymatic peroxidase activity. The peroxidase (POD) activity of the bimetallic–organic Ce/Zr framework was found to be higher than those of the corresponding monometallic MOFs. In addition to exhibiting sensing properties, this Ce/Zr metal framework also displays catalytic characteristics. In the catalytic cycle, the Ce and Zr redox cycles operate synergistically, enhancing the activity of POD and facilitating the highly sensitive detection of hydrogen peroxide. The biosensor can be quantitative, being capable of providing information regarding the concentration of hydrogen peroxide. The color change is visually discernible to

the naked eye, obviating the need for expert interpretation and rendering the process highly accessible. The enhanced POD-like activity mainly relied on the incorporation of Ce, which enhanced the conductivity and electron transport capability of Ce/Zr-MOF and boosted the production of ˙OH.[334]

Mercury ions are highly toxic, and their detection and quantification are crucial for human health and the quality of water, food, and medicine. Mercury detection has attracted the attention of numerous scientists, who have sought to develop more efficient methods for measuring Hg^{2+} ions. In response to this need, Lian Xia and colleagues synthesized a bimetallic La-MMOF using Ce^{4+} and Eu^{3+} and a 5-boronoisophthalic acid (5-bop) ligand for Hg^{2+} ion sensing. The LMCT in Ce^{4+} is more facile due to the lower energy of its 4f empty band in comparison to the Eu^{3+} ion. Consequently, Ce^{4+} exhibits a greater capacity to absorb energy than Eu^{3+}. For this reason, Ce^{4+} exhibits a more extensive and robust fluorescent emission than Eu^{3+}. Upon exposure to Hg^{2+}, the bimetallic La-MMOF undergoes an LMCT, whereby the boric acid group is replaced by a mercury ion. This process considerably disturbs the emission of the EuCe-MMOF, resulting in a decrease in the fluorescence intensity of Eu^{3+} and an increase in the
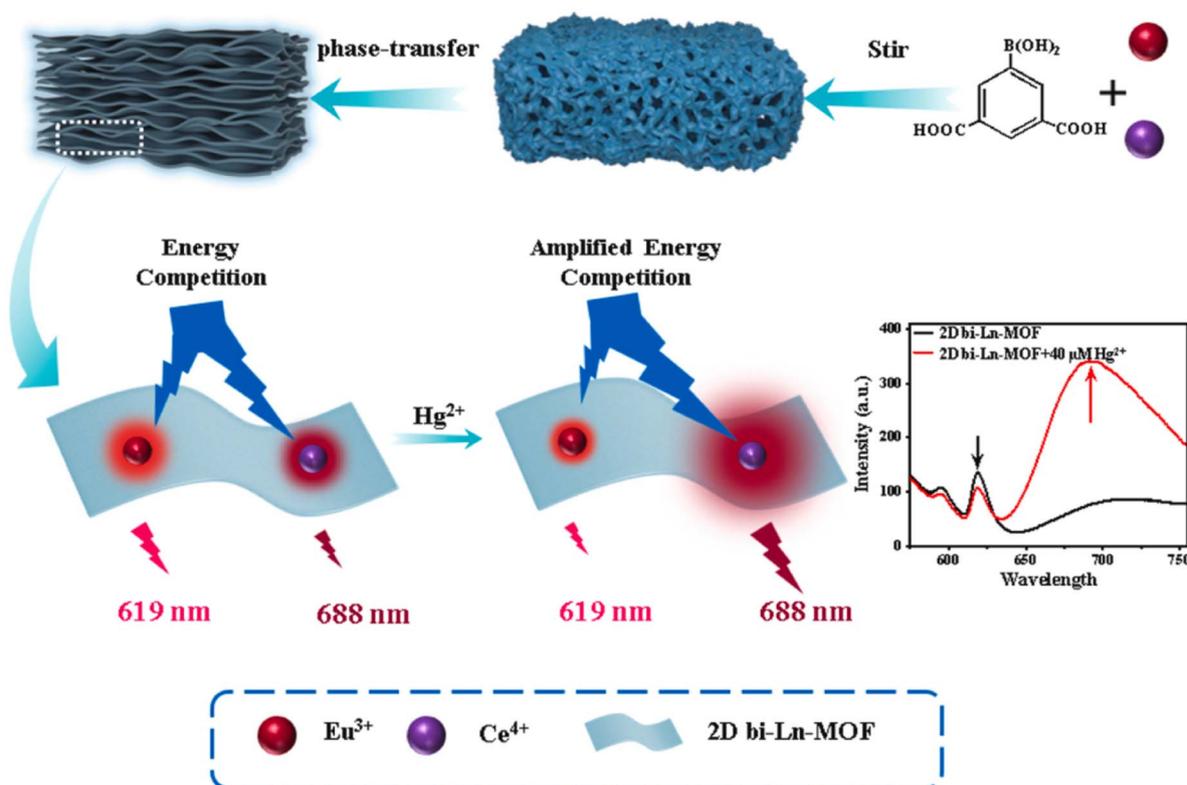
Fig. 19 Synthesis of bimetallic La–MMOF and its application in the detection of Hg^{2+} ions. Reproduced with permission from ref. 328, copyright 2024 Elsevier.

fluorescence intensity of Ce^{4+}. This behavior makes the bimetallic CeEu-MOF capable of detecting Hg^{2+} with high selectivity. The employment of this bimetallic MMOF instead of the monometallic analogs results in the improved detection of Hg^{2+} with a lower detection limit and higher selectivity (Fig. 19).[328]

In another report on the use as a sensor of a bimetallic La-MMOF, Eu/Zr-UiO-66 was synthesized to quantify volatile organic compounds (VOCs), with a particular focus on cyclohexanone and styrene. The BDC ligand in this MOF exhibits a strong emission effect due to the π-system in its aromatic

Fig. 20 XPS data of (a) Ce 3d and (b) O 1s for CeO_2 and porous $Ce_{0.9}Tb_{0.1}O_y$ obtained by thermal treatment of the corresponding MMOF. Reproduced with permission from ref. 337, copyright 2019 Elsevier.

Table 6 Summary of reports on La-MMOFs or derived materials for diverse applications with some metrics regarding their efficiency[a]

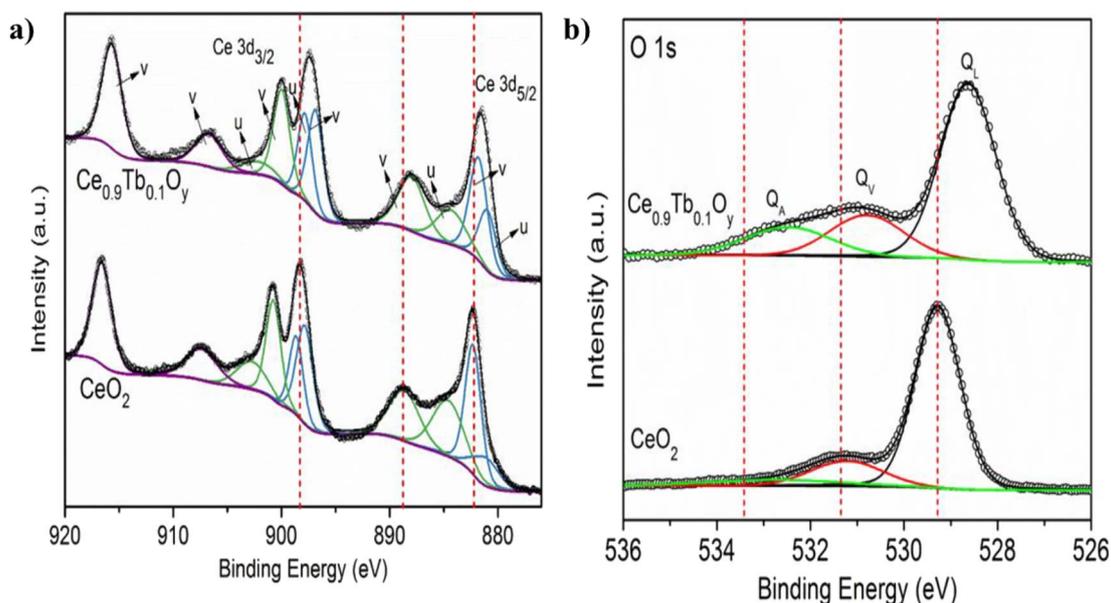| La-MMOFs	Other metals	Applications	Efficiency	Ref.
Ce-MOF@Pt[b]	Pt	Electrocatalyst/water splitting	C.d: OER and HER: 10/O.v: OER: 340 and HER: 208/T.f: OER: 47.9 and HER: 188.1	330
Pd/LaQS	Pd	Catalyst/hydrogenation of furfural	>99%/30 min/selectivity: 99%/reuse: 4 cycles	331
Ce-UiO-Co	Co	Catalyst/methane oxidation to methanol	2166 mmol $g_{cat}^{-1}/H_2O_2/80$ °C/ selectivity: 99%/TON: 3250	78
NUC-56a	In	Catalyst/knoevenagel condensation reaction	96%/65 °C/n-Bu$_4$NBr/7 h/TON: 960/TOF: 137/reuse: 10 cycles	340
Tb–Ce-MOFs[c]	—	Sensing/phosphate ion	LOD: 28 nM/metrics: water	341
Eu$_{0.048}$Tb$_{0.052}$Gd$_{0.9}$-CPBA	—	Sensing/glyphosate	LOD: 0.47 μM/metrics: water	342
Tb$_{0.4}$/Eu$_{0.6}$-BTC	—	Sensing/dipicolinic acid	LOD: 4.9 nM/metrics: soil and water samples	343
Cu/UiO-66	Cu	Sensing/chloramphenicol	LOD: 0.09 nM/metrics: fish	344
Tb$_{0.6}$Eu$_{0.4}$-MOF[b]	—	Sensing/sulfamerazine	LOD: 0.1 μM/metrics: fish	345
Eu$_{0.05}$Tb$_{0.95}$L[c]	—	Sensing/nitrofurazone	LOD: 0.013 μM	346
Eu/Zr-MOFs[c]	Zr	Sensing/acrylamide	LOD: 2.4×10^{-8} M/metrics: food	347
Eu$_{0.07}$Gd$_{0.03}$-MOF[d]	—	Sensing/Fe^{3+}	LOD: 0.091 μM/metrics: water	348
Eu$_{0.075}$Tb$_{0.925}$-MOF	—	Sensing/Fe^{3+}	LOD: 2.71×10^{-7} M to 8.72×10^{-7} M/ metrics: water	349
Zn$_3$Eu$_2$-L[e]	Zn	Sensing/Fe^{3+}	LOD: 1.14 μM	350
Zn/Eu-MOF	Zn	Sensing/ofloxacin	LOD: 0.44 μM/metrics: food	351
La-MOFs	—	Sensing/F$^-$	LOD: 96 ppb/metrics: water	352
Eu/Tb(BTC)	—	Sensing/*Bacillus anthracis*	LOD: 1087 nM	353
Tb$_{0.9}$Gd$_{0.1}$-PBA	—	Sensing/anthrax biomarker	LOD: 1.03 μM/metrics: urine and water	354
Eu$_{2.2}$Tb$_{97.8}$-TCA	—	Sensing/water	LOD: 0.016% v/v/metrics: organic solvent	355
Eu$_{0.00667}$Tb$_{0.99333}$[f]	—	Sensing/temperature	CIE coordinate of (0.3333, 0.3394), wavelength of 350 nm	356
Fe/Eu-MOF	Fe	Sensing/serum alkaline phosphatase (ALP)	LOD: 0.9 U L^{-1}	357
Eu/Zr-MOFs[c]	Zr	Sensing/acrylamide	LOD: 2.4×10^{-8} M	347
EuTb-MOF-1	—	Sensing/Pb^{2+} sulfamethoxazole (SMZ) sulfadiazine (SDZ)	LOD: 0.037 μM 0.041 μM/metrics: water	358
Tb$_{1.7}$Eu$_{0.3}$(BDC)$_3$(H$_2$O)$_4$	—	Sensing/dipicolinic acid (DPA)	LOD: 2 to 100 μM/metrics: water	359

[a] C.d: current density based on A g^{-1} or mA cm^{-2} for energy applications/O.v: overpotential based on mV/T.f: Tafel slope based on mV dec^{-1}/C.v: cell voltage based on V/O.p: onset potential based on V and S.p (specific capacitance) is based on F g^{-1}, C g^{-1}, and mAh g^{-1}/E.d: energy density based on Wh kg^{-1}/P.d: power density based on W kg^{-1}/all percentages in the photocatalyst or catalyst represent the yield, conversion or any efficiency of MMOFs; for further details, see the references/bandgap based on eV/apparent quantum efficiency (AQE)/photocurrent density (pd) based on μA cm^{-2}/RT: room temperature/TOF: turnover frequency/TON: turnover number/E_a: energy activation based on kJ mol^{-1}/for further details, see the references. LaQS: La-based metal–organic framework; CPBA: 3,5-bis-(3-carboxyphenoxy)benzoic acid; TCA: 4,4′,4″-nitrilotribenzoic acid. [b] BTC as an organic linker. [c] NH$_2$-BDC as the linker. [d] 2,3,5,6-Tetrafluoroterephthalic acid (H$_2$tfBDC) as the linker. [e] H$_6$TTHA: 1,3,5-triazine-2,4,6-triamine hexaacetic acid as the linker. [f] H$_2$TDC: 2,5-thiophenedicarboxylic acid as the linker.

rings, which is enhanced by the addition of Eu^{3+}. The bimetallic MOF displays a higher fluorescence intensity than UiO-66, which can be attributed to the "antenna effect" and the strongest $^5D_0 \rightarrow {}^7F_2$ transition. In this study, the fluorescence intensity of Eu/Zr-UiO-66 was investigated in the presence of different VOCs. It was observed that the fluorescence intensity of the MOF increased by 54% when exposed to cyclohexane and decreased by 76% when exposed to styrene. However, in the presence of other VOCs, no discernible change was observed. Styrene as a VOC displays greater sensitivity and larger fluorescence change compared to aliphatic compounds. This higher response for styrene can be attributed to the effect of the aromatic ring and its p electron cloud, which should interact better with the metal ions and the MOF terephthalate linker. As the UV absorption spectrum of cyclohexanone and styrene overlaps with the emission spectrum of Eu/Zr-UiO-66, exposure of this compound to cyclohexanone and styrene results in a decrease in emission intensity and cessation of emission due to the fluorescence resonance mechanism and energy transfer, in which light emitted by the terephthalate linker is absorbed by

the analytes and not detectable. This is attributable to the synergistic effect of the two metals and the superior performance of a bimetallic MOF in comparison to a monometallic one.[329] Besides fluorescence and VOC sensing ability, other collateral effects of the incorporation of Eu^{3+} in the MOF structure are a more uniform pore distribution and a larger surface area in Eu/Zr-UiO-66 (1 : 9) compared to a monometallic Zr-UiO-66.[329]

In a synthesis of La-MMOF reported by de Azambuja, Parac-Vogt, and co-workers, Zr/Ce-MOF-808 was obtained, which can function as a peptidase enzyme. The role of Ce^{4+}, in this case, is of particular importance to enhance the enzymatic activity of MOF-808, as Ce^{4+} is a more efficient center for peptide bond hydrolysis than Zr^{4+}, which explains the enhanced performance of the bimetallic MOF in comparison to the monometallic.[335] Furthermore, Ce^{4+} increases the durability of this MMOF in an aqueous environment. This is a crucial point regarding the catalytic activity as demonstrated in this and other examples.

In another instance, Li, Yang, and coworkers reported a bimetallic La/Ca-BDC MOF for the application of phosphate
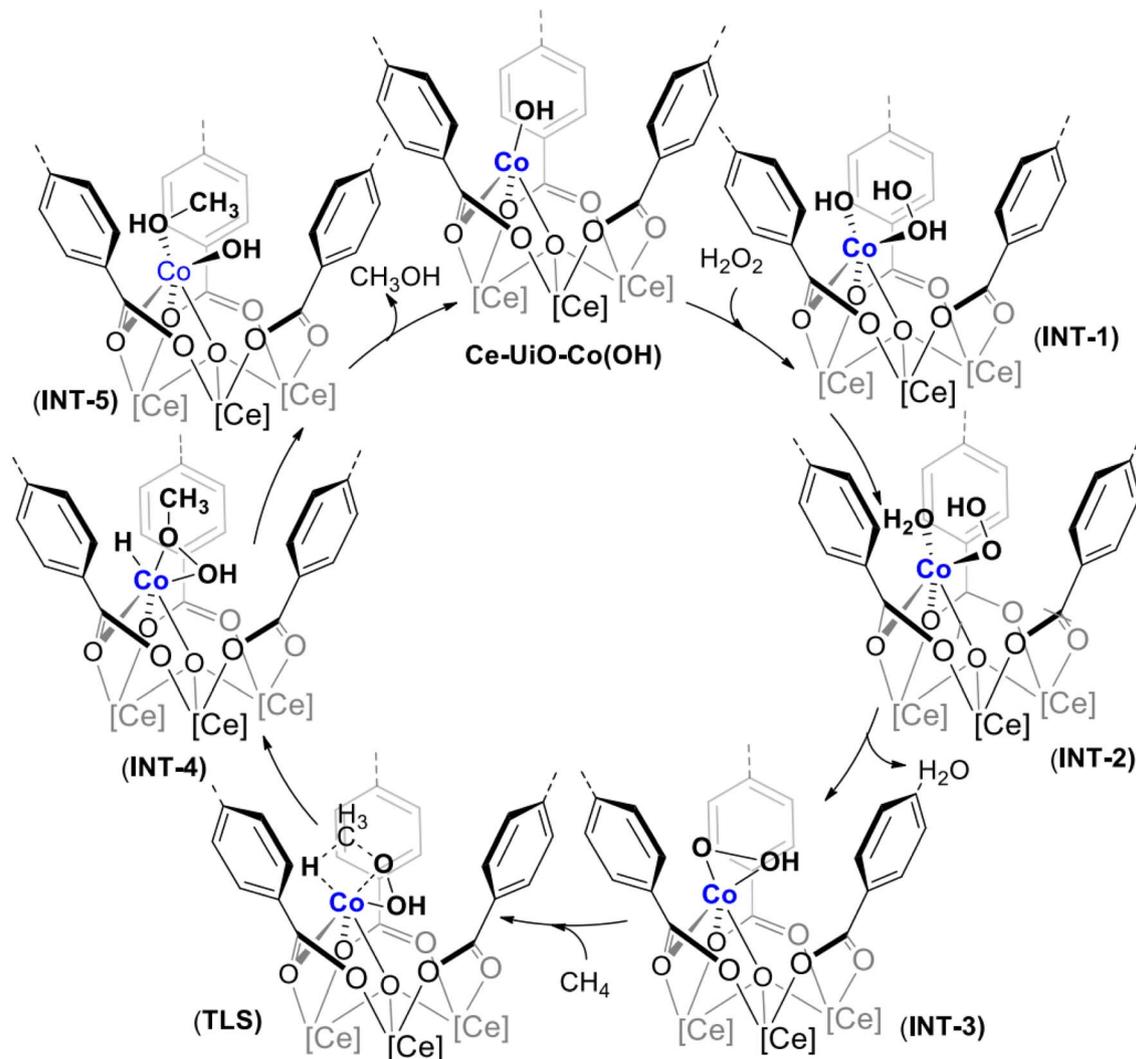
Fig. 21 Proposed mechanism for the activation of methane by Ce-UiO-Co MMOF. Reproduced with permission from ref. 78, copyright 2022 American Chemical Society.

removal in water. By incorporating Ca into a La-BDC MOF, the phosphate removal capacity was significantly increased. In addition, this bimetallic MOF works in a wide range of pH from 3 to 9, which indicates the high performance of this bimetallic MOF in comparison to La-BDC, particularly under basic pH values.[336]

As previously stated, the measurement of H_2O_2 in biological fluids is important because this substance, despite its low toxicity, has the potential to generate ROS responsible for damaging carbohydrates, proteins, and lipids. It has been proposed that hydrogen peroxide formed as a byproduct of aerobic metabolism can accumulate in the body causing oxidative stress that may result in cell malfunction. Consequently, scientists have devised various methods for measuring this substance. In this context, it is known that certain metal oxides, including TiO_2, MnO_2, Co_3O_4, CeO_2, and Fe_2O_3, can be used for the detection of hydrogen peroxide. Among these metal oxides, CeO_2 has garnered particular interest from scientists in the fields of medicine and biology for its ability to decompose

hydrogen peroxide mitigating the negative effects of free ROS and its effective catalytic activity. In this regard, Guo et al. have reported the synthesis of two metal oxides derived from bimetallic rare earth homotypic metals to measure hydrogen peroxide, where homotypic indicates that the Ce and the second rare earth metals are similar in properties and exchangeable.[337] Two issues were taken into consideration during the development of this sensor. First, the researchers employed two homotypic metals to ascertain the potential for a synergistic effect, in addition to the similar properties of the homotypic elements. As is generally the case when two elements with similar atomic mass, oxidation state, and radius are substituted, this substitution results in the formation of a highly stable framework. The utilization of a porous MOF precursor facilitates the generation of a large surface area and precise channel interconnections, which finally leads to an enhanced sensing efficiency.[337] Accordingly, MMOFs were employed as a precursor to prepare homotypic porous bimetallic oxides. To this end, the $Ce_{0.9}Tb_{0.1}$-MOF (BTC as linker)

crystal was initially synthesized, with its XRD peaks agreeing with those of Ce-MOF. Upon heating the material to 400 °C in air, the Ce-MMOF underwent decomposition, resulting in the formation of the $Ce_{0.9}Tb_{0.1}O_y$ crystal through the MOF-derived process. The XRD pattern of the obtained mixed oxide is consistent with the crystallography of CeO_2. The resulting solid oxide exhibits some of the characteristics of $Ce_{0.9}Tb_{0.1}$-MOF, particularly its porosity. The formation mechanism of the final micron-sized porous $Ce_{0.9}Tb_{0.1}O_y$ is proposed to occur in two steps, in which first $Ce_{0.9}Tb_{0.1}$-MOF decomposes, forming bimetallic oxide nanoparticles that, in a second step, undergo sintering of the bimetallic nanoparticles and growth, giving rise to micron-sized crystals but retaining a considerable degree of porosity. Compared to CeO_2, the bimetallic oxide sample exhibits a larger pore volume and surface area, thereby providing a higher density of accessible catalytic sites. XPS was used to investigate the surface composition and oxidation states of both CeO_2 and $Ce_{0.9}Tb_{0.1}O_y$ samples. The comparison of these two spectra shows that the relative O_y percentage on the surface of $Ce_{0.9}Tb_{0.1}O_y$ is higher than that of the monometallic crystal. The Ce^{3+} ion plays a role in the electron transfer rate. Ce^{3+} content in $Ce_{0.9}Tb_{0.1}O_y$ is higher than that in CeO_2. This indicates that by incorporating Tb in the crystal structure, it is possible to increase the content of Ce^{3+}, showing a higher sensing ability in detecting H_2O_2 using $Ce_{0.9}Tb_{0.1}O_y$ in comparison to CeO_2 (Fig. 20).[337] All reported sensing and other applications in La-MMOFs are summarized in Table 6.

La-MMOFs have been much less investigated for applications related to electrocatalysis, catalysis, and removal.[330,338,339] For La-based bimetallic MOFs used as catalysts, an example worth mentioning is bimetallic Ce-UiO-66-Co, which exhibits lower activation energy for chemoselective methane oxidation to methanol by H_2O_2 under high pressure than the Zr-UiO-66-Co counterpart, resulting in better catalytic performance for the former.[78] This better performance of Ce-UiO-66-Co was attributed to: (i) the higher activity and selectivity for Ce compared to when Zr is in the structure, (ii) the higher electron deficiency on Co due to the electronegativity of the Ce^{4+}-oxo cluster node that renders Co more similar to a Co^{3+} species, thereby enhancing C–H activation of methane via σ-bond metathesis, and (iii) a certain increase in pore size for Ce-UiO.[78] Mechanistic studies on bimetallic Ce-MOFs have led to the proposal that coordination of H_2O_2 to Co ions, followed by removal of H_2O, results in the formation of a Co–OOH intermediate. A scheme of the proposed mechanism of methane activation by Ce-UiO-66-Co is depicted in Fig. 21. Subsequent steps involve the formation of a CH_3–O bond by σ-bond metathesis between the C–H bond of methane and the Co–O bond of Co–OOH. Finally, CH_3OH is released by the replacement of the Ce–OCH_3 bond by Co–OH, closing the catalytic cycle.[78]

Lanthanide incorporation is the most frequently employed strategy in MMOFs and derivatives for application in sensing, due to the remarkable atomic fluorescence properties of these metals. From the existing literature, it appears that co-incorporation of more than one lanthanide element is generally favorable and can increase sensing efficiency even more.

Although Ln-based MMOFs are less investigated in energy applications, findings indicate that they can have intrinsic activity in water-splitting, especially doping or incorporation of Ce into the structure of MMOFs, which can augment electrocatalytic activity and serve to introduce structural defects, which should increase the number of active sites, thereby boosting the catalytic performance with respect to the parent monometallic MOF. In the future, besides focussing on sensing properties of La-MMOFs, but also can be demanding to explore the role of lanthanides in La-MMOFs in the electro-/photocatalysis, catalytic organic transformations, and pollutant removal.

10. Conclusions

A simple procedure for synthesizing MMOFs is always beneficial for any application. Especially suitable methods are *in situ* or one-pot synthesis, since they are the simplest methods, consisting of the formation of MMOFs from a mixture of all components. Also, the use of preformed clusters can be a practical strategy with the advantage of fine control of the molar ratio of the metals prior to the formation of MMOFs, which appears to be very appropriate considering that an optimal molar ratio is usually required to achieve the highest efficiency in most applications. For energy storage applications with Ni-containing MMOFs, one of the most favorable strategies is the *in situ* growth of a Ni-MMOF on nickel foam, since in this way, the nickel foam acts as the source of Ni and the resulting MMOF exhibits superior electrocatalytic activity or specific capacitance that is impossible to reach in other synthetic methods. Similar strategies using other metal foams or metal elements are, however, still to be developed, but appear promising in view of the excellent results achieved with Ni foam. In other cases, the metallo-ligand strategy in which a preformed metal complex is used in the MMOF synthesis can be a practical route for certain specific MMOFs due to their well-defined incorporation of suitable complexes acting as linkers. Metallo-ligands in MMOFs can especially introduce some response in the materials, transferring electrons within the structure, particularly in electrocatalytic applications, frequently establishing a synergistic effect with other metals in the structure. In comparison to electrocatalysis, the use of metallo-ligands in MMOFs is much less explored in photocatalysis, although the reported examples already show considerable potential, and it is even less investigated in catalysis. This is somehow unexpected considering that metal complexes have very high catalytic activity as homogeneous catalysts in a variety of reactions. Regarding MMOF-derived materials, thermal treatment causes the collapse of the crystal structure, forming an amorphous structure that nevertheless retains a high specific area, very small particle size, and a large number of attainable active sites. Depending on the atmosphere of the thermal process and the temperature, the organic linker can completely disappear, forming an inorganic solid, like oxides, or can be carbonized, yielding amorphous porous carbon. The loss of the crystal structure is particularly interesting for the use of the resulting derivative in electrocatalysis and as an active material in supercapacitors. Post-modification methods to obtain MMOFs

have been divided into core–shell, insertion, and exchange routes, and all of them are less explored compared to the pre-modification approach and MMOF derivatization, probably due to their higher complexity. It has been found that post-synthesis incorporation of additional metals in a preformed structure can diminish its crystallinity, which can be beneficial or detrimental depending on the application. As a general comment, it seems that post-modification strategies, despite having considerable potential, still require much further attention to overcome their limitations, such as the complexity or high cost of precursors.

This review has described the use of MMOFs and their derivatives for applications related to electrical energy conversion and storage, catalysis, photocatalysis, and sensing. As a general summary, it can be concluded that MMOFs perform better than the corresponding monometallic MOFs due to synergistic effects. Typically, there is an optimum molar ratio of each metal to achieve a balance between the site accessibility and crystallinity of MMOFs and composition that results in higher efficiency, abundance and affordability, and the appropriate redox potentials of the various Ni oxidation states provide efficient electroactive catalytic sites. In addition, Ni establishes synergistic effects with other metal ions, such as Fe and Co, resulting in an increase in faradaic efficiency, including a lower overpotential, smaller Tafel slope, lower energy barrier of the rate-determining step, lower charge resistance, increased double-layer capacitance, and higher turnover frequency. Also, for energy storage applications, Ni-MMOFs are again the most frequently reported systems in the literature due to the high electroactivity of Ni ions and their synergistic effect with Co and Mn, leading to increased specific capacitance. In comparison to energy storage and conversion, the nature of the metals in MMOFs for catalytic applications is wider and more diverse, although the literature is at present dominated by Co, followed by Zn and Cu, as the three most prevalent elements in MMOF structures. Due to the favorable accessibility of a porous structure, a larger number of defects generated almost universally by the native metal and regulation of the electronic properties of the active sites, MMOFs frequently exhibit better catalytic performance than monometallic MOFs, achieving higher conversion and yields in the catalytic reactions. Regarding photocatalysis, MMOFs can also perform better than monometallic analogs by diminishing the bandgap, which results in enhanced light harvesting and regulation of the d-band center to the Fermi level. The most frequently employed metals in MMOF photocatalysts are Ni and Fe, besides heavy metal ions and lanthanides. Lanthanides are by far the most commonly used MMOFs utilized in sensing due to their atomic fluorescence. Incorporation of lanthanides into MMOFs enhances their sensing performance relative to their monometal counterparts, a phenomenon attributed to the synergistic effect between the constituent metals. Besides their use as sensors, Ce-MMOFs are also employed as catalysts and photocatalysts. In terms of other applications, such as removal of pollutants and adsorption, medicine and separation, there are already several reports showing that Fe as a second or third metal can be effective in increasing the performance of the material by either acting as an active site or providing a selective coordination environment. Besides experimental

measurements, further rationalization and deeper understanding of the specific role of each metal in MMOFs is still necessary in general. Also, better control over crystal engineering and a wider toolbox of possible modifications to prepare the required MMOF and derivatives at will are still desired. Enhancing the efficiency of MMOFs by using other metal combinations can lead to optimal performance of these materials for specific applications. Using abundant elements to obtain materials with the highest activity remains a challenge in this area. Also, some drawbacks such as controlling the crystalline structures of MOFs by introduction of multiple metals, providing commensurate metal salt precursors, modulation of the molar ratio, and choosing appropriate content of each metal for higher efficiency, complexity of some synthesis routes, scalability, and stability in some cases can be noticed more in the future for achieving the best performance of MMOFs. Future research in this area should focus not only on synthesizing new MMOFs with optimal molar ratios but also on providing an understanding of the specific role of each metal and the reasons for their synergy, including more *in situ* analysis, analysis that evaluates alterations in electronic structures before and after operation, and theoretical simulations such as DFT.

11. Outlook and future prospects

The synthesis and application of MMOFs and their derivatives is a fast-growing area that has shown the unique performance of these materials as a consequence of the combination of two or more metals, but it currently encounters several limitations and bottlenecks. Further understanding of each metal's role in MMOFs and investigation of the reasons for improved efficiency are mandatory to advance the field. This could provide some guidelines for the selection of the composition of the optimal materials for a given application. Computational modeling must assist in gaining this knowledge and in predicting optimal materials. Novel, general synthesis strategies that could allow the obtainment of the desired MMOF with a good balance between affordability and performance are also needed for future development of the area. Although many studies have shown improved performance in diverse fields of MMOFs compared to single-metal MOFs, the understanding of the role of each metal in applications such as catalysis, energy-related applications, sensing, and pollutant adsorption is still limited. Therefore, investigating the role of metals and the origin of the synergistic effect derived from the combination of transition metals is still necessary and will be extremely important to orient future research toward further performance optimization of MMOFs and derived materials. Modulating band positions in photocatalysts, a change in the stability of MOFs, buttresses catalytic site diversity and activity, which can be achieved by using MMOFs. MMOFs and their derivatives, which can be explored further in the future, can be related to the: (i) MMOFs and their derivatives are less investigated in the applications such as NRR, CO_2RR, electrochemical sensing, and CO_2 hydrogenation, (ii) improving their efficiency and stability *via* various modification from functionalization (such as defect engineering beside mixed-metal) to exchange metals in most applications that have been investigated more, such as OER/

HER, batteries, and supercapacitors *via* emphasize on the role of metal synergy, (iii) using various trend materials and their incorporation with MMOFs such as single-atom catalysis procedures, (iv) increase in conductivity of MMOFs and their derivatives for better electrochemical response and signal-to-noise ratio issues, (v) applying diverse metal-based, and carbon-based materials such as MXene, oxides, graphene, and others to MMOF and their derivations to form MMOF composites and to develop *in situ* analysis beside engineering of materials.

Conflicts of interest

There are no conflicts to declare.

Data availability

Data sharing is not applicable to this article as no new data were generated or analyzed in this work.

Acknowledgements

References

1 S. Kitagawa and M. Kondo, *Bull. Chem. Soc. Jpn.*, 1998, **71**, 1739–1753.

2 H. Li, M. Eddaoudi, M. O'Keeffe and O. M. Yaghi, *Nature*, 1999, **402**, 276–279.

3 A. K. Cheetham, G. Férey and T. Loiseau, *Angew. Chem., Int. Ed.*, 1999, **38**, 3268–3292.

4 H. Ghasempour, F. Zarekarizi and A. Morsali, *CrystEngComm*, 2022, **24**, 4074–4084.

5 R. R. Moslehabadi, Z. Hedayati, M. Mazraeh, S. Asghar, F. Rouhani and A. Morsali, *J. Mater. Chem. B*, 2025, **13**, 7554–7608.

6 X.-W. Yan, A. Hakimifar, F. Bigdeli, Y. Hanifehpour, S.-J. Wang, K.-G. Liu, A. Morsali and S. W. Joo, *Crystals*, 2023, **13**, 1344.

7 D. Ma, B. Li, K. Liu, X. Zhang, W. Zou, Y. Yang, G. Li, Z. Shi and S. Feng, *J. Mater. Chem. A*, 2015, **3**, 23136–23142.

8 Z. Karimzadeh, B. Shokri and A. Morsali, *Appl. Phys. Lett.*, 2023, **123**, 103903.

9 X.-W. Yan, F. Bigdeli, M. Abbasi-Azad, S.-J. Wang and A. Morsali, *Coord. Chem. Rev.*, 2024, **520**, 216126.

10 H. Wang, X. Pei, M. J. Kalmutzki, J. Yang and O. M. Yaghi, *Acc. Chem. Res.*, 2022, **55**, 707–721.

11 F. Afshariazar, A. Morsali, J. Wang and P. C. Junk, *Chem.–Eur. J.*, 2020, **26**, 1355–1362.

12 M. Rubio-Martinez, C. Avci-Camur, A. W. Thornton, I. Imaz, D. Maspoch and M. R. Hill, *Chem. Soc. Rev.*, 2017, **46**, 3453–3480.

13 M. Y. Masoomi, A. Morsali, A. Dhakshinamoorthy and H. Garcia, *Angew. Chem.*, 2019, **131**, 15330–15347.

14 G. Xu, C. Zhu and G. Gao, *Small*, 2022, **18**, 2203140.

15 R. Abazari, S. Sanati and A. Morsali, *Inorg. Chem.*, 2022, **61**, 3396–3405.

16 M. Hu, J. Liu, S. Song, W. Wang, J. Yao, Y. Gong, C. Li, H. Li, Y. Li, X. Yuan, Z. Fang, H. Xu, W. Song and Z. Li, *ACS Catal.*, 2022, **12**, 3238–3248.

17 H. Wang, X. Zhang, X. Wu, Y. Kang, Y. Huang, Z. Zhao, Z. Li, T. Zhou, J. Wang, W. Zhu and C. Pan, *J. Mater. Chem. A*, 2025, **13**, 9952–9962.

18 Q. Qian, P. A. Asinger, M. J. Lee, G. Han, K. Mizrahi Rodriguez, S. Lin, F. M. Benedetti, A. X. Wu, W. S. Chi and Z. P. Smith, *Chem. Rev.*, 2020, **120**, 8161–8266.

19 X.-G. Han, P.-F. Wang, Y.-H. Zhang, H.-Y. Liu, J.-J. Tang, G. Yang and F.-N. Shi, *Inorg. Chim. Acta*, 2022, **536**, 120916.

20 S. Kubendhiran, R.-J. Chung, C. Kongvarhodom, H.-M. Chen, S. Yougbaré, M. Saukani, Y.-F. Wu and L.-Y. Lin, *ACS Appl. Energy Mater.*, 2025, **8**, 6339–6352.

21 H. Shu, T. Lai, J. Ren, X. Cui, X. Tian, Z. Yang, X. Xiao and Y. Wang, *Nanotechnology*, 2022, **33**, 135502.

22 A. M. Rice, G. A. Leith, O. A. Ejegbavwo, E. A. Dolgopolova and N. B. Shustova, *ACS Energy Lett.*, 2019, **4**, 1938–1946.

23 R. E. Sikma, K. S. Butler, D. J. Vogel, J. A. Harvey and D. F. Sava Gallis, *J. Am. Chem. Soc.*, 2024, **146**, 5715–5734.

24 S. Abednatanzi, P. Gohari Derakhshandeh, H. Depauw, F.-X. Coudert, H. Vrielinck, P. Van Der Voort and K. Leus, *Chem. Soc. Rev.*, 2019, **48**, 2535–2565.

25 J. Bitzer and W. Kleist, *Chem.–Eur. J.*, 2019, **25**, 1866–1882.

26 M. Ahmed, *Inorg. Chem. Front.*, 2022, **9**, 3003–3033.

27 L. Chen, H.-F. Wang, C. Li and Q. Xu, *Chem. Sci.*, 2020, **11**, 5369–5403.

28 X. Luo, R. Abazari, M. Tahir, W. K. Fan, A. Kumar, T. Kalhorizadeh, A. M. Kirillov, A. R. Amani-Ghadim, J. Chen and Y. Zhou, *Coord. Chem. Rev.*, 2022, **461**, 214505.

29 R. Rajak, R. Kumar, S. N. Ansari, M. Saraf and S. M. Mobin, *Dalton Trans.*, 2020, **49**, 11792–11818.

30 S. Sanati, R. Abazari, J. Albero, A. Morsali, H. García, Z. Liang and R. Zou, *Angew. Chem., Int. Ed.*, 2021, **60**, 11048–11067.

31 J.-E. Zhou, J. Chen, Y. Peng, Y. Zheng, A. Zeb and X. Lin, *Coord. Chem. Rev.*, 2022, **472**, 214781.

32 Q. Liang, J. Chen, F. Wang and Y. Li, *Coord. Chem. Rev.*, 2020, **424**, 213488.

33 X. Qin, D. Kim and Y. Piao, *Carbon Energy*, 2021, **3**, 66–100.

34 J. Du, F. Li and L. Sun, *Chem. Soc. Rev.*, 2021, **50**, 2663–2695.

35 S. Sanati, A. Morsali and H. García, *Energy Environ. Sci.*, 2022, **15**, 3119–3151.

36 J. Ji, W. Lou and P. Shen, *Int. J. Hydrogen Energy*, 2022, **47**, 39443–39469.

37 D. H. Taffa, D. Balkenhohl, M. Amiri and M. Wark, *Small Struct.*, 2023, **4**, 2200263.

38 S. Navalón, A. Dhakshinamoorthy, M. Álvaro, B. Ferrer and H. García, *Chem. Rev.*, 2023, **123**, 445–490.

39 R. Jaryal, R. Kumar and S. Khullar, *Coord. Chem. Rev.*, 2022, **464**, 214542.

40 C. Zhang, Q. Liu, P. Wang, J. Zhu, D. Chen, Y. Yang, Y. Zhao, Z. Pu and S. Mu, *Small*, 2021, **17**, 2104241.

41 Y. Li, Y. Xu, W. Yang, W. Shen, H. Xue and H. Pang, *Small*, 2018, **14**, 1704435.

42 H. Wu, X. Li, S. Huai, S. Zhang, W. Ruan, X. Huang, C. Cheng, M. Qu, P. Li and X. Yu, *J. Mater. Chem. A*, 2025, **13**, 30324–30337.

43 M. Cui, B. Xu, X. Shi, Q. Zhai, Y. Dou, G. Li, Z. Bai, Y. Ding, W. Sun, H. Liu and S. Dou, *J. Mater. Chem. A*, 2024, **12**, 18921–18947.

44 M. S. Khan, Y. Li, D.-S. Li, J. Qiu, X. Xu and H. Y. Yang, *Nanoscale Adv.*, 2023, **5**, 6318–6348.

45 Z. Qian, R. Zhang, Y. Xiao, H. Huang, Y. Sun, Y. Chen, T. Ma and X. Sun, *Adv. Energy Mater.*, 2023, **13**, 2300086.

46 S.-H. Guo, X.-J. Qi, H.-M. Zhou, J. Zhou, X.-H. Wang, M. Dong, X. Zhao, C.-Y. Sun, X.-L. Wang and Z.-M. Su, *J. Mater. Chem. A*, 2020, **8**, 11712–11718.

47 J. Wang, S. Zhang, Y. Han, L. Zhang, Q. Wang, G. Wang and X. Zhang, *Mol. Catal.*, 2022, **532**, 112741.

48 H. Dong, X. Zhang, X.-C. Yan, Y.-X. Wang, X. Sun, G. Zhang, Y. Feng and F.-M. Zhang, *ACS Appl. Mater. Interfaces*, 2019, **11**, 45080–45086.

49 N. K. Chaudhari, H. Jin, B. Kim and K. Lee, *Nanoscale*, 2017, **9**, 12231–12247.

50 S. Mao, L. Ye, S. Jin, C. Zhou, J. Pang and W. Xu, *Inorg. Chem.*, 2024, **63**, 6005–6015.

51 J. Ding, D. Guo, N. Wang, H.-F. Wang, X. Yang, K. Shen, L. Chen and Y. Li, *Angew. Chem., Int. Ed.*, 2023, **62**, e202311909.

52 Y. Li, M. Lu, Y. Wu, H. Xu, J. Gao and J. Yao, *Adv. Mater. Interfaces*, 2019, **6**, 1900290.

53 R. Bhosale, S. Bhosale, V. Chavan, C. Jambhale, D.-k. Kim and S. Kolekar, *ACS Appl. Nano Mater.*, 2024, **7**, 2244–2257.

54 M. R. Tamtam, G. S. Choi, S. P. Kumar Vangala, J. Shim, N. N. Nguyen and N. N. Dang, *J. Phys. Chem. Lett.*, 2025, **16**, 10655–10668.

55 S. Khan, T. Noor, N. Iqbal and E. Pervaiz, *ChemNanoMat*, 2022, **8**, e202200115.

56 Y. Peng, S. Sanati, A. Morsali and H. García, *Angew. Chem., Int. Ed.*, 2023, **62**, e202214707.

57 Y. Liu, S. Wang, Z. Li, H. Chu and W. Zhou, *Coord. Chem. Rev.*, 2023, **484**, 215117.

58 M. Z. Iqbal, U. Aziz, S. Aftab and H. H. Hegazy, *Int. J. Hydrogen Energy*, 2023, **48**, 17801–17826.

59 C. Li, Y. Liu, L. Guan, K. Li, G. Wang and Y. Lin, *Chem. Eng. J.*, 2020, **400**, 125884.

60 W. Zhou, Z. Xue, Q. Liu, Y. Li, J. Hu and G. Li, *ChemSusChem*, 2020, **13**, 5647–5653.

61 Y. Xu, Q. Zhou, T. Liu, T. Ren, H. Yu, K. Deng, Z. Wang, L. Wang and H. Wang, *Chem. Commun.*, 2023, **59**, 7623–7626.

62 A. Abdelhafiz, M. H. Mohammed, J. Abed, D.-C. Lee, M. Chen, A. S. Helal, Z. Ren, F. Alamgir, E. Sargent, P. A. Kohl, S. K. Elsaidi and J. Li, *Adv. Energy Mater.*, 2024, **14**, 2303350.

63 C. Zhang, R. Lu, C. Liu, J. Lu, Y. Zou, L. Yuan, J. Wang, G. Wang, Y. Zhao and C. Yu, *Adv. Sci.*, 2022, **9**, 2104768.

64 H. Wang, J. Bai, Q. He, Y. Liao, S. Wang and L. Chen, *J. Colloid Interface Sci.*, 2024, **665**, 172–180.

65 F. Ismail, A. Abdellah, V. Sudheeshkumar, A. Rakhsha, W. Chen, N. Chen and D. C. Higgins, *ACS Appl. Energy Mater.*, 2022, **5**, 9408–9417.

66 S. L. Fereja, Z. Zhang, Z. Fang, J. Guo, X. Zhang, K. Liu, Z. Li and W. Chen, *ACS Appl. Mater. Interfaces*, 2022, **14**, 38727–38738.

67 R. Abazari, S. Sanati, P. Stelmachowski, Q. Wang, A. Krawczuk, J. Goscianska and M. Liu, *Inorg. Chem.*, 2024, **63**, 5642–5651.

68 L. Wen, X. Li, R. Zhang, H. Liang, Q. Zhang, C. Su and Y.-J. Zeng, *ACS Appl. Mater. Interfaces*, 2021, **13**, 14181–14188.

69 X. Wang, G. Zhang, W. Yin, S. Zheng, Q. Kong, J. Tian and H. Pang, *Carbon Energy*, 2022, **4**, 246–281.

70 J. Wang, J. Liang, Y. Lin, K. Shao, X. Chang, L. Qian, Z. Li and P. Hu, *Chem. Eng. J.*, 2022, **446**, 137368.

71 T.-L. Wu, X.-N. Tan, T.-T. Nong, Y.-J. Pan, P.-F. Qiu, J.-Q. He, Y. Zhou, X.-C. Tan, Z.-Y. Huang and L. Han, *Chem. Eng. J.*, 2023, **457**, 141238.

72 H. Jiang, J. Xian, R. Hu, S. Mi, L. Wei, G. Fang, Z. Wu, S. Xu, M. Fan, K. Liu, H. Yu, W. Xu and J. Wan, *Chem. Eng. J.*, 2023, **455**, 140804.

73 L.-J. Ma, C.-Y. Luo, R.-N. Wang, Y.-C. Tan, J.-L. Hou and Q.-Y. Zhu, *ACS Energy Lett.*, 2023, **8**, 4427–4437.

74 K.-B. Wang, R. Bi, Z.-K. Wang, Y. Chu and H. Wu, *New J. Chem.*, 2020, **44**, 3147–3167.

75 Y. Chen, W. Du, B. Dou, J. Chen, L. Hu, A. Zeb and X. Lin, *CrystEngComm*, 2022, **24**, 2729–2743.

76 T. Zhao, H. Wu, X. Wen, J. Zhang, H. Tang, Y. Deng, S. Liao and X. Tian, *Coord. Chem. Rev.*, 2022, **468**, 214642.

77 C. Vallés-García, E. Gkaniatsou, A. Santiago-Portillo, M. Giménez-Marqués, M. Álvaro, J.-M. Greneche, N. Steunou, C. Sicard, S. Navalón, C. Serre and H. García, *J. Mater. Chem. A*, 2020, **8**, 17002–17011.

78 N. Antil, M. Chauhan, N. Akhtar, R. Newar, W. Begum, J. Malik and K. Manna, *ACS Catal.*, 2022, **12**, 11159–11168.

79 C. Chen, X. Ji, Y. Xiong and J. Jiang, *Chem. Eng. J.*, 2024, **481**, 148555.

80 S. Li, J. Tan, Z. Jiang, J. Wang and Z. Li, *Chem. Eng. J.*, 2020, **384**, 123354.

81 S.-C. Fan, S.-Q. Chen, J.-W. Wang, Y.-P. Li, P. Zhang, Y. Wang, W. Yuan and Q.-G. Zhai, *Inorg. Chem.*, 2022, **61**, 14131–14139.

82 J.-M. Li, Q.-C. Lin, N. Li, Z.-H. Li, G. Tan, S.-J. Liu, L.-H. Chung, W.-M. Liao, L. Yu and J. He, *Adv. Funct. Mater.*, 2023, **33**, 2210717.

83 Y. Yang, X. Hu, G. Wang, J. Han, Q. Zhang, W. Liu, Z. Xie and Z. Zhou, *Adv. Funct. Mater.*, 2024, **34**, 2315354.

84 W. Wang, B. Ibarlucea, C. Huang, R. Dong, M. Al Aiti, S. Huang and G. Cuniberti, *Nanoscale Horiz.*, 2024, **9**, 1432–1474.

85 P. Mhettar, N. Kale, J. Pantwalawalkar, S. Nangare and N. Jadhav, *ADMET and DMPK*, 2024, **12**, 27–62.

86 A. Wang, M. Walden, R. Ettlinger, F. Kiessling, J. J. Gassensmith, T. Lammers, S. Wuttke and Q. Peña, *Adv. Funct. Mater.*, 2024, **34**, 2308589.

87 F. Zadehahmadi, N. T. Eden, H. Mahdavi, K. Konstas, J. I. Mardel, M. Shaibani, P. C. Banerjee and M. R. Hill, *Environ. Sci.:Water Res. Technol.*, 2023, **9**, 1305–1330.

88 Q. Xia, H. Wang, B. Huang, X. Yuan, J. Zhang, J. Zhang, L. Jiang, T. Xiong and G. Zeng, *Small*, 2019, **15**, 1803088.

89 X. Liu, T. Liang, R. Zhang, Q. Ding, S. Wu, C. Li, Y. Lin, Y. Ye, Z. Zhong and M. Zhou, *ACS Appl. Mater. Interfaces*, 2021, **13**, 9643–9655.

90 S. Zhang, Y. Zhang, F. Baig and T.-F. Liu, *Cryst. Growth Des.*, 2021, **21**, 3100–3122.

91 M. Al Haydar, H. R. Abid, B. Sunderland and S. Wang, *Drug Des., Dev. Ther.*, 2018, 23–35.

92 Z. Mu, S. Wu, J. Guo, M. Zhao and Y. Wang, *ACS Sustain. Chem. Eng.*, 2022, **10**, 2984–2993.

93 S. Kulandaivel, Y.-K. Lu, C.-H. Lin and Y.-C. Yeh, *J. Mater. Chem. B*, 2025, **13**, 151–159.

94 Z. Deng, J. Cao, L. Zhao, Z. Zhang and J. Yuan, *Molecules*, 2024, **29**, 3739.

95 D. Zhao, W. Jiang, W. Zhang, C. Zhang, W. Zhao, Z. Chen, Y. Liu and J. Xu, *Chem. Mater.*, 2025, **37**, 4853–4867.

96 C. Ding, W. Zhong, Y. Cao, T. Ma, H. Ye, Z. Fang, Y. Feng, S. Zhao, J. Yang, Y. Li, L. Shen and W. He, *Chem. Eng. Sci.*, 2025, **302**, 120888.

97 M. Burud, S. A. Patil, V. Jadhav, P. Chougale, S. Mane-Gavade, R. Ustad, J. Shen, A. Supale, S. Sabale and D.-K. Kim, *Energy Fuels*, 2025, **39**, 13648–13657.

98 R. Li, J. Wang, B. Guo, J. Zhang, Y. Sun, J. Wang, H. Zhang, W. Li and X. Feng, *J. Alloys Compd.*, 2025, **1036**, 181892.

99 G. Arunkumar, G. Deviga, M. Mariappan, M. Pannipara, A. G. Al-Sehemi and S. P. Anthony, *Dalton Trans.*, 2025, **54**, 4225–4233.

100 X. Hou, Z. Han, X. Xu, D. Sarker, J. Zhou, M. Wu, Z. Liu, M. Huang and H. Jiang, *Chem. Eng. J.*, 2021, **418**, 129330.

101 H. Xu, C. Shan, X. Wu, M. Sun, B. Huang, Y. Tang and C.-H. Yan, *Energy Environ. Sci.*, 2020, **13**, 2949–2956.

102 W. Zhang, M. Niu, J. Yu, S. Li, Y. Wang and K. Zhou, *Adv. Funct. Mater.*, 2023, **33**, 2302014.

103 Y. Kong, D. Xiong, C. Lu, J. Wang, T. Liu, S. Ying, X. Ma and F.-Y. Yi, *ACS Appl. Mater. Interfaces*, 2022, **14**, 37804–37813.

104 Y. Xie, F. Le, X. Yang, W. Shu, R. Sheng, A. Liu and W. Jia, *Dalton Trans.*, 2025, **54**, 10907–10915.

105 B. Yan, D. Wang, W. Ji and Y. Fu, *J. Mater. Chem. C*, 2025, **13**, 11756–11763.

106 Y. Zhao, J. Ma, J. Yin, H. Han, X. Zhang, Y. Cao and W. Cai, *Appl. Surf. Sci.*, 2024, **657**, 159783.

107 Y. Han, J. Wang, X. Yan, D. Wang, H. Han and C. Sun, *J. Hazard. Mater.*, 2025, **499**, 140196.

108 H. Ghasempour, F. Zarekarizi, B. Habibi, G. Zhang, A. Ramazani and A. Morsali, *CrystEngComm*, 2025, **27**, 4826–4834.

109 H. Feng, Q. Xu, T. Lv and H. Liu, *Appl. Catal. B Environ. Energy*, 2024, **351**, 123949.

110 Y. Zhu, Q. Dong, A. Sial, A. Labidi, K. Zhao, X. Li, J. Wang and C. Wang, *Appl. Catal. O: Open*, 2025, **200**, 207030.

111 X. Zhong, J. Xu and S. Song, *Appl. Surf. Sci.*, 2025, **690**, 162659.

112 S. Adak, R. Ghosh Chaudhuri and M. K. Mandal, *Appl. Organomet. Chem.*, 2025, **39**, e70412.

113 Z. Yin, J. Liang, Z. Zhang, H. Luo and J. Zhou, *J. Colloid Interface Sci.*, 2022, **623**, 405–416.

114 L. Karuppasamy, L. Gurusamy, S. Ananan, S. C. Barton, C.-H. Liu and J. J. Wu, *Electrochim. Acta*, 2023, **449**, 142242.

115 C. Feng, Q. An, Q. Zhang, L. Huang, N. Wang, X. Zhang, Y. Xu, M. Xie, R. Wang, Y. Jiao and J. Chen, *Int. J. Hydrogen Energy*, 2024, **55**, 189–198.

116 Q. Zhai, M. Zhang, H. Ji, H. Bian, H. Wu, Y. Ma, Y. Yang, S. Tang, M. Cui and X. Meng, *J. Phys. Chem. C*, 2022, **126**, 20204–20212.

117 Q. Wang, X. Ma, P. Ma, R. Bi and S. Song, *ACS Appl. Nano Mater.*, 2023, **6**, 9339–9350.

118 W. Ke, Y. Zhang, A. L. Imbault and Y. Li, *Int. J. Hydrogen Energy*, 2021, **46**, 20941–20949.

119 W.-D. Zhang, H. Yu, T. Li, Q.-T. Hu, Y. Gong, D.-Y. Zhang, Y. Liu, Q.-T. Fu, H.-Y. Zhu, X. Yan and Z.-G. Gu, *Appl. Catal., B*, 2020, **264**, 118532.

120 C. Chen, Y. Tuo, Q. Lu, H. Lu, S. Zhang, Y. Zhou, J. Zhang, Z. Liu, Z. Kang, X. Feng and D. Chen, *Appl. Catal., B*, 2021, **287**, 119953.

121 Y. Zhang, Z. Li, K. Zhang, Z. Wu, F. Gao and Y. Du, *Appl. Surf. Sci.*, 2022, **590**, 153102.

122 W. Dong, N. Huang, Y. Zhao, Y. Feng, G. Zhao, S. Ran and W. Liu, *J. Electroanal. Chem.*, 2024, **959**, 118184.

123 D. Senthil Raja, C.-L. Huang, Y.-A. Chen, Y. Choi and S.-Y. Lu, *Appl. Catal., B*, 2020, **279**, 119375.

124 D. Xing, H. Wang, Z. Cui, L. Lin, Y. Liu, Y. Dai and B. Huang, *J. Colloid Interface Sci.*, 2024, **656**, 309–319.

125 I. W. P. Chen, W.-Y. Chen and T. Y. Liu, *Mater. Today Chem.*, 2024, **35**, 101873.

126 X.-N. Lv, Y.-H. Zhang, P.-P. Sun, P.-F. Wang, J.-J. Tang, G. Yang, Q. Shi and F.-N. Shi, *J. Solid State Chem.*, 2022, **306**, 122786.

127 W. Sun, S. Chen and Y. Wang, *Dalton Trans.*, 2019, **48**, 2019–2027.

128 L. Fan, X. Guo, W. Li, X. Hang and H. Pang, *Chin. Chem. Lett.*, 2023, **34**, 107447.

129 S. Ebrahimi-Koodehi, F. E. Ghodsi and J. Mazloom, *Int. J. Energy Res.*, 2022, **46**, 24368–24380.

130 C. Xu, M. Bao, J. Ren and Z. Zhang, *RSC Adv.*, 2020, **10**, 39080–39086.

131 H.-T. T. Nguyen, K.-N. T. Tran, L. Van Tan, V. A. Tran, V.-D. Doan, T. Lee and T. D. Nguyen, *Mater. Chem. Phys.*, 2021, **272**, 125040.

132 L. Gu, G. Deng, R. Huang and X. Shi, *Nanoscale*, 2022, **14**, 15821–15831.

133 Y. Zhang, R. Huang, Y. Fang, J. Wang, Z. Yuan, X. Chen, W. Zhu, Y. Cai and X. Shi, *Sep. Purif. Technol.*, 2024, **336**, 126164.

134 C. Li, H. Yu, S. Guo, J. Jia, Y. Chang, M. Jia and J. Wang, *New J. Chem.*, 2024, **48**, 3364–3369.

135 Q. Liu, J.-Y. Tan, J.-Y. Zhang, N. Zhang and Z.-J. Liu, *Microporous Mesoporous Mater.*, 2021, **310**, 110626.

136 Y. Hu, J. Zhang, H. Huo, Z. Wang, X. Xu, Y. Yang, K. Lin and R. Fan, *Catal. Sci. Technol.*, 2020, **10**, 315–322.

137 O. K. T. Nguyen, L. X. Nong, V. H. Nguyen and T. D. Nguyen, *ChemistrySelect*, 2023, **8**, e202302598.

138 D. Zeng, G. Zhu and C. Xia, *Fuel Process. Technol.*, 2022, **235**, 107374.

139 Y. Li, G. Zhao, B. An, K. Xu, D. Wu, X. Ren, H. Ma, X. Liu, R. Feng and Q. Wei, *Anal. Chem.*, 2024, **96**, 4067–4075.

140 A. Yousaf, Z. Zhao, L. Wu, S. Hanif and N. Akhtar, *Process Saf. Environ. Prot.*, 2024, **191**, 102–111.

141 P. Yuan, Z. Deng, P. Qiu, Z. Yin, Y. Bai, Z. Su and J. He, *Food Control*, 2023, **144**, 109357.

142 H.-R. Zhang, X.-H. Ren, D.-W. Wang, X.-W. He, W.-Y. Li and Y.-K. Zhang, *Talanta*, 2023, **259**, 124506.

143 C. Duan and J. Zheng, *J. Electrochem. Soc.*, 2019, **166**, B942.

144 F. T. Alshorifi, S. M. El Dafrawy and A. I. Ahmed, *ACS Omega*, 2022, 7, 23421–23444.

145 W. A. El-Yazeed, Y. Abou El-Reash, L. Elatwy and A. I. Ahmed, *RSC Adv.*, 2020, **10**, 9693–9703.

146 Z. Zhang, J. Liu, Z. Wang and J. Zhang, *Ind. Eng. Chem. Res.*, 2020, **60**, 781–789.

147 Q. Guo, X.-P. Ma, L.-W. Zheng, C.-X. Zhao, X.-Y. Wei, Y. Xu, Y. Li, J.-J. Xie, K.-G. Zhang and C.-G. Yuan, *Ecotoxicol. Environ. Saf.*, 2022, **245**, 114097.

148 W. A. El-Yazeed, Y. Abou El-Reash, L. Elatwy and A. I. Ahmed, *J. Taiwan Inst. Chem. Eng.*, 2020, **114**, 199–210.

149 Z. Garazhian, A. Farrokhi, A. Rezaeifard, M. Jafarpour and R. Khani, *RSC Adv.*, 2021, **11**, 21127–21136.

150 J. Yao, Z. Zhao, L. Yu, J. Huang, S. Shen, S. Zhao, Y. Wu, X. Tian, J. Wang and Q. Xia, *J. Mater. Chem. A*, 2023, **11**, 14728–14737.

151 Q. Wu, M. S. Siddique and W. Yu, *J. Hazard. Mater.*, 2021, **401**, 123261.

152 R. Liu, W. Zhang, Y. Chen and Y. Wang, *Colloids Surf., A*, 2020, **587**, 124334.

153 X. Liu, H. Yang, Y. Diao, Q. He, C. Lu, A. Singh, A. Kumar, J. Liu and Q. Lan, *Chemosphere*, 2022, **307**, 135729.

154 A. Helal, S. Shaheen Shah, M. Usman, M. Y. Khan, M. A. Aziz and M. Mizanur Rahman, *Chem. Rec.*, 2022, **22**, e202200055.

155 X. Zha, W. Yang, L. Shi, Y. Li, Q. Zeng, J. Xu and Y. Yang, *ACS Appl. Mater. Interfaces*, 2022, **14**, 37843–37852.

156 G. Li, Y. Liu, Y. Shen, Q. Fang and F. Liu, *Front. Chem. Eng.*, 2021, **3**, 636439.

157 C. Lin, X. Guo, L. Chen, T. You, J. Lu and D. Sun, *J. Colloid Interface Sci.*, 2022, **628**, 731–744.

158 X. Han, W. Yang, C. Yin, X. Zhang, C. Yi and Z. Fan, *Appl. Surf. Sci.*, 2025, **679**, 160964.

159 Y. Yao, K. Wei, S. Zhao, H. Zhou, B. Kui, G. Zhu, W. Wang, P. Gao and W. Ye, *ACS Sustain. Chem. Eng.*, 2025, **13**, 1245–1252.

160 Y. Wang, L. Fu, J. Wu, F. Yang and L. Feng, *ChemSusChem*, 2025, **18**, e202401580.

161 X. Sun, L. Yang, D. Li and Z. Tian, *J. Mol. Struct.*, 2025, **1322**, 140549.

162 Z.-H. Pu, S.-E. Yu, C.-C. Hsu, I. C. Ni, C.-I. Wu, N. Devi, C.-X. Liu, Y.-S. Chen, I. C. Cheng and J.-Z. Chen, *Int. J. Hydrogen Energy*, 2025, **113**, 429–440.

163 R. Pavadai, M. Arivazhagan, S. Prabu, S. Ingavale, G. Honnu, V. M. Gowri, S. Thongmee, C. Issro, D. Khamboonrueang and S. Kityakarn, *Mater. Chem. Phys.*, 2025, **345**, 131245.

164 W.-S. Liu, X. Hu, K. Zeng, C.-H. Ji, H. Feng, Y.-G. Zhou and Q.-Y. Cai, *J. Mater. Chem. A*, 2025, **13**, 3174–3184.

165 Sonadia, Z. Iqbal, W. Miran, A. Ul-Hamid, K. S. Ayub and F. Azad, *Energy Fuels*, 2024, **38**, 5397–5406.

166 M. Ding, J. Chen, M. Jiang, X. Zhang and G. Wang, *J. Mater. Chem. A*, 2019, **7**, 14163–14168.

167 Z.-Y. Zhao, X. Sun, H. Gu, Z. Niu, P. Braunstein and J.-P. Lang, *ACS Appl. Mater. Interfaces*, 2022, **14**, 15133–15140.

168 L. Zhao, J. Yan, H. Huang, X. Du, H. Chen, X. He, W. Li, W. Fang, D. Wang, X. Zeng, J. Dong and Y. Liu, *Adv. Funct. Mater.*, 2024, **34**, 2310902.

169 K. Yue, J. Liu, Y. Zhu, C. Xia, P. Wang, J. Zhang, Y. Kong, X. Wang, Y. Yan and B. Y. Xia, *Energy Environ. Sci.*, 2021, **14**, 6546–6553.

170 J. Hou, N. Chen, D. Bi, Z. Liu and Y. Liang, *Int. J. Hydrogen Energy*, 2025, **101**, 1070–1076.

171 S. Xu, M. Li, H. Wang, Y. Sun, W. Liu, J. Duan and S. Chen, *J. Phys. Chem. C*, 2022, **126**, 14094–14102.

172 M. Fang, X. Gao, J. Liang, B. Guo, L. Zou, J. Lu, Y. Gao, E. C. M. Tse and J. Liu, *J. Mater. Chem. A*, 2022, **10**, 7013–7019.

173 Y. Sun, Z. Xue, Q. Liu, Y. Jia, Y. Li, K. Liu, Y. Lin, M. Liu, G. Li and C.-Y. Su, *Nat. Commun.*, 2021, **12**, 1369.

174 M. Li, H. Sun, J. Yang, M. Humayun, L. Li, X. Xu, X. Xue, A. Habibi-Yangjeh, K. Temst and C. Wang, *Chem. Eng. J.*, 2022, **430**, 132733.

175 Y. Xu, Y. Xia, S. Fan, W. Gao, Z. Gao and C. Wang, *Small*, 2025, e08771.

176 J. Hu, A. Rendón-Patiño, I. S. Khan, L. Garzon-Tovar, D. Mateo, J. Albero, J. Gascon and H. García, *J. Energy Storage*, 2025, **108**, 114990.

177 N. Kumar, P. Bhattacharya, A. Jana and S. Kumar, *Inorg. Chem. Commun.*, 2025, **177**, 114445.

178 X. Wang, C. Hao, J. Zhang, C. Ni, X. Wang and Y. Shen, *J. Power Sources*, 2022, **539**, 231594.

179 A. Umar, S. Alam, N. u. Rehman, M. Zahoor, R. Ullah, E. A. Ali and M. N. Umar, *Inorg. Chem. Commun.*, 2025, **180**, 114942.

180 G. Karthikeyan, S. Mohan, P. M. Austeria and R. G. Balakrishna, *Small*, 2025, **21**, 2409133.

181 M. Zhao, H. Li, W. Li, J. Li, L. Yi, W. Hu and C. M. Li, *Chem.– Eur. J.*, 2020, **26**, 17091–17096.

182 M. Manivannan, V. Rajagopal, L. Krishnamoorthy, S. Dhanasurya, V. Suryanarayanan, M. Kathiresan, T. Raju and L. A. Jones, *New J. Chem.*, 2023, **47**, 6330–6341.

183 J. Yin, C. Wang, J. Li, S. Yu, Z. Wu, Y. Zhang and Y. Du, *Inorg. Chem.*, 2024, **63**, 5167–5174.

184 M. Zhang, W. Xu, T. Li, H. Zhu and Y. Zheng, *Inorg. Chem.*, 2020, **59**, 15467–15477.

185 Q. Mou, Z. Xu, W. Zuo, T. Shi, E. Li, G. Cheng, X. Liu, H. Zheng, H. Li and P. Zhao, *Mater. Chem. Front.*, 2022, **6**, 2750–2759.

186 S. Xu, Q. Huang, J. Xue, Y. Yang, L. Mao, S. Huang and J. Qian, *Inorg. Chem.*, 2022, **61**, 8909–8919.

187 H. Zhao, L. Zhang, L. Dai, F. Yao, Y. Huang, J. Deng, Y. Fu, J. Zhu and J. Sun, *Appl. Surf. Sci.*, 2022, **592**, 153252.

188 Q. Qian, Y. Li, Y. Liu, L. Yu and G. Zhang, *Adv. Mater.*, 2019, **31**, 1901139.

189 Z. Li, S. Deng, H. Yu, Z. Yin, S. Qi, L. Yang, J. Lv, Z. Sun and M. Zhang, *J. Mater. Chem. A*, 2022, **10**, 4230–4241.

190 Q. Liang, Y. Liu, Z. Xue, Z. Zhao, G. Li and J. Hu, *Chem. Commun.*, 2022, **58**, 6966–6969.

191 S. Li, Z. Wang, T. Wang, Y. Yang, Y. Xiao, Y. Tian, H. Zhu, X. Jing and G. Zhu, *Chem.–Eur. J.*, 2023, **29**, e202301129.

192 H. Xu, C. Wang, G. He and H. Chen, *Dalton Trans.*, 2023, **52**, 8466–8472.

193 Y. Zhang, Y. Mo, S. Wang, H. Zhong, Z. Cao and X. Ma, *Colloids Surf., A*, 2022, **642**, 128469.

194 Q. Li, Y. Liu, S. Niu, C. Li, C. Chen, Q. Liu and J. Huo, *J. Colloid Interface Sci.*, 2021, **603**, 148–156.

195 D. Liu, H. Xu, C. Wang, H. Shang, R. Yu, Y. Wang, J. Li, X. Li and Y. Du, *Inorg. Chem.*, 2021, **60**, 5882–5889.

196 S. Niu, C. Li, J. Huo, W. Dong, S. El Hankari, Y. Liang and Q. Li, *ACS Omega*, 2021, **6**, 13946–13952.

197 T. Liu, Y. Zhang, C. Ye, D. Wang, C. Wang and Y. Du, *J. Colloid Interface Sci.*, 2024, **655**, 466–473.

198 W. Li, H. Zhang, K. Zhang, Z. Cheng, H. Chen, G. Tan, X. Feng, L. Wang and S. Mu, *Chem. Commun.*, 2023, **59**, 4750–4753.

199 M. Rinawati, Y.-X. Wang, K.-Y. Chen and M.-H. Yeh, *Chem. Eng. J.*, 2021, **423**, 130204.

200 K. Karuppasamy, R. Bose, D. B. Velusamy, D. Vikraman, P. Santhoshkumar, P. Sivakumar, A. Alfantazi and H.-S. Kim, *ACS Sustain. Chem. Eng.*, 2022, **10**, 14693–14704.

201 K. Srinivas, F. Ma, Y. Liu, Z. Zhang, Y. Wu and Y. Chen, *ACS Appl. Mater. Interfaces*, 2022, **14**, 52927–52939.

202 J. Ma, B. Lu, S. Wang, W. He, X. Bai, T. Wang, X. Zhang, Y. Li, L. Zhang, J. Chen, F. Meng and Y. Fu, *New J. Chem.*, 2020, **44**, 2459–2464.

203 Y. Du, M. Zhang, Z. Wang, Y. Liu, Y. Liu, Y. Geng and L. Wang, *J. Mater. Chem. A*, 2019, **7**, 8602–8608.

204 E. Sadeghi, S. Chamani, I. D. Yildirim, E. Erdem, N. S. Peighambardoust and U. Aydemir, *ACS Appl. Mater. Interfaces*, 2024, **16**, 10078–10092.

205 T. Chen, C. Lu, J. Wang, Y. Kong, T. Liu, S. Ying, X. Ma and F.-Y. Yi, *Electrochim. Acta*, 2024, **480**, 143927.

206 Z. Gao, Y. Wang, L. Xu, Q. Tao, X. Wang, Z. Zhou, Y. Luo, J. Yu and Y. Huang, *Chem. Eng. J.*, 2022, **433**, 133515.

207 S. Gopi, S. Perumal, E. M. Al Olayan, O. D. AlAmri, A. S. Aloufi, M. Kathiresan and K. Yun, *Chemosphere*, 2021, **267**, 129243.

208 D.-X. Yang, P.-F. Wang, H.-Y. Liu, Y.-H. Zhang, P.-P. Sun and F.-N. Shi, *J. Solid State Chem.*, 2022, **309**, 122947.

209 J. Lin, C. Xu, M. Lu, X. Lin, Z. Ali, C. Zeng, X. Xu and Y. Luo, *Energy Environ. Mater.*, 2023, **6**, e12284.

210 Y. Chen, X. Hu, X. Chen, J.-H. Liu, Y. Huang and D. Cao, *Chem. Eng. J.*, 2023, **478**, 147411.

211 H.-y. Chen, Y.-q. Huo, K.-z. Cai and Y. Teng, *Synth. Met.*, 2021, **276**, 116761.

212 X. Hang, B. Liu, G. Yuan, X. Wang, Y. An and H. Pang, *Mater. Today Chem.*, 2023, **34**, 101754.

213 Y. Xie, H. Zhang, K. Zhang, R. Liu, Y. Sun, X. Gao, H. Bai, F. Yao and H. Yue, *Electrochim. Acta*, 2024, **477**, 143784.

214 Y. Zhu, Z. Tao, C. Cai, Y. Tan, A. Wang and Y. Yang, *Inorg. Chem. Commun.*, 2022, **139**, 109391.

215 B. Zhang, S. Song, W. Li, L. Zheng and X. Ma, *Ionics*, 2021, **27**, 3553–3566.

216 M. R. Abdul Karim, W. Khalid and R. Zahid, *Energy Technol.*, 2024, **12**, 2301160.

217 R. Zahid, M. R. Abdul Karim, W. Khalid and M. A. Marwat, *Energy Technol.*, 2024, **12**, 2300883.

218 M. Abedi, G. Mahmoudi, P. Hayati, B. Machura, F. I. Zubkov, K. Mohammadi, S. Bahrami, H. Derikvandi, Z. Mehrabadi and A. M. Kirillov, *New J. Chem.*, 2019, **43**, 17457–17465.

219 D. Wang, M. Suo, S. Lai, L. Deng, J. Liu, J. Yang, S. Chen, M.-F. Wu and J.-P. Zou, *Appl. Catal., B*, 2023, **321**, 122054.

220 Z. Song, R. Li, D. Wen, J. Pei, H. Zhu and S. Ruan, *ACS Mater. Lett.*, 2023, **5**, 473–479.

221 B. Wang, Y. Luo, L. Gao, B. Liu and G. Duan, *Biosens. Bioelectron.:X*, 2021, **171**, 112736.

222 Y. Yang, J.-L. Zhang, W.-B. Liang, J.-L. Zhang, X.-L. Xu, Y.-J. Zhang, R. Yuan and D.-R. Xiao, *Sens. Actuators, B*, 2022, **362**, 131802.

223 Z. Xu, Q. Wang, H. Zhangsun, S. Zhao, Y. Zhao and L. Wang, *Food Chem.*, 2021, **349**, 129202.

224 W. Li, S. Lv, Y. Wang, L. Zhang and X. Cui, *Sens. Actuators, B*, 2019, **281**, 652–658.

225 Y. Ma, P. Wei, M. Chen, X. Shi, X. Lu, X. Zhang and D. Sun, *J. Electroanal. Chem.*, 2023, **940**, 117490.

226 F. M. Jais, S. Ibrahim, C. Y. Chee and Z. Ismail, *J. Environ. Chem. Eng.*, 2021, **9**, 106367.

227 G.-R. Si, W. Wu, T. He, Z.-C. Xu, K. Wang and J.-R. Li, *ACS Mater. Lett.*, 2022, **4**, 1032–1036.

228 J. Ma, W. Bai, X. Liu and J. Zheng, *Microchim. Acta*, 2022, **189**, 20.

229 X. Shi, R. Hua, Y. Xu, T. Liu and G. Lu, *Sustainable Energy Fuels*, 2020, **4**, 4589–4597.

230 T. Zhang, H. Chen, L. Wang, Y. Liang and X. Zhang, *ACS Appl. Nano Mater.*, 2022, **5**, 15220–15227.

231 E. Raphael Ezeigwe, L. Dong, J. Wang, L. Wang, W. Yan and J. Zhang, *J. Colloid Interface Sci.*, 2020, **574**, 140–151.

232 T. Zhang, X. Sun, S. Weng, S. Zhang, C. Xu, X. Gao and N. Zhu, *J. Mol. Struct.*, 2025, **1321**, 140190.

233 S. Tavakoli and A. Abbasi, *Res. Chem. Intermed.*, 2025, **51**, 1457–1472.

234 F. Zheng, J. Lu, Q. Xu, M. Zhang, B. Zhao, J. Ji and Z. Zhou, *J. Energy Inst.*, 2025, **123**, 102339.

235 S. K. Konavarapu, G. Kim, K. Shin and S. Y. Kim, *Chem.–Eur. J.*, 2025, **31**, e202500010.

236 T.-m. Li, B.-q. Hu, J.-h. Han, W. Lu, F. Yu and B. Li, *Inorg. Chem.*, 2022, **61**, 7051–7059.

237 S. Ketrat, T. Maihom, S. Wannakao, M. Probst, S. Nokbin and J. Limtrakul, *Inorg. Chem.*, 2017, **56**, 14005–14012.

238 S. Li, Y. Hou, Q. Chen, X. Zhang, H. Cao and Y. Huang, *ACS Appl. Mater. Interfaces*, 2020, **12**, 2581–2590.

239 F. Akram, M. Tariq, A. Raza and N. Akhtar, *Polyhedron*, 2026, **283**, 117848.

240 Y. Zou, W.-D. Zhang, M. Chen, J. Liu, Z.-G. Gu and X. Yan, *J. Colloid Interface Sci.*, 2024, **653**, 11–19.

241 F. Zheng, M. A. Gaikwad, Z. Fang, S. Jang and J. H. Kim, *Energy Fuels*, 2024, **38**, 6290–6299.

242 Z. Xu, C.-L. Yeh, Y. Jiang, X. Yun, C.-T. Li, K.-C. Ho, J. T. Lin and R. Y.-Y. Lin, *ACS Appl. Mater. Interfaces*, 2021, **13**, 28242–28251.

243 M. Zhao, T. Guo, W. Qian, Z. Wang, X. Zhao, L. Wen and D. He, *Chem. Eng. J.*, 2021, **422**, 130055.

244 H. Chu, R. Li, P. Feng, D. Wang, C. Li, Y. Yu and M. Yang, *ACS Catal.*, 2024, **14**, 1553–1566.

245 M. Nozari-Asbemarz, M. Amiri, A. Khodayari, A. Bezaatpour, S. Nouhi, P. Hosseini, M. Wark, R. Boukherroub and S. Szunerits, *ACS Appl. Energy Mater.*, 2021, **4**, 2951–2959.

246 Y. Li, T. Zhao, M. Lu, Y. Wu, Y. Xie, H. Xu, J. Gao, J. Yao, G. Qian and Q. Zhang, *Small*, 2019, **15**, 1901940.

247 X. Wang, J. Zhang, D. Ma, X. Feng, L. Wang and B. Wang, *ACS Appl. Mater. Interfaces*, 2021, **13**, 33209–33217.

248 Y. Li, B. Huang, X. Zhao, Z. Luo, S. Liang, H. Qin and L. Chen, *J. Power Sources*, 2022, **527**, 231149.

249 C. Kang, L. Ma, Y. Chen, L. Fu, Q. Hu, C. Zhou and Q. Liu, *Chem. Eng. J.*, 2022, **427**, 131003.

250 M. Liu, H. Miao, T. Ye, J. Gao, L. Tan, Y. Tian, Z. Fu, L. Wen, M. Yan, W. Gu, G. Gu, Y. Wang and Y. Wang, *Adv. Funct. Mater.*, 2026, e12905.

251 H. Tariq, M. S. Khan, M. A. Khan, A. Ali, A. Shuja, M. Owais, S. Alam, Y. Khan and I. Murtaza, *ChemistrySelect*, 2025, **10**, e05134.

252 A. Veysi, M. Roushani and H. Najafi, *Heliyon*, 2025, **11**, e41296.

253 S. Wang, J. Lu, Q. Liu, H. Cui, H. Wang, X. Feng, K. Ge, Y. Yang and Y. Zhao, *J. Environ. Chem. Eng.*, 2025, **13**, 117176.

254 M. A. Karim, M. R. Abdul Karim, A. Ahmed and M. A. Marwat, *Electrochim. Acta*, 2025, **542**, 147509.

255 K.-R. Oh, H. Lee, G.-N. Yun, C. Yoo, J. W. Yoon, A. Awad, H.-W. Jeong and Y. K. Hwang, *ACS Appl. Mater. Interfaces*, 2023, **15**, 9296–9306.

256 S. Guo, L. H. Kong, P. Wang, S. Yao, T. B. Lu and Z. M. Zhang, *Angew. Chem.*, 2022, **134**, e202206193.

257 G. Li, L. Lu, L. Pei, Z. Ma, Y. Yuan, M.-L. Hu, Q. Miao and J. Zhong, *Inorg. Chem.*, 2022, **61**, 738–745.

258 Y. Wu, W. Wang, W. Jiang, H. Li, Y. Ma, C. Liu and X. Yang, *Int. J. Hydrogen Energy*, 2022, **47**, 31587–31595.

259 Y. Pan, J. Zhang, Z. Zhao, L. Shi, B. Wu and L. Zeng, *Int. J. Hydrogen Energy*, 2021, **46**, 34565–34573.

260 R. Yu, C. Wang, D. Liu, X. Wang, J. Yin and Y. Du, *Inorg. Chem.*, 2023, **62**, 609–617.

261 X. Hou, J. Zhou, X. Xu, X. Wang, S. Zhang, H. Wang and M. Huang, *Catal. Commun.*, 2022, **165**, 106445.

262 L. Ai, Y. Luo, W. Huang, Y. Tian and J. Jiang, *Int. J. Hydrogen Energy*, 2022, **47**, 12893–12902.

263 Y. Li, B. Thomas, C. Tang and T. Asefa, *Dalton Trans.*, 2023, **52**, 17834–17845.

264 L. Ma, Q. Xue, Y. Dang, L. Wang and Y. Zhou, *J. Colloid Interface Sci.*, 2024, **655**, 234–242.

265 J. Ma, S. Wang, W. He, H. Chen, X. Zhai, F. Meng and Y. Fu, *ChemSusChem*, 2021, **14**, 5042–5048.

266 W. H. Choi, K.-H. Kim, H. Lee, J. W. Choi, D. G. Park, G. H. Kim, K. M. Choi and J. K. Kang, *Advanced Science*, 2021, **8**, 2100044.

267 R. Qi, Z. Zhong, F. Chen, X. Zhen, Q. Li, Y. Yang and Q. Ye, *Fuel*, 2024, **357**, 129882.

268 J.-T. Yuan, J.-J. Hou, X.-L. Liu, Y.-R. Feng and X.-M. Zhang, *Dalton Trans.*, 2020, **49**, 750–756.

269 S. S. Sankar, K. Manjula, G. Keerthana, B. Ramesh Babu and S. Kundu, *Cryst. Growth Des.*, 2021, **21**, 1800–1809.

270 X. Deng, H. Qin, X. Liu, S. Zhu, J. Li, L. Ma and N. Zhao, *J. Alloys Compd.*, 2022, **918**, 165650.

271 D. Taherinia, H. Hatami and F. Mirzaee Valadi, *J. Electroanal. Chem.*, 2022, **922**, 116720.

272 R. Li, X. Chen, H. Zhang, Y. Wang, Y. Lv, H. Jiang, B. Guo and X. Feng, *Inorg. Chem.*, 2024, **63**, 2282–2288.

273 Y. Gong, L. Sun, J. Hu, F. Xie, H. Tan, Y. Qu, K. Wang and Y. Zhang, *Mater. Today Energy*, 2021, **21**, 100825.

274 W. Wu, X. Wang, Y. Yan and X. Li, *Mater. Lett.*, 2023, **334**, 133722.

275 X. Zhao, Q. Bi, C. Yang, K. Tao and L. Han, *Dalton Trans.*, 2021, **50**, 15260–15266.

276 D. K. Yadav, J. Muhommad and S. Deka, *ACS Appl. Nano Mater.*, 2023, **6**, 13513–13523.

277 W. Zhao, G. Yan, Y. Zheng, B. Liu, D. Jia, T. Liu, L. Cui, R. Zheng, D. Wei and J. Liu, *J. Colloid Interface Sci.*, 2020, **565**, 295–304.

278 S. Li, T. Yu, F. Li, T. Chen, L. Zhang, G. Wang, J. Xin and D. Zhang, *Energy Fuels*, 2022, **36**, 5492–5501.

279 Z. Andikaey, A. A. Ensafi, B. Rezaei and J.-S. Hu, *Electrochim. Acta*, 2022, **417**, 140338.

280 P. Panda, S. Roy, R. Samanta and S. Barman, *ACS Appl. Nano Mater.*, 2023, **6**, 15916–15924.

281 S. Y. Lee, H. J. An, J. Moon, D. H. Kim, K. W. Park and J. T. Park, *Electrochim. Acta*, 2023, **451**, 142291.

282 H. Zhang, X. Lu, L. Yang, Y. Hu, M. Yuan, C. Wang, Q. Liu, F. Yue, D. Zhou and Q. Xia, *Mol. Catal.*, 2021, **499**, 111300.

283 Q. Mo, H. Zheng and G. Sheng, *Mol. Catal.*, 2024, **553**, 113817.

284 A. Ibrahim, X. Liu, C. N. Uguna and C. Sun, *Mater. Today Sustain.*, 2023, **23**, 100424.

285 H. Zhang, F. Sun, X. Lu, H. Guo, Y. Dong, Q. Zhang, J. Chen, D. Zhou and Q. Xia, *Mol. Catal.*, 2023, **535**, 112903.

286 K.-R. Oh, H. Lee, H.-W. Jeong, G.-N. Yun, A. Awad, A. Nimbalkar, M. Lee and Y. K. Hwang, *J. CO₂ Util.*, 2023, **78**, 102633.

287 Y. Li and S. Li, *Int. J. Hydrogen Energy*, 2020, **45**, 10433–10441.

288 Y. Song, M. Xu, Z. Li, L. He, M. Hu, L. He, Z. Zhang and M. Du, *Sens. Actuators, B*, 2020, **311**, 127927.

289 C. Chen, Y. Zhong, S. Cheng, Y. Huanga, T. Li, T. Shi, G. Liao and Z. Tang, *J. Electrochem. Soc.*, 2020, **167**, 027531.

290 X. Zhang, D. Li, Y. Sun, C. Dong, H. Zhu, X. Li, Q. Cao, J. Shen, F. Yan and Y. Wei, *Mater. Lett.*, 2021, **293**, 129739.

291 Y. Zhang, Y. Huang, P. Gao, W. Yin, M. Yin, H. Pu, Q. Sun, X. Liang and H.-b. Fa, *Microchem. J.*, 2022, **175**, 107097.

292 S. Binyamin, R. Shimoni, I. Liberman, R. Ifraemov, A. Tashakory and I. Hod, *ACS Appl. Mater. Interfaces*, 2024, **16**, 13849–13857.

293 L. Jin, H. Liu, A. Xu, Y. Wu, J. Lu, J. Liu, S. Xie, Y. Yao, L. Dong, M. Zhang, S. Kai and M. Fan, *Microporous Mesoporous Mater.*, 2021, **317**, 110997.

294 K. Tong, G. Lu, F. Kong, Z. Wei, Z. Zhan and X. Wang, *ACS Appl. Nano Mater.*, 2025, **8**, 17440–17450.

295 H. Zhang, S. Zhang, Y. Zhang, X. Chen, H. Zhan and D. Cai, *Catal. Lett.*, 2025, **155**, 1–13.

296 M. Ma, E. Chen, H. Yue, G. Tian and S. Feng, *Nat. Commun.*, 2025, **16**, 367.

297 A. Dhakshinamoorthy, S. Navalón, A. Primo and H. García, *Angew. Chem.*, 2024, **136**, e202311241.

298 J. Zhang, B. An, Z. Li, Y. Cao, Y. Dai, W. Wang, L. Zeng, W. Lin and C. Wang, *J. Am. Chem. Soc.*, 2021, **143**, 8829–8837.

299 B. Gikonyo, E. Montero-Lanzuela, H. G. Baldovi, S. De, C. Journet, T. Devic, N. Guillou, D. Tiana, S. Navalon and A. Fateeva, *J. Mater. Chem. A*, 2022, **10**, 24938–24950.

300 Z. Yongjia, M. A. Islam and B. B. Saha, *Colloids Surf., A*, 2025, **713**, 136524.

301 K. Lin, J. Qin, Z. Liu, W. Xu, M. Li, Y. Zheng, W. Han, G. Zhou, J. Fang, Z. Fang, F. Peng and K. L. Yeung, *Environ. Res.*, 2025, **279**, 121789.

302 C. Shi, N. Tang, S. Pu, H. Xin, L. Wu and X. Hou, *Chem. Eng. J.*, 2025, **503**, 158621.

303 A. Santiago Portillo, H. G. Baldoví, M. T. García Fernandez, S. Navalón, P. Atienzar, B. Ferrer, M. Alvaro, H. Garcia and Z. Li, *J. Phys. Chem. C*, 2017, **121**, 7015–7024.

304 A. Bhattacharyya, M. Gutiérrez, B. Cohen, A. Valverde-González, M. Iglesias and A. Douhal, *Mater. Today Energy*, 2022, **29**, 101125.

305 Y. B. N. Tran, P. T. K. Nguyen, V.-A. Dao and V.-D. Le, *New J. Chem.*, 2024, **48**, 5300–5310.

306 A. A. Meshram and S. M. Sontakke, *Mater. Today: Proc.*, 2023, **72**, 47–54.

307 S. Bahrani, S. A. Hashemi, S. M. Mousavi and R. Azhdari, *Drug Metab. Rev.*, 2019, **51**, 356–377.

308 A. G. Eldin, E. H. Mohamed, S. M. El-Sheikh, S. M. Sheta, A. O. Youssef, E. Elshahat, M. S. Attia and M. N. Abou-Omar, *RSC Adv.*, 2025, **15**, 34149–34159.

309 M. Nakhaei, K. Akhbari, M. Kalati and A. Phuruangrat, *Inorg. Chim. Acta*, 2021, **522**, 120353.

310 R. Safdar Ali, H. Meng and Z. Li, *Molecules*, 2021, **27**, 100.

311 W. Li, D. Li, Y. Yang, S. Su, S. Qie, Y. Jia and M. Hu, *J. Mol. Struct.*, 2025, **1321**, 139974.

312 W. Wei, H. Wang, P. Su, J. Song and Y. Yang, *Talanta*, 2025, **291**, 127862.

313 Y. Wan, J. Fang, Y. Wang, J. Sun, Y. Sun, X. Sun, M. Qi, W. Li, C. Li and Y. Zhou, *Adv. Healthcare Mater.*, 2021, **10**, 2101515.

314 A. Radwan, A. A. A. Aziz, A. M. Abdel-Aziz, M. E. Sidqi and M. A. Sayed, *Inorg. Chem. Commun.*, 2025, **179**, 114870.

315 J. Komara, J. P. Karumuri and M. Gudivada, *Res. Chem. Intermed.*, 2025, 1–19.

316 R. Abazari, A. R. Amani-Ghadim, A. M. Z. Slawin, C. L. Carpenter-Warren and A. M. Kirillov, *Inorg. Chem.*, 2022, **61**, 9514–9522.

317 R. Bhosale, S. Bhosale, D. Narale, C. Jambhale and S. Kolekar, *Langmuir*, 2023, **39**, 12075–12089.

318 U. A. Kolachi, N. H. Solangi, Y. Sun, R. Andavar, I. Shahid, J. Zhao and J. Pan, *J. Mater. Chem. A*, 2025, **13**, 22142–22154.

319 T. Stolar, A. Prašnikar, V. Martinez, B. Karadeniz, A. Bjelić, G. Mali, T. Friščić, B. Likozar and K. Užarević, *ACS Appl. Mater. Interfaces*, 2021, **13**, 3070–3077.

320 A. Karbalaee Hosseini, F. Moghadaskhou, A. Tadjarodi and B. Safarkoopayeh, *Inorg. Chem.*, 2023, **62**, 21156–21163.

321 J. Liu, Y. Zhao, L.-L. Dang, G. Yang, L.-F. Ma, D.-S. Li and Y. Wang, *Chem. Commun.*, 2020, **56**, 8758–8761.

322 S. Varangane, C. S. Vennapoosa, A. Tiwari, S. K. Nataraj, T. P. Yendrapati and U. Pal, *Appl. Organomet. Chem.*, 2022, **36**, e6815.

323 N. Nagarjun and A. Dhakshinamoorthy, *New J. Chem.*, 2019, **43**, 18702–18712.

324 N. Nagarjun, K. Arthy and A. Dhakshinamoorthy, *Eur. J. Inorg. Chem.*, 2021, **2021**, 2108–2119.

325 H. Lv, L. Fan, H. Chen, X. Zhang and Y. Gao, *Dalton Trans.*, 2022, **51**, 3546–3556.

326 B. Yi, H. Zhao, L. Cao, X. Si, Y. Jiang, P. Cheng, Y. Zuo, Y. Zhang, L. Su, Y. Wang, C. K. Tsung, L. Y. Chou and J. Xie, *Mater. Today Nano*, 2022, **17**, 100158.

327 W.-J. Ji, G.-F. Liu, B.-Q. Wang, W.-B. Lu and Q.-G. Zhai, *CrystEngComm*, 2020, **22**, 4710–4715.

328 Y. Li, F. Wang, M. Liang, M. Sun, L. Xia and F. Qu, *Talanta*, 2024, **278**, 126456.

329 Z. Zhang, L. Liu, T. Zhang and H. Tang, *ACS Appl. Mater. Interfaces*, 2023, **15**, 18982–18991.

330 S. Li, R. Wang, M. Xie, Y. Xu, J. Chen and Y. Jiao, *J. Colloid Interface Sci.*, 2022, **622**, 378–389.

331 X. Zhao, Y. Wang, Z. Zhai, C. Zhuang, D. Tian, H. Guo, X. Zou and T. X. Liu, *ACS Appl. Nano Mater.*, 2023, **6**, 8315–8324.

332 S.-N. Zhao, G. Wang, D. Poelman and P. V. D. Voort, *Materials*, 2018, **11**, 572.

333 L.-L. Ma, G.-P. Yang, G.-P. Li, P.-F. Zhang, J. Jin, Y. Wang, J.-M. Wang and Y.-Y. Wang, *Inorg. Chem. Front.*, 2021, **8**, 329–338.

334 Y. Liu, X. Zhou, W. Zhu, C. Chen, C. Fan, L. Ding and K. Wang, *Inorg. Chem.*, 2023, **62**, 15022–15030.

335 C. Simms, A. Mullaliu, F. de de Azambuja, G. Aquilanti and T. N. Parac-Vogt, *Small*, 2024, **20**, 2307236.

336 Q. Zhang, Z. Sang, Q. Li, J. Gong, X. Peng, L. Li, Z. Zhang, B. Zhang, S. Li and X. Yang, *J. Mol. Liq.*, 2022, **356**, 119024.

337 L. Zhao, K. Sun, N. Youliwasi, H. Guo, G. Yang, F. Jiao, B. Dong, Y. Chai, S. Mintova and C. Liu, *Appl. Surf. Sci.*, 2019, **470**, 91–98.

338 R. Zhao, Z. Wang, W. Li, Z. Zhang, H. Xu and H. Zhao, *J. Mater. Sci.*, 2025, **60**, 861–880.

339 Y. Lu, Z. Bai, Z. Sun, F. Wang, S. Pei, S. Wang, C. Wang, X. Li and B. Wang, *Chem. Eng. J.*, 2025, **520**, 166079.

340 H. Lv, H. Chen, T. Hu and X. Zhang, *Inorg. Chem. Front.*, 2022, **9**, 5788–5798.

341 Z. Li, G. Liu, C. Fan and S. Pu, *Anal. Bioanal. Chem.*, 2021, **413**, 3281–3290.

342 Z. Zhao, S. Yang, M. Zhu, Y. Zhang, Y. Sun and S. Wu, *Sens. Actuators, B*, 2023, **383**, 133593.

343 M. Wu, Z. W. Jiang, P. Zhang, X. Gong and Y. Wang, *Sens. Actuators, B*, 2023, **383**, 133596.

344 Z. Lu, Y. Jiang, P. Wang, W. Xiong, B. Qi, Y. Zhang, D. Xiang and K. Zhai, *Anal. Bioanal. Chem.*, 2020, **412**, 5273–5281.

345 X. Yue, L. Fu, Y. Li, S. Xu, X. Lin and Y. Bai, *Food Chem.*, 2023, **410**, 135390.

346 C. Zhang, Y. Wu, X. Hong, W. Lei, M. Xia and F. Wang, *Spectrochim. Acta, Part A*, 2024, **304**, 123326.

347 J. Yao, M. Xie and Y. Li, *Microporous Mesoporous Mater.*, 2021, **317**, 110831.

348 H. Yu, Q. Liu, J. Li, Z.-M. Su, X. Li, X. Wang, J. Sun, C. Zhou and X. Hu, *J. Mater. Chem. C*, 2021, **9**, 562–568.

349 J. Yin, H. Chu, S. Qin, H. Qi and M. Hu, *Sensors*, 2021, **21**, 7355.

350 J.-L. Li, Y. Xiao, L.-Y. Wang, Y.-H. Xing, F.-Y. Bai and Z. Shi, *Polyhedron*, 2022, **214**, 115648.

351 Y. Wu, Y. Zhou, H. Long, X. Chen, Y. Jiang, L. Zhang and T. Le, *Food Chem.*, 2023, **422**, 136250.

352 X. Zeng, J. Hu, M. Zhang, F. Wang, L. Wu and X. Hou, *Anal. Chem.*, 2020, **92**, 2097–2102.

353 M. Wu, Y. Zhuang, J. Liu, W. Chen, X. Li and R.-J. Xie, *Opt. Mater.*, 2020, **106**, 110006.

354 Y. Songlin, S. Dongxue, L. Kaisu, W. Lei, Z. Ying, S. Yaguang, Z. Mingchang and W. Shuangyan, *Dyes Pigm.*, 2023, **220**, 111673.

355 X. Zhai, P. Feng, N. Song, G. Zhao, Q. Liu, L. Liu, M. Tang and Y. Tang, *Inorg. Chem. Front.*, 2022, **9**, 1406–1415.

356 F. Zhang, Z. Zhao, F. Wang, Y. Pu and H. Cheng, *J. Solid State Chem.*, 2019, **280**, 120972.

357 W. Shi, T. Li, N. Chu, X. Liu, M. He, B. Bui, M. Chen and W. Chen, *Mater. Sci. Eng., C*, 2021, **129**, 112404.

358 Y. Gao, Y. Zhu, Y. Wang and J. Bi, *Spectrochim. Acta, Part A*, 2024, **323**, 124915.

359 X. Jiang, J. Hu, Y. Zhang, X. Zeng and Z. Long, *Microchem. J.*, 2020, **159**, 105417.